APPLICATION OF MACHINE LEARNING ALGORITHMS ON VIV FATIGUE LIFE ASSESSMENT OF MULTI-SPANNING SUBSEA PIPELINES

by

© Mobin Abdolalipour Miandoab

A Thesis submitted to the

School of Graduate Studies

in partial fulfillment of the requirements for the degree of

Master of Engineering

Faculty of Engineering and Applied Science

Memorial University of Newfoundland

Oct 2023

St. John's   Newfoundland   Canada

ABSTRACT

Subsea pipelines are the most efficient and reliable method of transportation of liquid, gas, and multiphase products through an aquatic medium. Pipelines laid on the uneven seabed lose contact with the seabed, leaving it suspended in some areas. The length of the pipeline hung over the seabed is called freespan. The free-spanning length of the pipeline is subjected to different static and hydrodynamic loads where the Vortex-Induced Vibrations (VIV) are among the most severe factors threatening pipeline integrity.

Repetitive deflection on the free-spanning length of the pipeline imposes fatigue damage on the pipeline structure. Consequently, it results in the early failure of the structure before the expected operational life. Regarding the critical role of subsea pipelines and the uncertainty of pipeline behavior against VIV damages, high safety factors are usually applied in designing subsea free-spanning pipelines, bringing unnecessary financial burdens on offshore pipeline projects.

Designing subsea pipeline projects is primarily conducted based on standard codes (e.g., DNVGL RP-F105, DNVGL RP-C203, and DNVGL RP-F114). However, accurate assessment of the free-spanning pipeline integrity against the VIV needs advanced experimental and numerical modeling with extensive cost and time impacts.

In this study, machine-learning algorithms are adopted to develop a cost-effective and easy-to-implement solution for VIV-induced fatigue analysis of free-spanning and multi-spanning pipelines. The numerical model was developed based on recommendations provided by DNVGL RP-F105 and verified by numerical results from FATFREE software, which is developed by DNV for analysis of subsea free-spanning pipelines (DET NORSKE

VERITAS, 2021). The comparison conducted using the data presented by Pereira et al. (Pereira et al., 2008). The employment of machine learning methods requires a high-quality dataset covering all of the possible cases. In this regard, a Python script was developed to control ABAQUS for creating different case studies and interacting with output results to perform data cleaning and preparation. The procedure of creating case studies, reading and analyzing outcomes, and cleaning and preparing results for machine learning was performed by a fully automated cycle managed by Python scripts. More than 200000 configurations of single free-span and multi-spanning conditions were analyzed. In order to have a more realistic study, pipeline characteristics, and soil properties were selected from available industrial products and trusted industrial data such as standard codes of DNVGL. The study showed that machine learning algorithms can effectively predict the fatigue life of the free-spanning pipelines subjected to VIV oscillations. Particularly, this can be of significant importance during the initial design projects for a fast and fairly accurate assessment of the fatigue lives.

ACKNOWLEDGMENT

Contents

List of Figures

List of Tables

List of Abbreviations and Symbols

Abbreviations

AI   Artificial Intelligence

DTR   Decision Tree Regression

ETR   Extra Tree Regression

KC   Keoulegan Carpenter

ML   Machine Learning

MAE   Mean Absolute Error

RBF   Radial Basis Functions

RFR   Random Forest Regression

RMSE   Real Mean Square Error

SVR   Support Vector Regression

VC   Vapnik-Chervonenkis

VIV   Vortex Induced Vibration

Symbols

D_{acc}	Accumulated fatigue damage
C_a	Added mass coefficient
R_k	Amplitude reduction factor due to amplitude
ω	Angular velocity
ψ_β	Correction factor for fluid flow ratio β
A_e	Cross sectional area of element
A_{CF}	Cross-flow stress amplitude
A_z	Cross-flow VIV amplitude
ζ	Damping ratio
ρ	Density of fluid
ρ_s	Density of steel
e	Depth of gap
C_D	Drag coefficient
F_D	Drag force
μ	Dynamic viscosity
m_e	Effective mass

U	Flow speed
β	Fluid flow ratio
C_M	Inertia coefficient
F_I	Inertia force
A_{IL}	In-line stress amplitude
A_Y	In-line VIV amplitude
KC	Keulegan-Carpenter's Number
$K_{L,D}$	Lateral spring stiffness
l_e	Length of element
$L_{span\ length}$	Length of free-spanning area
L_{max}	Length of greater span in configuration of two neighboring spans.
$L_{shoulder}$	Length of shoulder in a multi-spanning configuration
L_{min}	Length of smaller span in configuration of two neighboring spans.
m	Mass
m^*	Mass per unit of length of pipeline
$\vec{W}$	Matrix of mode shape
I	Moment of inertia

L_R	Multi-span relative aspect ratio
f_n	Natural frequency
T	Period of oscillation
ν	Poisson's ratio
v_r	Reduced Velocity
L_{sh}	Relative length of shoulder in a multi-spanning configuration.
Re	Reynolds number
γ_s	Safety factor for stress
C_v	Simplified dynamic stiffness (vertical)
C_L	Simplified stiffness factor (lateral)
C_v	Simplified stiffness factor (vertical)
U_∞	Speed of fully developed current flow
K_s	Stability parameter
k	Stiffness
S_t	Strouhal number
ζ_T	Total Damping ratio
U_C	Velocity of current

U_w Velocity of wave

$K_{V,D}$ Vertical spring stiffness

t Wall thickness

E Young's modulus

Chapter 1:

Introduction

1.1   Overview

Pipelines are the most reliable and safest method for transportation of oil and gas products. Subsequently, offshore pipelines play a vital role in cost-effective, reliable, and safe transportation of hydrocarbon products (Chen et al., 2021; Green & Jackson, 2015; Kabul & Madiistriyatno, 2021; Marhavilas et al., 2021). Regarding the important role of offshore pipelines, traditional measurement to protect offshore pipelines was to lay pipe strings inside a trenched canal and bury them. Buried pipelines benefit extra security against collision-based incidents in shallow waters and occurrence of free-spanning created by local erosion of soil sediments under the pipeline washed off by current flow. However, due to the high cost of trenching, pipeline projects are designed to be directly laid down on the seabed (Zhang et al., 2020a).

Subsea pipelines laying on uneven seabed are exposed to free-spanning condition, which can severely damage the pipeline, leading to a dramatic cut in pipeline life expectancy. Ambient current-flow crossing pipeline cross-section leads to the creation of wake areas or vortices behind the pipeline, which can result in a continues shake of the pipeline called Vortex-Induced Vibration (VIV). The VIV can impose dynamic loads on subsea pipelines, which might dramatically decline the estimated fatigue life of pipelines. Understanding pipeline behavior against VIV can not only play vital role in preventing VIV failure but will also be a milestone in designing a reliable and cost-effective subsea pipeline project.

This thesis's main subject is to study VIV's impact on the fatigue life of multi-spanning subsea pipelines.

In general, Engineering problems can either be studied through experiments or computational/numerical studies. Experimental models themselves can be performed with real models with exact features of the studied subject or simplified models which are normally smaller in size and therefore easier to work with. Numerical modeling is also a very useful technique for studying engineering problems where, instead of physical experiments, the problem is simulated with Computer Aid Engineering (CAE) tools and the engineering incident/behavior/operation is simulated within the software. Regarding the complexity of the VIV fatigue of subsea freespanning pipeline and presence of multiple independent factors influencing structures performance, there is a need for great number of case studies to find out impact of every single parameter on pipeline's performance against VIV fatigue.

Having many variables involved in the model and the need to implement large number of case studies, makes it difficult to employ traditional methods to find out impact of variables on structure's performance against VIV loads. Machine Learning (ML) methods which are designed to work with large number of inputs and to handle diverse sets of data, can be a useful method for resolution of VIV fatigue problems on subsea pipelines.

Traditionally, there are two main approaches for studying a problem in engineering, one is to perform experimental tests on practical case studies, and the other is to numerically simulate the situation using finite element/ finite volume software. Regarding the harsh environmental condition of installed subsea pipelines and technical difficulties of modeling

the seabed-pipeline interaction, experimental studies cannot be considered a conventional research approach. Due to the complex nature of pipeline-seabed interaction under VIV loads, numerical modeling will need a great amount of computational resources, making the analysis expensive. Both of the conventional study methods are based on case studies and a generalized outcome cannot be expected from them. In this thesis, Machine Learning methods (ML) have been employed to predict pipeline behavior under VIV loads to overcome the aforementioned problems.

Input data for training the machine learning model have been generated using ABAQUS software in combination with python scripting for case studies. In order to manage huge amounts of data and computational resources, a python script has been developed. The managing python code enabled us to perform data-cleaning and pre-processing steps simultaneous to FE model analysis by ABAQUS, giving us a significant advantage in time-efficiency in generating input database for ML. The ABAQUS model is verified based on a comparison between the model and data from DNV FATFREE and Intec Span 2B data (Pereira et al., 2008).

Four different ML methods have been used including Decision Tree Regression (DTR), Random Forest Regression (RFR), Extra Tree Regression (ETR), and Support Vector Regression (SVR). Studies show that DTR and RFR methods have excellent performance in training a precise model followed by ETR, which also had a good performance. Unlike other methods, models trained by d SVR with default settings failed to predict VIV behavior of the pipeline with desired precision.

Results from this research indicate that the total free-spanning length of pipeline is the most important parameter governing VIV damage. The longer free-spanning length leads to greater VIV damage on the pipeline. In addition, pipe parameters such wall-thickness and pipe diameter are other important parameters affecting the fatigue performance of the pipeline. On the other hand, width of the dividing shoulder between two neighboring free-spans in multi-spanning condition, has less significant effect on pipeline performance. The depth of the span also plays a neutral role except when the depth is as low as the pipeline collides with the seabed within free-spanning length while impacted by VIV vibrations, leading to immediate failure.

1.2   Original contribution

In the presented project, it has been practiced having an extensive study to determine key factors affecting pipeline's performance against VIV fatigue loads. Unlike common practice in case studies where it is mostly to study influence of one parameter on final result, in this study all possible parameters of pipeline-seabed on a multispanning configuration have been considered including length of each freespan, length of shoulder, mechanical properties of pipe, depth of freespanning gap, and length of total spanning area. Regarding the number of involved variables and extended of different values assumed for variables, the is a massive number of different cases for studying.

For post-processing output dataset, machine learning methods have been employed for fast and accurate evaluation of dataset. In order to input dataset to be fed to machine learning models, the numbers and variables are best to be dimensionless while regarding mechanical

nature of variables in this study, they are mostly defined as units. To make variables suitable for machine learning purposes, they have been combined in accordance to build new dimensionless parameters for machine learning purposes.

In this thesis, a database of free-spanning pipeline's behavior under Vortex-Induced Vibrations has been developed and by applying machine learning methods, impact of different structural parameters on pipeline's VIV fatigue performance has been investigated. The numerical model has been developed using ABAQUS software. Modeling and post processing of study cases have been performed using practices recommend in DNVGL RP-F105 and DNV RP-F114 (Det Norske Veritas Germanischer Lloyd (DNV GL), 2021; Det Norske Veritas Germanischer Lloyd (DNV GL), 2017).

No-dimensional parameters have always been key tools in analysis of fluid-solid interaction. A comprehensive list of non-dimensional parameters has been employed to interpret the influence of a full list of characteristics of pipeline structure and free-span configuration on VIV fatigue performance of free-spanning/multi-spanning pipelines. Since the stress calculations are conducted using semi-empirical approach of DNV RP F105, nonlinearity and scattered influence of parameters on final VIV stress is naturally expected. This complexity associated with a great number of cases makes the final analysis rigorous to solve; therefore, machine learning as a modern tool suitable for analysis of immense datasets have been effectuated. The proposed methodology, the developed numerical models and ML algorithms along with post processing tools and Python scripts are all amongst the original contributions of the current study. In addition, the study resulted in one conference and one journal papers as follows:

Abdolalipour, M., Shiri., H (2022), "Pipeline-Soil Interaction Effects on Vortex-induced Vibration Fatigue Analysis of Multi-Spanning Subsea Pipelines Using Decision Tree Regression", *75th Canadian Geotechnical Conference, GeoCalgary2022*, Calgary, Alberta, Oct 2 – 5.

Abdolalipour, M., Azimi, H., Shiri, H. (2022), "VIV fatigue life assessment of free-spanning subsea pipelines using machine learning algorithms", *Journal of Pipeline Sciences and Engineering*, (under review).

1.2.1 Organization of the Thesis

This thesis starts with introduction as chapter 1 that defines the significance of the tackled problem, the novelty of developed methodology, the validation process, and the main findings of the project along with original contributions and thesis organization. Chapter 2 presents a thorough literature review about the recent advancements on Vortex-Induced Vibrations (VIV) of free-spanning subsea pipelines. The literature review covers studies published on free-span, numerical modeling of free-spans, theoretical approach for understanding VIV vibrations, and experimental studies conducted for VIV analysis. Chapter 3 outlines the theory of VIV on subsea free-spanning pipelines where semi-empirical solutions based on DNV standard codes are provided. In chapter 4, the developed finite element model and the free-span analysis using ABAQUS are presented in detail. The theory of adopted machine learning algorithms accompanied by output results are presented in chapter 5. In chapter 6, the conclusions extracted from observations are summarized accompanied by recommendations for future studies. Further analysis results are provided in appendix A.

Chapter 2:

Literature review

2.1 Free-span

Free-span is a condition where the contact between pipeline and seabed is lost. Currents crossing the pipeline's cross-section create wake areas downstream to the pipe section. Free-spanning is one of the major problems which needs to be considered in pipeline projects' design, installation, and operation. Free-spans don't occur as a result of unique reason; they can be developed as a result of a variety of reasons (Anfinsen, 1995; DET NORSKE VERITAS, 2021) The main reasons for free-spans to occur can be categorized into five groups as 1) Natural irregularities such as presence of icebergs which leave craters and hoe on the seabed during displacements; 2) local erosions and scouring which also might lead to the creation of free-spans; 3) Seabed uneven topography; 4) Seabed unevenness due to presence of industrial structures left from previous projects; 5) Unforeseen natural incidents such as earthquakes (Liang et al., 2005; Ronold, 1995; J. Yang et al., 2018; Zang et al., 2021). Classification of fatigue in pipelines is presented in taxonomy of Figure 2-1 (Keprate & Ratnayake, 2016).

Pipelines Fatigue

Mechanical & Metallurgical Failure

Environmental Assisted Cracking

Thermal Fatigue

Vibration Induced Fatigue

Corrosion Fatigue

Steady State Excitation

Transient Excitation

Flow Induced Turbulence

Mechanical Excitation

Flow Induced Pulsation

Acoustic Induced Vibration

Surge Changes due to Valve Operation

Cavitation & Flashing
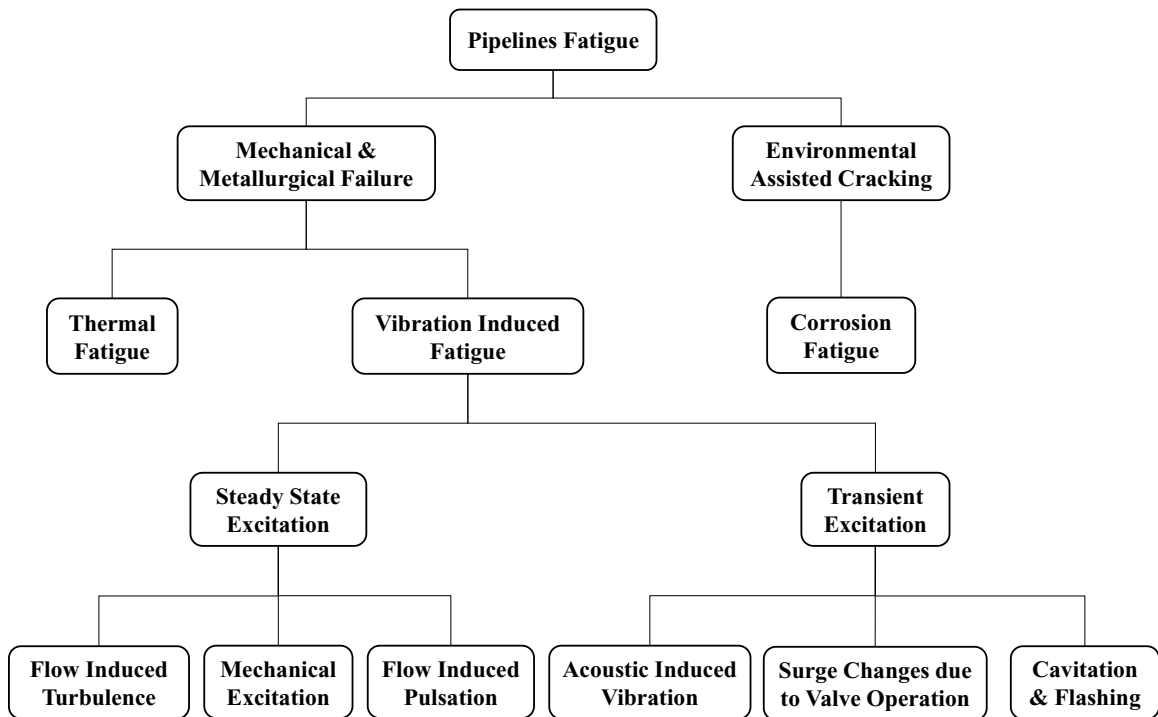
Figure 2-1: Taxonomy of piping fatigue (Keprate & Ratnayake, 2016).

Free-spanning lengths of pipeline are exposed to different static and dynamic loads in comparison to the rest of the pipeline. These loads are different in type and much higher in value than normal loads on the pipeline. Free-spanning specific loads includes high bending load due to suspended weight of pipeline, higher concentrated loads on shoulders between spans when there are two or more consecutive free-spans and other static and dynamic loads due to possible wave and currents. In cases where there is an inadmissible length of free-span, there is a good chance for Vortex-Induced Vibrations (VIV) to appear. It's believed that VIV is the main reason for fatigue failure of subsea pipelines (Bearman, 1978; Ronold, 1995). A semi-empirical solution presented by DNV is a globally accepted

approach for the analysis of VIV on free-spanning pipelines. The solution was first introduced as a recommended practice entitled DNV RP-F105 and then reviewed and updated to the current version of DNVGL-RP-F 105, amended in 2021. Technical solutions provided by DNV are in use on 65% of pipeline projects worldwide (Nair, 2020).

An early solution to prevent free-spanning in the 20th century was to physically intervene in seabed topology by placing external objects of other techniques to prevent extensive free-spanning length. Physical intervention is limited to pipeline projects installed at shallow waters and can only be performed in the absence of an adverse environmental condition. Nowadays, due to the high cost of physical intervention and considerable risks in harsh environments, this method is not controversial (Saheed Adekunle Shittu, 2022). So far, significant research has been conducted to determine pipeline behavior against VIV (Bryndum & Smed, 1998; Furnes & Berntsen, 2003; Pantazopoulos et al., 1993). It is desired and recommended that free-spanning length along pipeline remain within the allowable range determined in the design stage. In reality, external factors affect pipeline installation and operation procedures, including seabed topography, installation vessel limitations and maneuverability, and other external factors that cannot be applied in the design stage (H. S. Choi, 2001; DNV RP F105, 2006; Ronold, 1995).

2.1   Numerical Modeling

The accepted semi-empirical approach for VIV behavior of free-spanning pipelines relies on natural frequencies and natural mode shapes of pipeline structure (DET NORSKE VERITAS, 2021). There are different methods to find natural mode shapes and natural frequencies of pipeline in free-spanning condition such as experimental modal analysis or

numerical modeling. Modal analysis of a real pipeline in free-spanning conditions will be extraordinarily expensive and difficult to conduct; therefore, numerical modeling and semi-empirical solutions are preferred. There are two different techniques to numerically determine modal characteristics of the structure one is to simulate structure using computational fluid dynamic methods (CFD) and the other is to employ finite element analysis (FEA). CFD provides a more accurate solution in terms of flow dynamics by covering more details and non-linarites. Despite the advantages CFD has, regarding the need for enormous computational resources, CFD is not considered as a practical technique to employ. Analytical solutions offered for engineering problems rely on differential equations which are normally hard to solve, FEA is a method that divides the mechanical system into smaller parts known as elements. Elements are defined to behave as continuous bodies. Those elements have simpler boundary conditions; therefore, comparing the original complex equation they have much simpler equations which are easier to solve. By correct subdivision of problem, elements will represent an accurate approximation of original problem (Rao, S., & Yap, 2011).

In comparison to CFD, FEA methods consume reasonably less computation resources; therefore, using FEA methods to extract structural characteristics is a common approach. Application of FEA analysis is limited to case studies with simplified assumptions regarding pipeline behavior. In case of a thorough study with numerous configurations for seabed and pipeline, FEA analysis will not be cost-effective (Ole-Erik Vestøl Endrerud, 2013).

2.2 Structural and hydrodynamic parameters

Pipeline's performance against VIV loads depends on different factors such as pipe wall thickness to pipe diameter $\left(\frac{t}{D}\right)$, ratio of gap depth under the pipe to the pipe diameter $\left(\frac{\varepsilon}{D}\right)$, and relative span length based on pipe diameter $\left(\frac{L}{D}\right)$ (Endrerud OEV, 2013). In smaller gap ratio, Vortices in upper and lower side of pipe are not balanced. Unbalanced vortexes tend to suppress which means that the probability of VIV is low, and vibrations are likely to be suppressed. Previous studies indicated that target value for gap ratio for a safe and VIV free structure is 0.3. If the gap ratio is around 0.3 or smaller, unbalanced wake size in opposite sides will not form a VIV vibration (Sumer & Fredsøe, 2006)

In addition, wall proximity provides similar suppressive functionality. Efficiency of wall proximity on suppression of VIV vibrations can be estimated by using non-dimensional parameter of Keoulegan-Carpenter (KC). When the KC has a large value and sea current remains constant, conditions for a suppressive boundary are similar to gap ratio. When value of KC is smaller, boundaries are less effective in controlling VIV oscillations. Overall, boundaries are important when parameter KC has a large number (<40-50) (Sumer & Fredsøe, 2006).

Wall effect can also increase added mass and consecutively drag force implied on pipeline. When the gap ratio is small, the fluid film trapped between seabed and pipeline, plays as an invisible wall extending effective geometry of pipeline to the seabed. This phenomenon is a result of friction between the pipe's outer surface and the surrounding fluid around it.

The viscosity between pipe and fluid traps the fluid between the pipe and seabed which prevents the fluid from escaping (Ole-Erik Vestøl Endrerud, 2013).

Axial force and internal pressure of pipe are two other parameters that can have impacts of VIV performance of pipelines. Based on recommendations of DNV, natural frequencies and natural mode shapes are governing factors in VIV fatigue performance. Pipeline-seabed structures with smaller values for natural frequencies have higher risks of VIV vibrations. Studies indicate that an increase in internal pressure will lead into a decrease in natural frequency followed by higher risk of VIV damage on pipeline (Fyrileiv et al., 2005).

Regarding the relation between axial force and natural frequencies in free-spanning zones, studies show that bigger sagging force will decrease values of symmetric frequencies in crossflow direction modes. While this relation is in effect, axial force has no influence on non-symmetric crossflow modes nor inline modes (Søreide et al., 2001).

Span correction boulders are another external parameter that can affect VIV condition in free-spans. Correction boulders are corrective shoulders which are placed between pipe and seabed. Main goal of correction boulder is to alter the pipeline natural frequency from natural frequencies with higher risks of vortex shedding to frequencies which are safe regarding occurrence of VIV. Location of boulders plays a key role in their effectiveness. If the boulder is installed in a null point regarding natural mode shape, the boulder is neutral, and it is ignored in engineering calculations. In practical engineering calculations, a boulder which divides a free-span into two neighboring spans is ignored and total free-spanning zone is considered as a single long span with a length equal to total free-spanning length and interaction between neighboring spans is not admissible(Søreide et al., 2001).

Regarding diving shoulder between two neighboring spans, there are two different approaches. DNV advises to perform pre-screening to check whether two spans are interacting or not and then perform calculations based on screening result. On the other hand, Statoil has a simple rule. Based on Statoil recommendation, if shoulder length is more than six meters, two neighboring spans are considered two solo single spans and it is assumed that there are no interactions between them. When two neighboring single spans are treated as a simple single span and multi-spanning formulas doesn't apply (DET NORSKE VERITAS, 2021; Ole-Erik Vestøl Endrerud, 2013).Vortex induced vibrations (VIV) is one of the most important factors for fatigue failure of variety offshore structures including freespanning subsea pipelines, steel catenary risers, marine cables, and tension-leg platforms (Hirdaris et al., 2014).

Fatigue failure due to VIV can cause the structure to fail in tensions below the yield strength of structure(X. Song & Wang, 2019). Failure due to VIV fatigue is the main cause of a significant number of offshore incidents. There are major incidents directly related to VIV fatigue such as failure of mooring line of LNG vessel in the North Sea in 2017 and failure of production platform in gulf of Mexico in (DNV, 2012; safety4sea, 2019; Saheed Adekunle Shittu, 2022).

Along the suspended length of the pipe, due to presence of stream-wise drag force, dynamics loads on pipeline are cyclic and the mean of cyclic stresses imposed to pipeline is not zero. In some topographic conditions where there is residual bending stress on laid pipeline. These bending stresses are also another reason for the non-zero value of mean stress on pipelines. The residual bending forces are mostly active along vertical direction.

(Mohaddes Pour et al., 2021). In addition to stresses in inline and crossflow directions, peak stress which is influenced by stresses in both directions is one the main factors controlling fatigue damages on the free-spanned pipeline(DET NORSKE VERITAS, 2021; DNV RP F105, 2006). Span characteristics of span length and size of gap are believed to be two main parameters which degree of fatigue is dependent to them (Saheed Adekunle Shittu, 2022). Depending on shape of the gap and pipeline properties, pipeline can be bent downward the gap depth by the gravity force implied by pipeline's self-weight (Kenny, 1993). Different types of free-spanning configurations are also categorized by Agilah Binti Abu Bakar and Ridzuan. Different configuration of free-span is presented in Figure 2-2 (Aqilah Binti Abu Bakar & Darul Ridzuan, 2014).

1) PIPELINE CROSSES SEABED DEPRESSION

2) PIPELINE CROSSES SEABED WITH CHANGE IN SLOPE

3) PIPELINE CROSSES SEABED DEPRESSION WITH SLOPING ENDS

4) PIPELINE CROSSES SEABED ROCK OUTCROP

5) PIPELINE TOUCHES DOWN AT CENTER OF SEABED DEPRESSION

6) PIPELINE CROSSES HIGHLY UNEVEN REGION
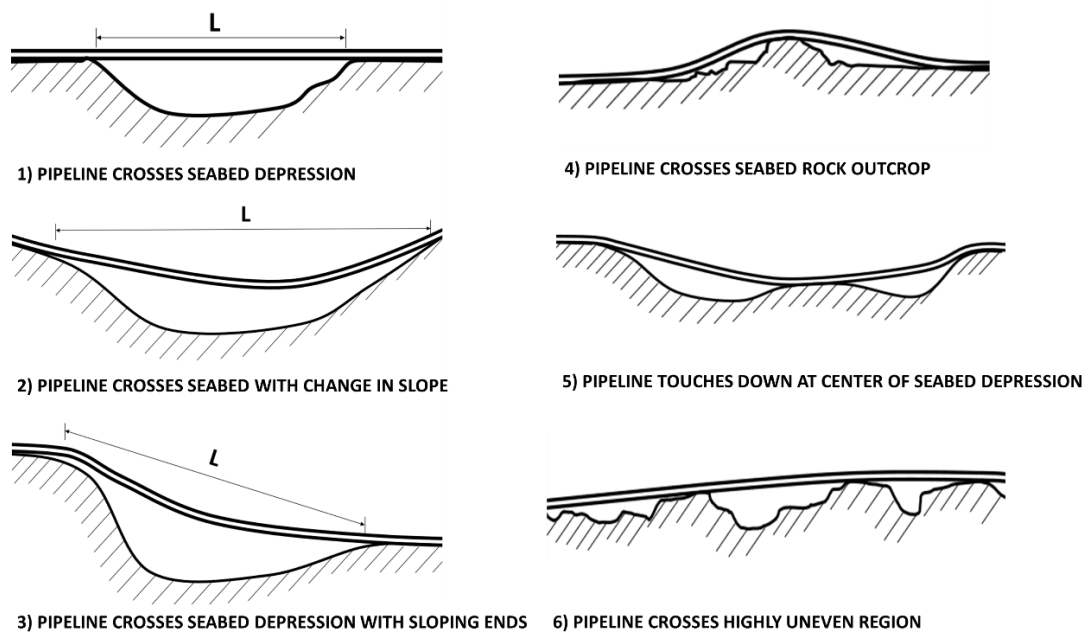
Figure 2-2: Types of single and multiple free-span configuration (Saheed Adekunle Shittu, 2022).

The distance between pipeline and seabed surface is one the important parameters in VIV fatigue damage. Due to the viscosity between the pipeline surface and ambient fluid, currents channeling between pipeline and seabed are to develop vertical velocity profile. In certain conditions where the height of the flow channel between pipeline and seabed is short, the velocity profile fails to fully develop. The unbalanced current speed in upper and lower sides of pipeline leads to unbalanced pressure profiles; therefore, Vortexes appeared in opposite sides are not equivalent and vortex-shedding cycle fails to complete (Abeele & Voorde, 2011; R. Yang et al., 2006).

A common method for applying VIV damage in pipeline design is to find maximum allowable length of span to limit VIV fatigue damage to comply with pipeline's expected operational life. Seabed intervention is a practical solution for conditions where span length exceeds maximum allowable length. The intervention is to change gap shape by techniques such as rock dumping to divide the long span into smaller spans or to completely fill the span (Q. Bai & Bai, 2014). Vortex suppression add-ons are another practical solution to prevent VIV damage to occur. The main idea behind development of suppressors is to eliminate destructive vibrations (Blevin, 1990; H. Choi et al., 2008; Rashidi et al., 2016; Skaugset, 2003).
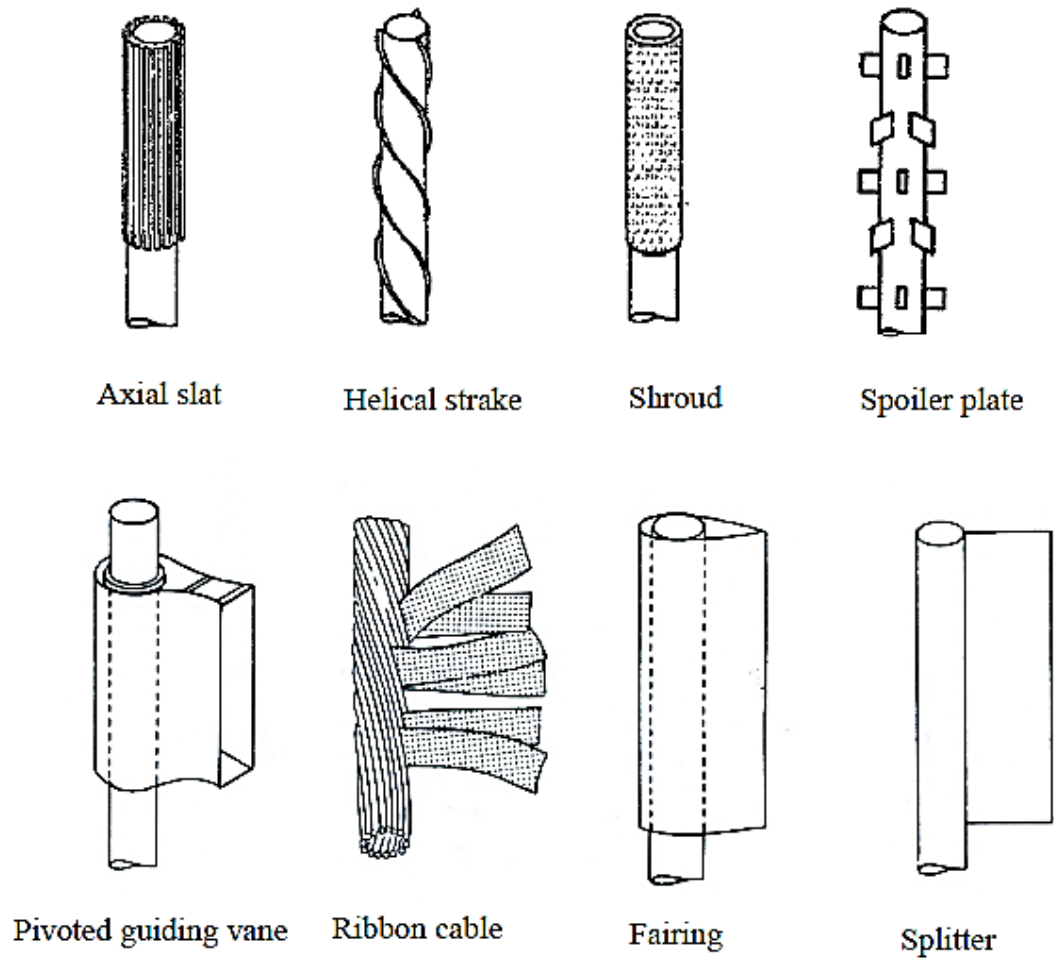
Figure 2-3: Different designs of VIV suppression add-ons (D. Blevin, 2001)

A comprehensive and correct analysis of VIV fatigue damage is one of the critical steps in any offshore pipeline project. Having a correct estimation about VIV fatigue damage might have a crucial impact of project overall cost. An over conservative design will unnecessarily inflate project costs while an underestimation can lead to failure before expected operational life. Determination of maximum span length against VIV fatigue failure has been target of numerous studies where some of them were to understand

pipeline behavior under free-spanning condition by indirect measurements (Bearman &
Zdravkovich, 1978; Fu et al., 2018; Lin et al., 2009).

2.3   Theory of Vortex Induced Vibration

Vortex shedding is a potential result of a condition where there is a blocking hinder along
streamline of a flow and fluid flows around the obstacle object. In this study, the pipeline
can be considered as a bluffing object.

The profile of the flow around the object is governed by Reynolds number. In cases where
Reynolds number is small, the flow is laminar and there is no other dynamic load except
stationary drag force. In contrast, for larger Reynolds numbers, the flow detaches from the
surface of bluffing object and forms a free shearing layer joining the main flow
downstream. For an unbounded stationary pipeline, the vortex shedding caused by vortices,
follows a repetitive pattern resulting a constant frequency of shedding (Kármán, 2012).

The repetitive pattern of vortices is called the Karman vortex street. Profile of the pressure
around the pipeline differentiates by alternation of vortices causing fluctuating drag and
lift forces on cylinder. While the frequency of altering lift force is equal to the frequency
of vortex shedding, the frequency of drag force fluctuation is twice the vortex shedding
frequency (Achenbach, 1968; Hans Drescher, 1956).
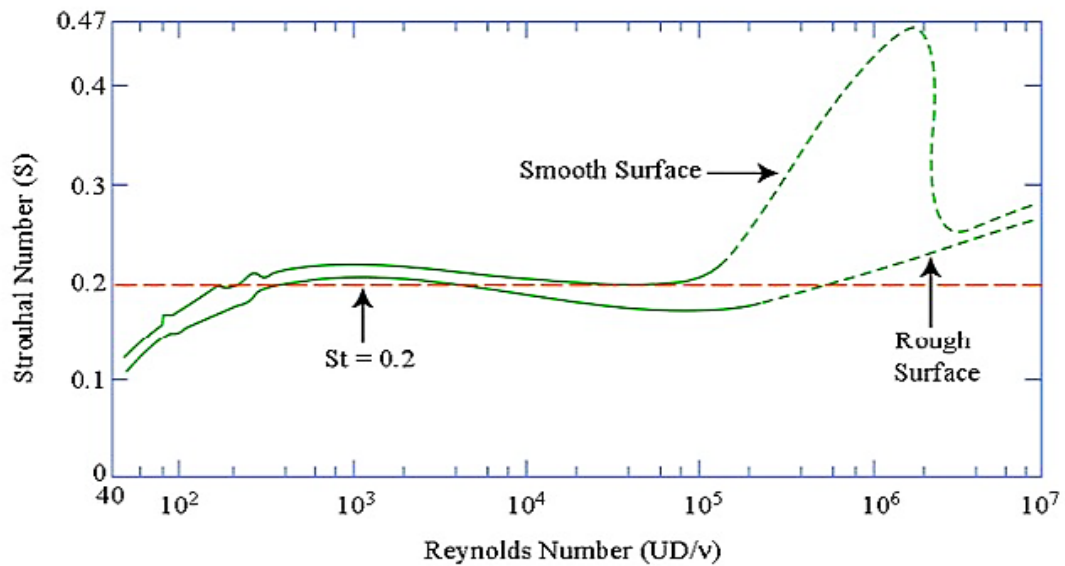
Figure 2-4: Relationship between Strouhal number and Reynolds number in a uniform flow over stationary cylinder (Achenbach & Heinecke, 1981).

Proximity to wall and the gap between pipeline and seabed can play a governing role by shaping the profile of flow regime around the pipeline. The gap between the pipeline and a plane wall directly affects the flow dynamics in the wake and consequently changes characteristics of vortex shedding. Even though probability of VIV in a pipeline close to the seabed is low, this configuration is particularly important for better understanding behavior of pipelines close to seabed (Salehi et al., 2018).

possibility of Vortex shedding in subsea pipelines can be categorized into three behavior zones including subcritical, trans-critical, and critical zones. These zones can be distinguished by the value of Reynolds number. In subcritical zone where Reynolds number is low, and the vortex shedding is unlikely to happen the Reynolds number is

smaller than 10^4. If the Reynolds number is in range of 10^4 to 10^7, the flow regime is mostly subcritical with minor overlap to trans-critical range (J. N. Song et al., 2011). For a cylindrical structure with no limiting boundary condition, by increase in Reynolds number, frequency of vortex-shedding can be close to the natural frequency of the structure which will lead into resonated vibration (Bourguet et al., 2011). Even though the Strouhal number is normally considered to be constant in the range of subcritical zone, but for a cylinder in vibration, due to unsteady vortices and wakes, the Strouhal number in subcritical zone changes respecting the condition of vortices and wakes; therefore, for cylindrical structures, Strouhal number for cylinders in subcritical zone cannot be considered as a constant value. In addition, vortex-induced vibration increases the strength of vortex shedding in wakes (Khalak & Williamson, 1999). In spite of the influence of the proximity to wall in suppression of vortex shedding, the vortex shedding always remains active for free cylinder even for conditions with zero gap ratio (B. Yang et al., 2009).

2.4   Experimental studies on Vortex Induced Vibrations

Experimental studies have been objective of wide range of studies where fluid-pipe interaction on a system of rigid cylinder laid on elastic foundation has been one the major topics of interest (J. Yang et al., 2012).This approach was conducted by simplifying a six degree of freedom flexible cylinders to one or two degree of freedom models. The approach of modeling cylindrical structures as rigid cylindrical bodies is an acceptable approach for modeling structures with moderate or low flexibility where the whole system is expected to behave as a one single entity (Elbanhawy, 2011). In cases where the aspect ratio is too large and the cylinder is significantly flexible, there mode shape and response might vary

along free-spanning length and full-scale experimental analysis is the only ideal option to study structural response against VIV vibrations (Hiramoto & Higuchi, 2003). An experimental study on stationary pipeline with high aspect ratio showed that such structure does not follow a unique response mode along pipeline. The study which conducted by flow visualization technique resulted in the fact that there is a span-wise changes in vortex shedding response and in cases where the pipeline is flexible and is fixed on both ends, multiple eignen frequencies and consequently multiple mode shapes is expected (Price et al., 2002). Experimental studies of fatigue due to VIV on risers have been studied by Trim et al (2005). Their model had aspect ratio of 1407 and value of $m^*\zeta$ of 0.0048 with a long flexible horizontal pipe exposed to uniform and sheared flow regimes with Reynolds number ranging from 12000 to 69000. Their study showed that within 0.1 of span length from tied end of riser is the most critical area for VIV responses.

Empirical analysis used to be the traditional method for analysis of VIV of free-spanning subsea pipelines. Regarding high uncertainty in empirical methods, analysis was in conjunct with high safety factors. Afterward, presence of cyclic vortex wake at downstream of cylindrical bluffing objects has been discovered which led to proposition of assumptions to simplify modeling of VIV analysis of cylinder. One early postulation was to assume wake as simple harmonic disturbances (Zhang et al., 2020b). Although employing this simplification made VIV analysis much easier and faster, the results were not accurate and reliable. Later on, a more accurate idea was to model hydrodynamic loads acting on free-spanning pipeline as sinusoidal force. In this model, free-spanning pipeline was modeled as a rigid cylinder with elastic support where the cylinder has one degree-of-freedom (Sumer & Fredsøe, 1990). This model was successfully verified by experimental data of

King (1974) for cases where stability parameter is in range of $K_s \geq 2$. Nowadays the accepted approach is to define VIV phenomenon as a nonlinear problem with multiple degrees of freedom rather than a simple small perturbation on a simple empirical model (Sarpkaya, 2004).By development of reliable experimental studies, the knowledge gained from experimental studies on stationary cylinder subjected to flow has been utilized in modeling of VIV. Application of experimental data in association with analytically developing equations governing behavior of free cylinder in flow led to proposition of semi-empirical models which were much more accurate than purely empirical models(Kurushina & Pavlovskaia, 2017). Modeling wake as nonlinear oscillation was one the areas significant improvements achieved using semi-empirical models (Y. Bai et al., 2015; Gabbai & Benaroya, 2005). The concept of modeling wake as wake oscillator was first introduced by Bishop and Hassan where they employed nonlinear oscillator of Van der Pol for modeling wake (Bishop & Hassan A Y, 1964).

Successful implementation of semi-empirical models positively encouraged the use of analytical relations in modeling. In order to couple wake oscillator model with structural analysis, displacement has been combined with wake oscillator model (Krenk & Nielsen, 1999). It also proved that time derivatives of displacement such as velocity and acceleration can also be useful for coupling structural analysis with wake oscillator (Blevin, 1990; Facchinetti et al., 2004; Mureithi et al., 2000; Plaschko, 2000).

Despite being a huge advancement at the time, the model of wake oscillator fails to perfectly illustrate all conditions of flow regime. In order to study conditions of flow regime such as low mass-damping ratio, cases where there is a proximity between cylinder

and a plane wall, and cases with two degree-of-freedom, the model of wake oscillator has been through some modifications to include Reynolds number and cover different configurations. In order to achieve higher precision in cases involving low mass-damping within sub-critical flow regimes, Farshidianfar and Zanganeh developed a model where response velocity is coupled with a model of elastically rigid cylinder exposed to the wake condition of Van der pol nonlinear oscillation (Farshidianfar & Zanganeh, 2010).

For the system of rigid cylinder mounted on elastic support with two degree-of-freedom, the coupling between streams-wise and transverse response plays a critical role. Experimental studies shows that the lock-in region in models with two degree-of-freedom one in stream-wise and one along transverse direction, is wider than the model where only one degree-of-freedom in transverse direction was allowed (Moe & Wu, 1990) Further conducted experimental studies demonstrated that the higher degree-of-freedom has no significant effect on width of lock-in region of cases with $m^* > 6$ (Williamson & Jauvtis, 2004). In cases where response in in-line and cross-flow are similar, the cross section of cylinder will follow a trajectory path forming a trace of figure 8 (Mode et al., 1994; Moe & Wu, 1990; Sarpkaya, 2004). Formation of figure 8 is shown in Figure 2-5.
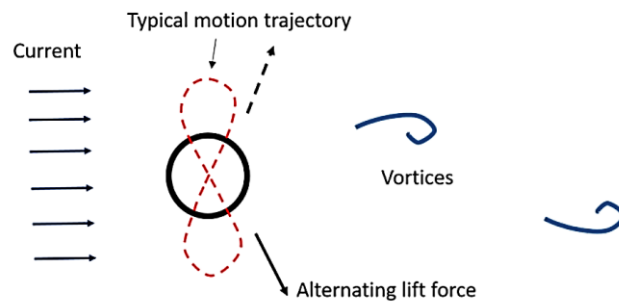
Figure 2-5: motion of figure 8 in VIV vibrations (Riemer-Sørensen et al., 2019).

By development of computational resources, analysis of response of pipeline structures against fatigue damage caused by vortex induced vibrations had rapidly improved and still is evolving. Regarding lack of detailed information about VIV, application of empirical methods and simplified modeling became conventional (Jo et al., 2002) In respect to high level of uncertainty, the projects designed with unnecessary expenses. Development of flow dynamic simulations and numerical analysis of structures paved the road for sophisticated modeling of vortex induced vibrations on freespanning pipelines. By advancement in modeling techniques of VIV phenomenon, seabed intervention as new method for reducing VIV damage on free-spanning pipeline has been introduced (Knoll & Herbich, 1980; Ole-Erik Vestøl Endrerud, 2013; Reid et al., 2000). Even though numerical models are considered to be most accurate, and their outcome are almost most cost-effective approach in project design, since numerical simulations require high computational resources and time-consuming solutions, classic methods are still relatively applicable. An algorithm for design procedure in VIV free-spanning pipelines is proposed by Kaneko et al (2014).

This study aims to a find a reliable and cost-effective solution by employing machine

learning methods on a database of results from validated numerical model.

2.5   Vortex Induced Vibration on subsea free-spanning pipelines.

In order to describe the behavior of a subsea pipeline under free-spanning condition, a guitar string can be a good resemble to analogically exemplify the free-spanning pipeline. The deflections of guitar strings are in format of mechanical waves with specific frequencies and modes. The pretension on guitar string controls the tones of resulting sonic wave which itself is categorized as a mechanical wave. The effect of pretension can similarly be an accumulated representative of sort mechanical factors such as internal pressure, external pressure, sagging, thermal expansion, and residual laying tension. The mechanical force applied by the musician on the guitar string can also be analogized by waves and current forces forcing the pipeline to vibrate. These vibrations can lead to pipeline to fail due to damages accumulated by numerous cyclic stresses (Ole-Erik Vestøl Endrerud, 2013).

2.6   Vortex Induced Vibration (VIV)

The length of the pipeline which is suspended above seabed can be modeled as a submerged cylinder. Waves and currents make the ambient fluid to flow around the cylinder; this phenomenon is called Vortex-Induced Vibration (VIV). Each case study of phenomenon of VIV falls into one of the two separate divisions; waves which have oscillatory flow and currents which have constant flow characteristics. Study cases studied in this research are assumed to be installed in deep waters, therefore; regarding theory of linearized wave, the impact of waves on pipeline can be neglected and current is the only assumed form of external force affecting pipeline.

2.7   Vortex shedding in pure current flow.

The flow passing surrounding a bluffing object (cylinder/pipeline in this study) is subjected to the friction force due to the resistance on the cylinder surface confronting flow of the fluid. Tis resistance to flow is called viscosity and in the real world, flow of a liquid on any surface has a degree of viscosity against it. Since viscosity prevents the fluid from slipping on the surface of the cylinder, a film of no-slip area is developed surrounding the cylinder which is called boundary layer. Within boundary layer, resistive viscous force is the dominant force, therefore; particles of fluid do not move and are statically attached to the submerged cylinder (Finnemore & Franzini, 2002). Regarding presence of boundary layer, there is a profile of gradient of speed in the flow where subsequently, an adverse pressure gradient is created. Because of the shear stress between fluid layers, different velocities of adjacent layers introduce the rotation in the fluid flow. The speed profile starts by zero on the surface of cylinder, then develops to transitional or turbulent range and finally reaches the current velocity.

When fluid overpasses through complex geometries such as pipe curvature, the boundary layers might be lifted off from the surface of boundary layer which leads wake areas to appear at downstream of the flow. In the wake zone, the fluid flow follows a recirculation pattern resulting in vortices and eddies downstream.

Within the boundary layer, particles of the fluid do not slip on the surface and therefore do not follow the movement pattern of fluid flow outside of the boundary layer. Regarding the different velocities inside and out of boundary layer, a friction force is enforced which decreases the velocity of flow layers and therefore, their mechanical energy.

Depending on the geometry of surface, the fluid might experience positive pressure gradient along flow-stream which is known as adverse pressure gradient. In cases where adverse pressure gradient increases along flow-stream and regarding the decrease in fluid velocity due to friction, at some point the pressure gradient will be strong enough to reverse direction of the velocity. The point where direction of movement switches is known as separation point.
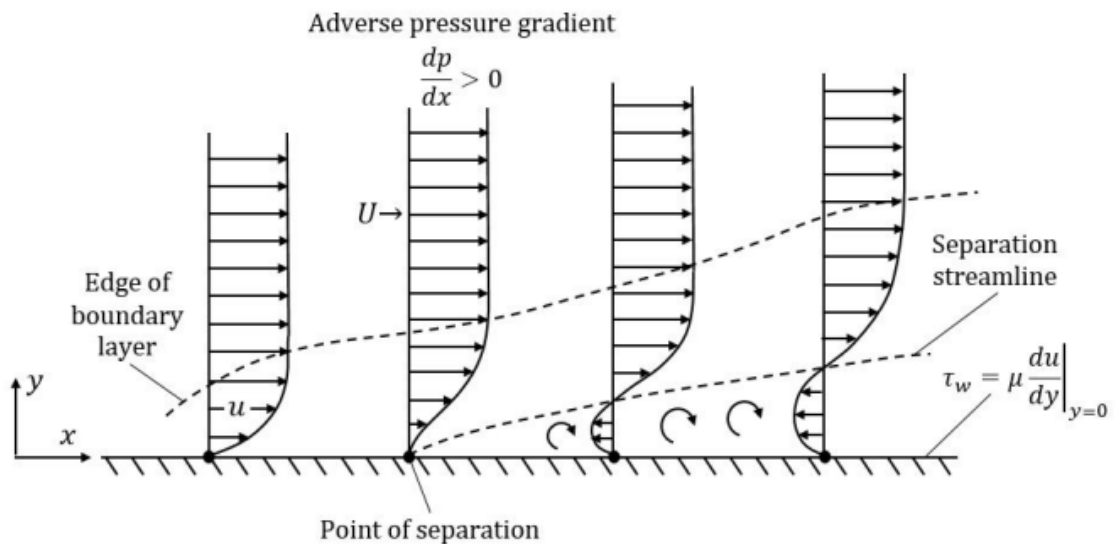

Figure 2-6: Development of boundary layer and separation point (Johnsson and Gunnarson, 2017).

In a fixed configuration of pipeline, fluid, and topography of cross-section, the transition from laminar flow to transitional and turbulent layers is depended to the flow velocity affecting Reynolds number. For low range of Reynolds number, fluid particles flow smoothly within a fixed layer and adjacent layers do not merge with each other. Laminar flow is mostly expectable for values of Reynolds number between 0 and 40 where

Reynolds number of zero refers to no-flow status. For higher range of Reynolds number from 40 to 200, the transitional range, vortices start to appear from the wake and form laminar vortex street (Sumer & Fredsøe, 2006). Formation of vortices from the upper and lower wake areas starts simultaneously, but for Reynolds number of 300 and higher, the vortex shedding is not coetaneous anymore, instead the vortex shedding alternates between upper and lower wake leading to vibration (Williamson, 1988). For pipelines, the Strouhal's number for flow regimes with Reynolds number between 300 to 3×10^5 can fairly be assumed consistent 0.2, where higher end of the range is the higher end of subcritical flow range (Sumer & Fredsøe, 2006).Within the aforementioned range, the power spectra is at highest peak value at value of $St = 0.2$ (Schewe, 1983). A further increase in Reynolds number transforms the flow regime from subcritical to supercritical where the Strouhal number jumps from 0.2 to 0.7 and amplitude of vibration noticeable decreases.

2.8   Vortex shedding for combination of current and wave flow.

The ambient water particles follow elliptical orbital path which can be mathematically represented with trajectory components of x and z where, for deep waters, this motion can be described by formula below (Journee & Massie, 2001):

$$(x - x_0)^2 + (z - z_0)^2 = (\xi. e^{k_\omega z_0})^2 \qquad (2\text{-}1)$$

Where x and z are horizontal and vertical coordinates. x_0 and z_0 are coordinates of center of circle, ξ is the displacement amplitude, and k_ω is the wave number. For describing an oscillatory flows like wave situation, the number of Keuligan-Carpenter (KC) is widely applicable. The lower value of KC indicates that separation of boundary layers is unlikely to happen and magnitude of the motion orbital of water particles is small. Larger values of KC indicates that the flow amplitude of oscillatory motion of flow is larger than pipeline diameter and the there is a higher probability of vortex shedding to occur (Rao, S., & Yap, 2011) .Based on the information presented in Figure 2-7 for KC >7, vortex shedding is expected. Flow regimes around bluffing cylinder exposed to current flow are listed in Figure 2-7.
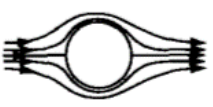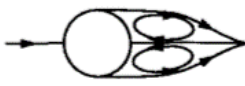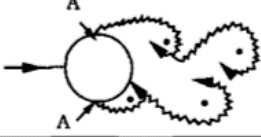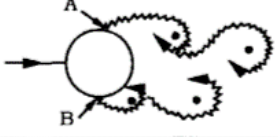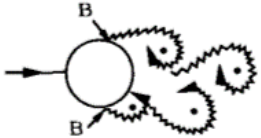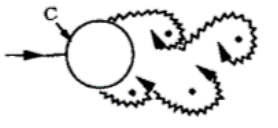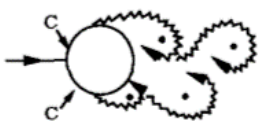
a)	No separation. Creeping flow	Re < 5
b)	A fixed pair of symmetric vortices	5 < Re < 40
c)	Laminar vortex street	40 < Re < 200
d)	Transition to turbulence in the wake	200 < Re < 300
e)	Wake completely turbulent. A:Laminar boundary layer separation	$300 < Re < 3 \times 10^5$ Subcritical
f)	A:Laminar boundary layer separation B:Turbulent boundary layer separation;but boundary layer laminar	$3 \times 10^5 < Re < 3.5 \times 10^5$ Critical (Lower transition)
g)	B: Turbulent boundary layer separation;the boundary layer partly laminar partly turbulent	$3.5 \times 10^5 < Re < 1.5 \times 10^6$ Supercritical
h)	C: Boundary layer completely turbulent at one side	$1.5 \times 10^6 < Re < 4 \times 10^6$ Upper transition
i)	C: Boundary layer completely turbulent at two sides	$4 \times 10^6 < Re$ Transcritical

Figure 2-7: Flow regimes for a constant current around a pipeline (Sumer & Fredsøe, 2006).

2.9　Non-dimensional parameters

In fields of fluid mechanics and fluid dynamics due to large size of subjects and complexity in fluid dynamics, experimental evaluation of the phenomenon is difficult and, in some cases, impossible to perform. In this regard, non-dimensional parameters such as Reynolds number are effective approach in analysis of complex fluid dynamics and fluid mechanics problems. Since analysis of VIV fatigue in free-spanning pipelines requires fluid dynamics, fluid-solid interaction, and structural dynamics, application of dimensionless parameters is inevitable (Sumer & Fredsøe, 2006). Required dimensionless parameters are introduced in follow.

2.9.1　Aspect ratio

The parameter aspect ratio is the ratio of span length over pipe's outer diameter. This parameter has dimension of $\left(\frac{L}{L}\right)$. This parameter is defined in equation below:

$$Aspect\ ratio = \frac{L_{span\ lenght}}{D_{pipe}} \tag{2-2}$$

2.9.2　Gap aspect ratio

Gap aspect ratio is the ratio of gap between pipeline and seabed over outer diameter of pipeline. This parameter controls the development of fluid layers.

$$Gap\ ratio = \frac{e}{D} \tag{2-3}$$

The target flow regime in this research is the current flows and selected gap ratios are all greater than the critical value of $\frac{e}{D} = 0.3$; therefore, impact of gap ratio on VIV stresses

31

and consecutively, VIV fatigue life is expected to be inadmissible. Despite having minimum effect on VIV fatigue performance, in cases with high span aspect ratio and low span depth, it's possible for vibration amplitude be greater than size of gap depth. Collision of vibrating pipeline and seabed might severely damage pipeline structure. In this research collision of pipeline and seabed is considered an immediate failure.

2.9.3 Reynolds number

Reynolds number is the ratio of inertia force over viscous force. Reynolds number for pipeline can be calculated by formula below:

$$Reynolds = \frac{\rho U_\infty D}{\mu} \tag{2-4}$$

2.9.4 Reduced Velocity

Reduced velocity is defined as ratio of ambient current velocity to the product of pipeline's outer diameter and structural natural frequency in free-spanning length.

$$v_r = \frac{U_\infty}{f_n D} \tag{2-5}$$

2.9.5 Mass ratio

Mass ratio is mass per unit of length of pipeline to the mass of fluid displaced by unit length of pipeline. This parameter is presented below:

$$m^* = \frac{m}{\rho D^2} \tag{2-6}$$

Where m is the total mass of pipeline.

2.9.6 Damping ratio

Damping is the suppression of an oscillatory movement. This influence can affect gradually or act by total prevention of oscillation. Damping is a collective parameter and total damping ratio is summation of damping in all individual element of structure.

$$\zeta_T = \sum \zeta_1 + \zeta_2 + \cdots \tag{2-7}$$

2.9.7 Strouhal number

This non-dimensional parameter is the normalized shedding frequency around the pipeline and is normalized by using current velocity U_∞ and pipeline's outer diameter.

$$S_t = \frac{fD}{U_\infty} \tag{2-8}$$

2.9.8 Keulegan-Carpenter's Number

This number is the ratio of the drag force caused by steady currents, to the inertia force imposed on the structure. This parameter is dimensionless and can be calculated by equation below:

$$KC = \frac{U_m T}{D} \tag{2-9}$$

Where T is the period of the oscillation.

2.9.9 Multi-span relative aspect ratio

This parameter is only applicable in multi-spanning condition where there are two neighboring spans divided by a shoulder. Since neighboring spans can interact with each other, this parameter is proposed for better understanding of interaction between neighboring spans. This parameter will be used in training Machine Learning (ML) models. For a pair of neighboring spans, this parameter is defined as length of longer span to the length of shorter span.

$$L_R = \frac{L_{max}}{L_{min}} \tag{2-10}$$

2.9.10 Multi-span shoulder aspect ratio

This dimensionless parameter is also can specifically be defined for multi-spanning condition. The Multi-span shoulder ratio is the ratio of total spanning length of two neighboring spans to length of shoulder. This parameter can be a good representation for static gravity driven stress on pipeline in shouldering length. The parameter can be calculated by equation below:

$$L_{sh} = \frac{L_{max} + L_{min} + L_{shoulder}}{L_{shoulder}} \tag{2-11}$$

Where $L_{shoulder}$ is length of the shoulder in a multi-spanning setup.

2.9.11 Stability parameter

Stability parameter K_s represents the damping for a given modal shape and can be calculated by equation (2-12).

$$K_s = \frac{4\pi m_e \zeta_T}{\rho D^2} \qquad (2\text{-}12)$$

Where ρ the density of ambient water, D is is the pipe diameter and m_e is the effective mass including the added mass. Coefficient of added mass and its calculation procedure based on reduced velocity is described in detail in DNV RP-F105.
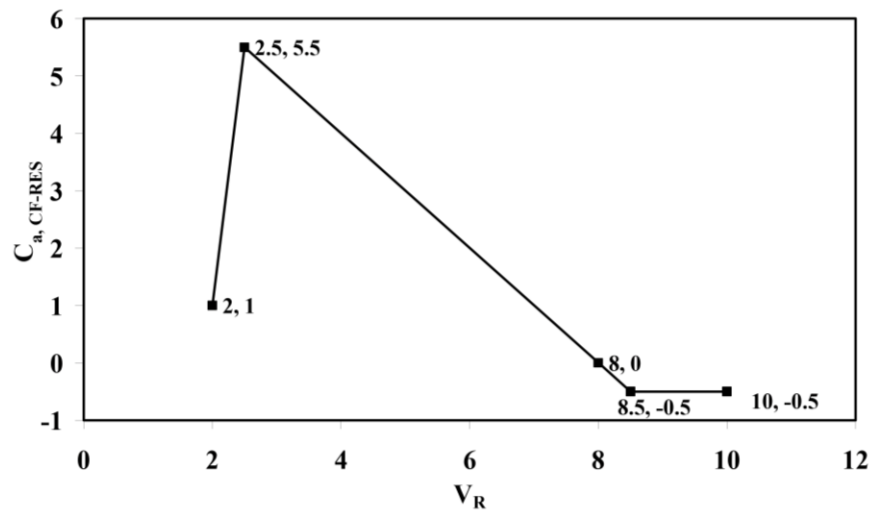

Figure 2-8: Added mass coefficient in cross-flow direction in respect to reduced velocity

(DET NORSKE VERITAS, 2021).

2.9.12 Inverse of wall thickness ratio

Pipeline performance against shear, hoop, and other forms of stresses is highly dependent on wall thickness. Due to higher density of steel, high thickness of pipe significantly increases structural weight but on the other hand, improves pipes strength. Since non-dimensional parameters have higher compatibility with machine learning methods, the non-dimensional parameter of inverse wall thickness ratio is proposed.

$$inverse\ of\ wall\ thickness\ ratio = \frac{D}{t} \qquad (2\text{-}13)$$

Where t is the wall thickness.

2.10   Forces on subsea free-spanning pipeline

A free-spanning subsea pipeline can be modeled as a submerged cylinder where there are two main forces perpendicularly exerting on the cylinder. Namely drag force and the lift force are the acting forces in in-line and crossflow directions respectively. The in-line drag force is applied parallel to the fluid flow from upstream to downstream on the pipeline section where lift force acts in the direction perpendicular to the drag force. There is a significant difference between forces originated by current flow and forces emerged due to oscillatory flows such as waves.

2.11   Forces in pure current situation

The total drag force acting on pipeline consists of two elements of pressure drag force and frictional drag force. In flows within the range of subcritical flow regime where Reynolds number falls in range of $300 < Re < 2 \times 10^5$, contribution of frictional drag force to total drag force is about 2-3%; therefore, impact of friction drag force can be neglected (Sumer & Fredsøe, 2006).

The pressure drag force is the conclusive of two opposing forces applied on pipeline in the direction of crossing fluid flow. The smaller force has a direction opposing the flow direction and is a result of presence of wake area downstream side of pipeline. The velocity at the wake area behind the pipeline is lower than the area outside of the wake, where based on Bernoulli principle, pressure in wake area is higher than no-wake area resulting a pushing force against flow direction. However, the pressure drag force, which is result of change in momentum of fluid stream interacting with the pipeline at stagnation point of pipeline front (upstream), is larger than the opposing force and the conclusive drag force is toward the downstream of pipeline. Depending on vortex shedding, pressure drag can be fixed or be time variant by absence or presence of vortex shedding respectively. Since within every single vortex shedding, the pressure drag completes a full cycle; In case of vortex shedding, frequency of drag force will be twice the frequency of vortex shedding. Vibration amplitude for in-line vibrations is noticeably smaller than those of cross-flow vibrations.

For Reynolds numbers larger than 40, the upward and downward lift forces acting in cross-flow direction occur in alternating sequence. The fluctuation in distribution of pressure is

the factor controlling the sequence of upward and downward forces. Upward lift force occurs synchronously when the vortex from lower wake is created, and the downward lift force happens when the vortex from upper wake is created.

Alternation of lift forces lead to creation of cross-flow vibration which will have frequency identical to shedding frequency. Flow regimes around a pipeline subjected to waves are described in Figure 2-9. Distribution of pressure around the pipeline in subject to current flow is presented in Figure 2-10.
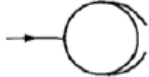
a)	No separation. Creeping (laminar) flow.	KC < 1.1
b)	Separation with Honji vortices. See Figs. 3.3 and 3.4	1.1 < KC < 1.6
c)	A pair of symmetric vortices	1.6 < KC < 2.1
d) A	A pair of symmetric vortices. Turbulence over the cylinder surface (A).	2.1 < KC < 4
e)	A pair of asymmetric vortices	4 < KC < 7
f)	Vortex shedding	7 < KC Shedding regimes

Figure 2-9: Flow regimes around subsea pipeline subjected to waves (Sumer & Fredsøe, 2006).
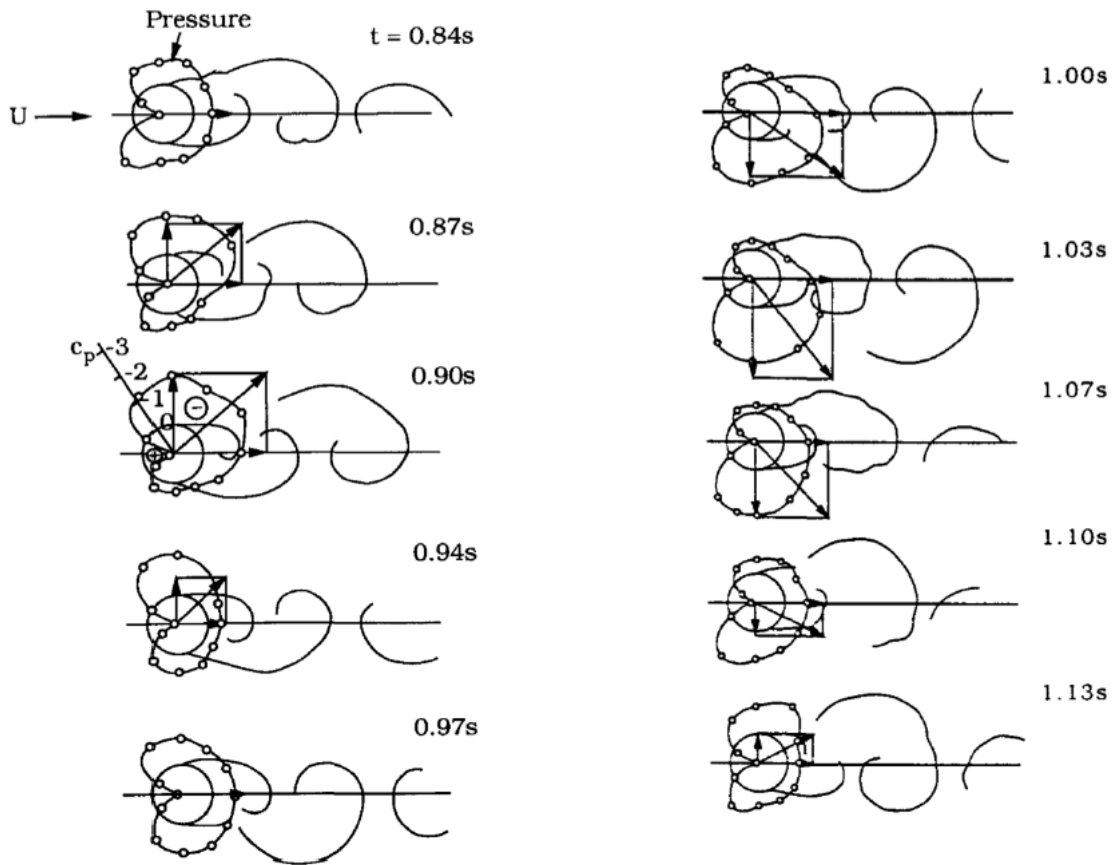
Figure 2-10: Distribution of pressure around a pipeline subjected to pure current flow

(Sumer & Fredsøe, 2006).

2.12 Forces in pipeline subjected to wave.

Pipelines subjected to waves have all the lift and drag forces applied to cases subjected to pure current flow. In addition, waves as oscillatory flow regime, impose extra forces as hydrodynamic mass force known as added mass force and the Frude-Krylov force.

Total in-line force can be calculated by Morison's equation as follows (Morison et al., 1950).

$$F_{IL} = \frac{1}{2}\rho C_D DU|U| + \rho C_m A\dot{U} + \rho A\dot{U}$$

(2-14)

Where the C_D is the drag coefficient, ρ is the density of fluid, D is size of outer diameter of pipeline, U is the flow rate, and C_m is the hydrodynamic mass coefficient where for smooth surface of pipeline and low KC, we have $C_m = 1$ (Sumer & Fredsøe, 2006) where equation (2-14) can be reformatted into equation below:

$$F_{IL} = \frac{1}{2}\rho C_D DU|U| + \rho C_M A\dot{U}$$

(2-15)

The first expression is the drag force component F_D and the second expression represents the inertia force F_I.

$$F_D = \frac{1}{2}\rho C_D DU|U|$$

(2-16)

$$F_{IL} = \rho C_M A\dot{U}$$

(2-17)

The C_M is the inertia coefficient and can be calculated as below:

$$C_M = C_a + 1$$

(2-18)

Linear wave theory assumes displacements to be harmonic and velocity and acceleration have a phase difference of 90^0 with each other. These two variables are time derivatives of displacement. In regard to the phase difference, it is impossible to have maximum drag force and maximum inertia force at the same time. For small values of KC, the ratio between inertia and drag forces can be achieved by formula below:

$$\frac{F_I}{F_D} = \frac{C_M \frac{\pi}{4} D^2 \omega U}{\frac{1}{2} C_D D U^2} = \pi^2 \frac{D}{U T_\omega} \frac{C_M}{C_D} = \frac{\pi^2}{KC} \frac{C_M}{C_D}$$

(2-19)

Where ω is the angular velocity. This equation can be simplified by replacing appropriate values for circular cylinder. The rewritten form of the equation (2-19) for pipeline as circular cylinder is as follows.

$$\frac{F_{I,\text{max}}}{F_{D,\text{max}}} = \frac{\pi^2}{KC} \frac{2}{1} \approx \frac{20}{KC}$$

(2-20)

Based on the equation (2-20), it can be concluded that for lower values of KC the inertia force is larger than drag force. For flow regimes with KC < 4, there is no vortex shedding and consequently the vertical force component will be zero. Vortices start to appear from regimes with KC > 4 and from KC >7, oscillatory lift force emerges. The frequency of oscillation of lift force is in direct relationship with KC and increase by increase in value

of KC and is not depended to wave's frequency(Sumer & Fredsøe, 2006). The largest

possible lift force can be driven from the equation below:

$$F_{L,\max} = \frac{1}{2}\rho C_{L,\max} DU_m^2 \qquad (2\text{-}21)$$

Where $C_{L,\max}$ stands for maximum lift force coefficient. Based on experimental data,

maximum value for lift force coefficient can be reached at KC 10 and Reduced velocity Vr

= 6.

2.13 Vibrations of subsea free-spanning pipelines

As mentioned before, this study is mainly focused on fatigue damages enforced by VIV

vibrations due to pure current flow, where based on the solution methods recommended in

DNV RP-F-105, the natural frequency of pipeline critically affects the pipeline's behavior

against VIV vibration.

2.14 Natural Frequency of Euler-Bernoulli beam

For any mechanical system there is a natural frequency where if there is no dissipation of

energy, by adding an initial energy in form of force or displacement, the system will start

to vibrate continuously and for indefinite times of cycles. In the real world, it is impossible

to completely avoid energy loss within a cycle, therefore; all of mechanical systems are

subjected to energy dissipation where this loss of energy is represented as the damping

effect. Natural frequency is the frequency where the energy can be transferred to the mechanical system at a high rate. High amounts of energy transferred to the system will lead to larger amplitude of vibration causing severe damage to the structure.

In order to find the natural frequency of a system, i.e., free-spanning section of the subsea pipeline, the equation of eigenvalues needs to be solved.

$$(\lambda[k] - [m])\vec{W} = \vec{0}$$

<div align="right">(2-22)</div>

Where k and m are stiffness and mass respectively and $[k]$ and $[m]$ are stiffness matrix and mass matrix respectively and λ can be defined as below:

$$\lambda = \frac{1}{\omega^2}$$

<div align="right">(2-23)</div>

The λ is inverse of the eigenvalue ω^2. $\vec{W}$ represents mode shape of system which is form of displacement of the system when vibrating in natural frequency. The natural frequency of the system is represented by ω and can be referred as f_n.

$$\vec{W} = \begin{Bmatrix} W_1 \\ W_2 \\ W_3 \\ \dots \\ W_n \end{Bmatrix}$$

<div align="right">(2-24)</div>

The $\vec{0}$ is the null vector.

$$\vec{0} = \begin{Bmatrix} 0 \\ 0 \\ 0 \\ \dots \\ 0 \end{Bmatrix}$$

(2-25)

The formula of eigenvalues can also be written as follows:

$$(\lambda[I] - [D])\vec{W} = \vec{0}$$

(2-26)

Where the $[I]$ represents identity matrix and $[D]$ can be calculated as below:

$$[D] = [k]^{-1}[m]$$

(2-27)

As a trivial solution, the matrix $\vec{W}$ is set to be zero. In order to attain a general solution, non-trivial conditions need to be solved which results in the equation which makes the determinant zero.

$$|\lambda[k] - [m]| = 0$$

(2-28)

A modern approach to solve natural frequency and mode shape of mechanical systems is to employ finite element methods (FE). The FE method has successfully replaced experimental approaches conducted on mechanical and structural systems.
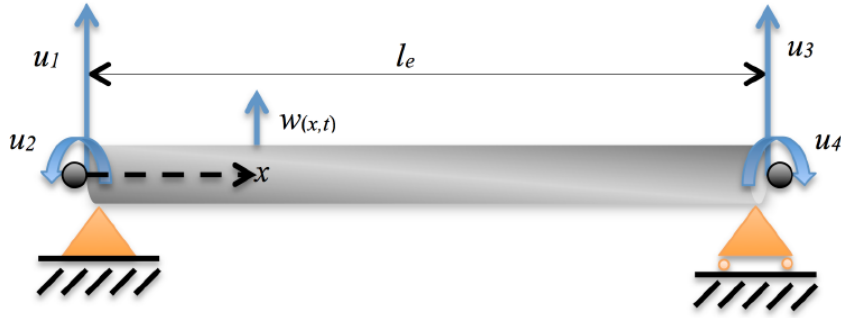
Figure 2-11: Schematic of a Euler-Bernoulli beam (Ole-Erik Vestøl Endrerud, 2013).

In finite element method nodes are geometrically defined points where field variables are explicitly calculated. Elements can be defined by the nodal points assigned to it. In a three-dimensional model, each node of an element has six degrees of freedom at least. These degrees of freedom define location (u_x, u_y, u_z) and angular position $(\theta_x, \theta_y, \theta_z)$. Elements are connected to each other via common nodes between them.

As an example, a simple model with one element for free-spanning length of pipeline is considered. For one single element, local and global coordination systems are equal to each other. In order to find mass and stiffness matrixes in global coordination, terms of kinetic and potential energy have to be determined. Assuming free-spanning length of pipeline to behave as a Euler-Bernoulli beam, the mass [M] and stiffness matrixes [K] can be achieved as below:

$$[K] = \frac{EI}{l_e^3} \begin{bmatrix} 12 & 6l_e & -12 & 6l_e \\ 6l_e & 4l_e^2 & -6l_e & 2l_e^2 \\ -12 & -6l_e & 12 & -6l_e \\ 6l_e & 2l_e^2 & -6l_e^2 & 4l_e^2 \end{bmatrix} \qquad (2\text{-}29)$$

45

$$[M] = \frac{\rho A_e l_e}{420} \begin{bmatrix} 156 & 22l_e & 54 & -13l_e \\ 22l_e & 4l_e^2 & 13l_e & -3l_e^2 \\ 54 & 13l_e & 156 & -22l_e \\ -13l_e & -3l_e & -22l_e & 4l_e^2 \end{bmatrix} \tag{2-30}$$

Where A_e is the cross-sectional area of the element, l_e is the length of the element, and ρ is mass density. Since local and global coordination systems are equal, we have $u_1 = W_1$ and $u_2 = W_2$ and so on. Considering the simply supported boundary condition for both ends of the element of free-spanning length we have $W_1 = 0$ and $W_3 = 0$, therefore; columns 1 and 3 and rows 1 and 3 can be deleted. By deletion of zero values, stiffness and mass matrixes can be rewritten in simplified form.

$$[K] = \frac{2EI}{l_e} \begin{bmatrix} 2 & 1 \\ 1 & 2 \end{bmatrix} \tag{2-31}$$

$$[M] = \frac{\rho A_e l_e^3}{420} \begin{bmatrix} 4 & -3 \\ -3 & 4 \end{bmatrix} \tag{2-32}$$

In order to find eigenvalues of system we need to sole the determinant equation which we will have:

$$\begin{vmatrix} 2 - 4\lambda & 1 + 3\lambda \\ 1 + 3\lambda & 2 - 4\lambda \end{vmatrix} = (2 - 4\lambda)^2 - (1 + 3\lambda)^2 = 3 - 22\lambda + 7\lambda^2 \tag{2-33}$$

By solving this equation, natural frequencies of beam can be obtained.

$$\lambda_1 = \frac{1}{7} => \omega_1 = \sqrt{\frac{120EI}{\rho A_e l_e^4}} \tag{2-34}$$

46

$$\lambda_2 = 3 = \omega_3 = \sqrt{\frac{2520EI}{\rho A_e l_e^4}} \qquad (2\text{-}35)$$

Accuracy of finite element method can be improved by increase in number of elements. By increase in accuracy of numerical analysis, accuracy of natural frequencies will also improve.

2.15 Natural modes and mode shapes

For every natural frequency of a mechanical system, there is a matching form of deformation which is known as mode shape. The mode shape is a vector representing deformation and amplitude of the element, where in this specific case, mode shape indicates movement and amplitudes of pipeline. Furthermore, the order of the mode in its direction can indicate the status of symmetricity of mode shape where even modes are all symmetric and off modes are asymmetric. First three mode shapes of a pipeline are presented in Figure 2-12.
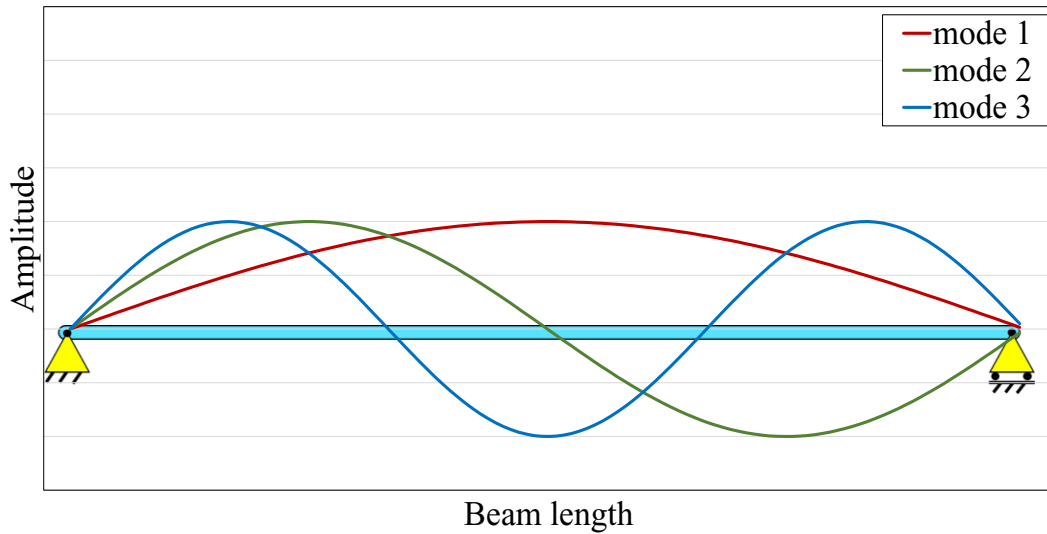
Figure 2-12: First three mode shapes of free-spanning pipeline - beam.

These vibration modes are only in effect when there is a vortex shedding in pipeline. In order to find whether vortex shedding occurs or not, the parameter of reduced velocity has to be calculated and compared with threshold criteria provided by DNV RP-F-105.

In mechanical systems, the natural frequency of first mode shape is the smallest natural frequency of system. The mechanical system of a pipeline has two different group of natural frequencies and mode shapes which are perpendicular to each other. Natural frequencies of modes shapes of deflection along current flow are in-line natural frequencies and corresponding mode shapes are in-line mode shapes. The group of cross-flow mode shapes are mode shapes are natural shapes in direction perpendicular to in-line modes and their corresponding frequencies are cross-flow natural frequencies. In order to vortex shedding to have effect on pipeline, the following criteria has to be fulfilled by first natural frequencies in either of in-line or cross-flow directions. If first natural frequency in in-line

or cross-flow direction fails to meet the criteria, it is not expected to have VIV in that direction. The VIV occurrence criteria defined by DNV is presented (DET NORSKE VERITAS, 2021)

$$f_{IL,1} > \frac{U_{extreme}\gamma_{f,IL}}{V_{R,onset}^{IL}D} \tag{2-36}$$

$$f_{CF,1} > \frac{U_{extreme}\gamma_{f,CF}}{2D} \tag{2-37}$$

Where $U_{extreme}$ is the flow condition based on characteristic environmental events. $f_{IL,1}$ and $f_{CF,1}$ are first natural frequencies in in-line and cross-flow directions respectively. $\gamma_{f,IL}$ and $\gamma_{f,CF}$ are safety factors of natural frequency in in-line and cross-flow directions respectively, $V_{R,onset}$ is the onset value for reduced velocity in in-line direction, and D is the hydrodynamic diameter of pipe which is the outer diameter including concrete layer.

The value of $U_{extreme}$ can be calculated based on possibility of occurrence of wave and current conditions at pipe level.

$$U_{extreme} = \max(U_{c,100-year} + U_{w,10-year}, U_{c,10-year} + U_{w,100-year}) \tag{2-38}$$

Where we have:

$U_{c,i-year}$= value of the perpendicular component of current with return period of i-year.

49

$U_{w,i-year}$= value of the perpendicular component of significant wave with return period of i-year.

Safety factors for natural frequencies in in-line and cross-flow directions are provided.

Table 2-1: Safety factors for natural frequencies in in-line and cross-flow directions (DET NORSKE VERITAS, 2021).

Free span classifications	Safety class					
	Low		Medium		High	
	$\gamma_{f,IL}$	$\gamma_{f,CF}$	$\gamma_{f,IL}$	$\gamma_{f,CF}$	$\gamma_{f,IL}$	$\gamma_{f,CF}$
Very well defined	1.0	1.0	1.0	1.0	1.0	1.0
Well to very well defined	1.0	1.0	1.0	1.1	1.0	1.15
Well defined	1.05	1.05	1.1	1.1	1.15	1.15
Not well defined	1.1	1.1	1.2	1.2	1.3	1.3

2.16 Modeling of free-spanning pipeline

The behavior of pipeline in free-spanning condition is in heavy dependence to span aspect ratio, which is the relative length of span to pipe diameter and has been previously introduced as a non-dimensional parameter. Based on semi-empirical practice introduced by DNV, behavior of the pipeline can be classified into three major categories known as cases with minor dynamic amplification, cases where the behavior of the beam can be

approximated by beam elements, and cases where the pipeline performance is similar to behavior of a cable. In general, by increase in value of aspect ratio, the level of dynamic resonation of pipeline increases. For smaller range of aspect ratio $L/D < 30$, performance of pipeline is mainly governed by static responses of the structure and there is no significant dynamic response. For large and extremely large values of pipeline, behavior of the pipeline can be approximated beam and cable responses respectively. In this research length of free-spanning section fulfills criteria of beam behavior.

Depending on the seabed's stiffness, the subsea pipeline laid on the seabed soil is subjected to a level modal damping. Seabed characteristics including cohesiveness, degree of stiffness and type of seabed as sand or clay are effective parameters on soil damping. Penetration of pipeline on soil and Coulomb friction are two main reasons for the creation of soil damping. Interaction between pipe and soil can be modeled by determining dynamic soil stiffness values in three orthogonal directions. In order to obtain values of soil stiffness, coulomb friction theory can be employed. Values of soil dynamic stiffness based have been provided in DNV RP-F-105 and DNV RP-F-114. The lateral and vertical soil stiffness parameters can be calculated by dynamic stiffness factors.

$$K_{v,d} = \frac{C_V}{1 - v} \left(\frac{2}{3} \frac{\rho_s}{\rho} + \frac{1}{3} \right) \sqrt{D} \qquad (2\text{-}39)$$

$$K_{L,d} = C_L(1 + v) \left(\frac{2}{3} \frac{\rho_s}{\rho} + \frac{1}{3} \right) \sqrt{D} \qquad (2\text{-}40)$$

Where C_V and C_L are simplified dynamic stiffness factors for pipe-soil interaction and can be found on Table 2-2 and Table 2-3. ρ_s is the density of steel (DNVGL RP-F114, 2017).

Table 2-2:Simplified stiffness factors for pipe-soil interaction in sand (Det Norske

Veritas Germanischer Lloyd (DNV GL), 2017)

Sand type	Fraction angle, ϕ $[\ ^o]$	C_V $\left[kN/m^{\frac{5}{2}}\right]$	C_L $\left[kN/m^{\frac{5}{2}}\right]$	$K_{V,S}$ $[kN/m/m]$
Loose	28-30	10500	9000	250
Medium	30-36	14500	12500	530
Dense	36-41	21000	18000	1350

Table 2-3: Simplified stiffness factors for pipe-soil interaction in clay with OCR=1 (Det Norske Veritas Germanischer Lloyd (DNV GL), 2017)

Clay type	Undrained shear strength, s_u [kN/m^2]	C_V $\left[kN/m^{\frac{5}{2}}\right]$	C_L $\left[kN/m^{\frac{5}{2}}\right]$	$K_{V,S}$ [$kN/m/m$]
Very soft	< 12.5	600	500	50-100
Soft	12.5-25	1400	1200	160-260
Firm	25-50	3000	2600	500-800
Stiff	50-100	4500	3900	1000-1600

Where OCR is the over-consolidation factor and for non-cohesive soil is OCR = 1. The parameter $K_{V,S}$ is the static soil stiffness. For pipe-soil interaction along axial direction of pipe, the soil stiffness in axial direction can be taken equal to lateral soil stiffness (Det Norske Veritas Germanischer Lloyd (DNV GL), 2017)

Detailed calculation of soil stiffness requires thorough geotechnical investigations on the very specific location of interest. Regarding complicated and perplexing procedure required for accurate calculation of soil parameters, typical values provided by DNV RP-F105 and DNV RP-F114 can be reasonable choices to use.

2.17 Theory of fatigue life assessment.

Damages dues to VIV in free-spanning sections of pipelines can lead the pipeline to fail before expected operational life. VIV failure might be a result of lock-in region or accumulative fatigue damages during long term exposures. The fatigue summation method of Palmgren-Miner can be employed for calculation of the accumulated fatigue damages by VIV loads in free-spanning areas. The Palmgren-Miner equation is demonstrated in equation (2-41).

$$D_{acc} = \sum_{i=1}^{N} \frac{n_i}{N_{fi}} = \frac{1}{a} \sum_{i=1}^{N} n_i \, (\Delta\sigma_i)^m \tag{2-41}$$

Where a and m parameters are the interception of the design S-N curve with the log of N axis and negative inverse slope of the S-N curve respectively and can be extracted from S-N curve diagrams available for pipeline material. The parameter n is number of stress cycles applied on pipeline and the parameter N_f is the total number of stress cycles on pipeline system to fail. Finally, the parameter D_{acc} represents total accumulation of fatigue damages imposed on structure.
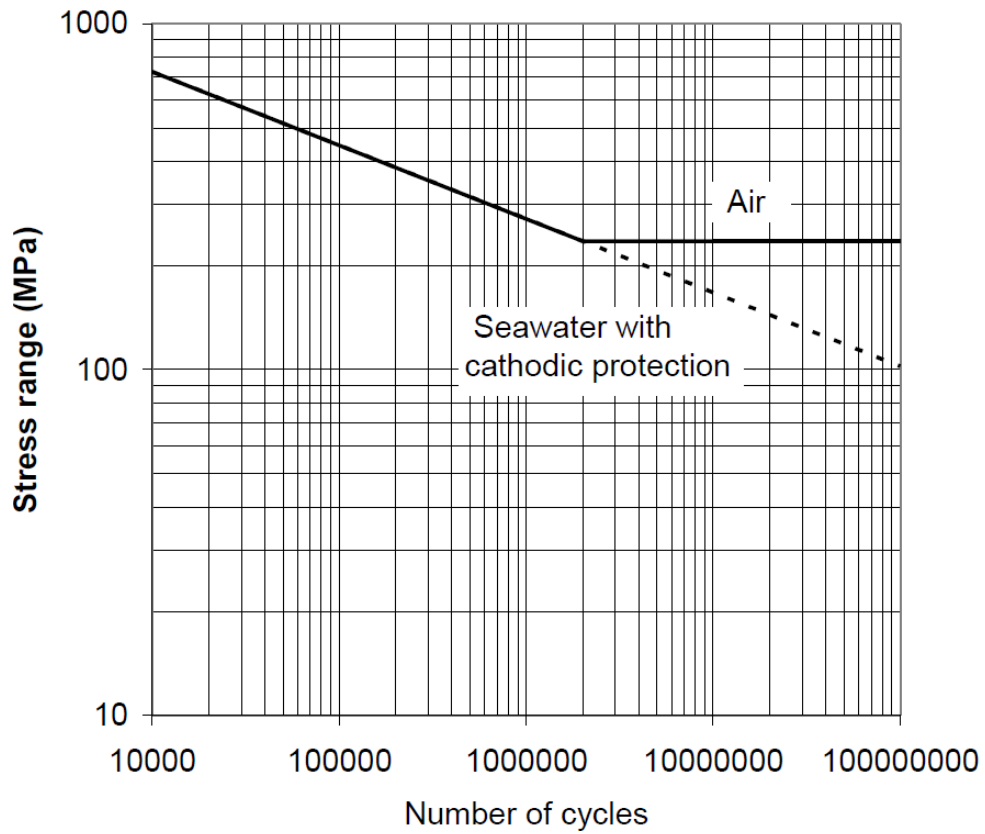
Figure 2-13: S-N curves for high strength steel with high mean tensile stress (DNV GL Group, 2016)

Non-zero value of mean stress can affect stress amplitude. There are multiple models for estimation of the effect of non-zero mean stress on stress amplitude. Correction factors for non-zero mean stress has been presented in Figure 2-14.

The flowchart of the design procedure proposed by DNV for designing subsea free-spanning pipelines is provided in Figure 2-15.
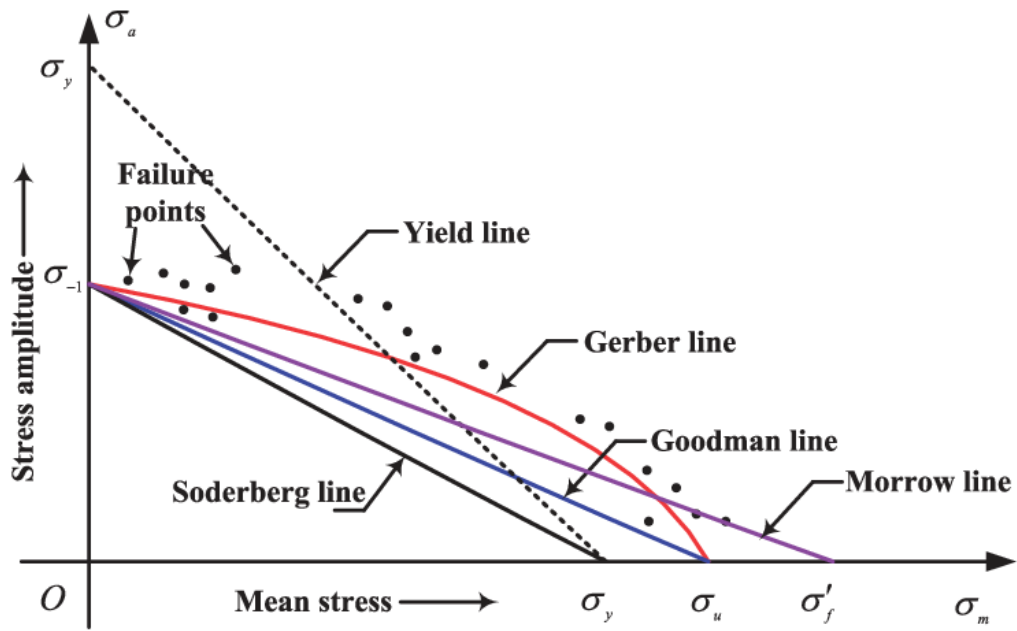
Figure 2-14: Impact of non-zero mean stress on fatigue prediction in metal (Zhu et al, 2017).
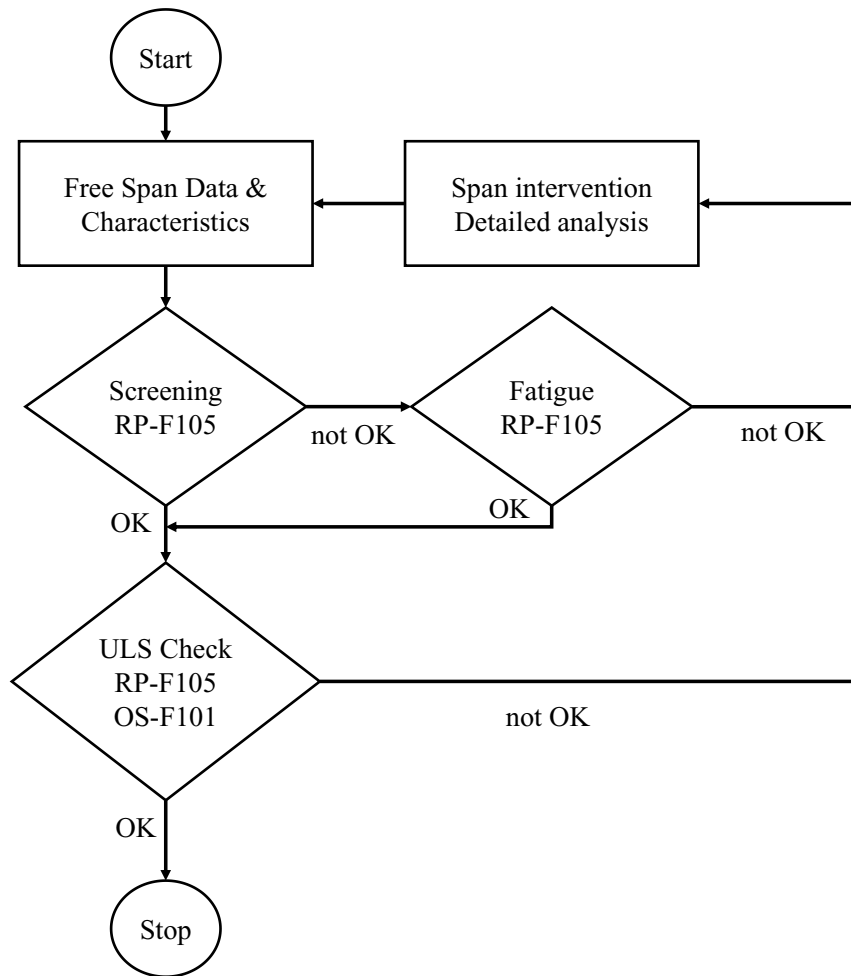
Figure 2-15: flow chart of design procedure for subsea free-spanning pipelines (DET

NORSKE VERITAS, 2021).

2.18 Flow regimes

Based on the proposed methodology by DNV RP-F105, flow regimes are categorized based

on dominance of wave or current. There are three classes for flow regimes based on the

parameter β. Parameter β can be obtained through equation (2-42)

$$\beta = \frac{U_c}{U_c + U_w} \qquad (2\text{-}42)$$

Where U_c velocity of current flow at pipeline level and U_w is velocity of wave at pipelines level. Classification of flow regimes are provided in the following table:

Table 2-4: classification of flow regimes.

Range	Flow regime
$\beta < 0.5$	Wave dominant – waves superimpose currents
$0.5 < \beta < 0.8$	Wave dominant – Currents super impose waves
$0.8 < \beta$	Currents dominant

1.1 VIV stress calculation

Stress values extracted from numerical simulation are not directly applicable in VIV stress and VIV fatigue life calculations. The procedure to convert initial stresses to VIV stresses is described in DNV RP-F105.

2.19 Cross-flow VIV stress

Generally, cross-flow induced VIV stress is calculated regarding effects of both currents and waves. Since the main objective of this research is to study VIV damage on pipelines installed in deep waters where waves are mostly dissipated, the VIV stresses are calculated for pure current flows.

Cross-flow VIV stresses can be calculated by formula below:

$$S_{CF} = 2A_{CF}\left(\frac{A_Z}{D}\right)R_k\gamma_s \tag{2-43}$$

Where A_{CF} is the stress amplitude in cross-flow direction which can be obtained from numerical model. R_k is the amplitude reduction factor due to damping and γ_s is the safety factor for stress range which can be obtained from Table 2-5.

Reduction factor due to damping in cross-flow direction can be determined based on stability parameter K_s.

$$K_{sd} = \frac{K_s}{\gamma_s} \tag{2-44}$$

$$R_K = \begin{cases} 1 - 0.15K_{sd} & K_{sd} \leq 4 \\ 3.2\, K_{sd}^{-1.5} & K_{sd} > 4 \end{cases} \tag{2-45}$$
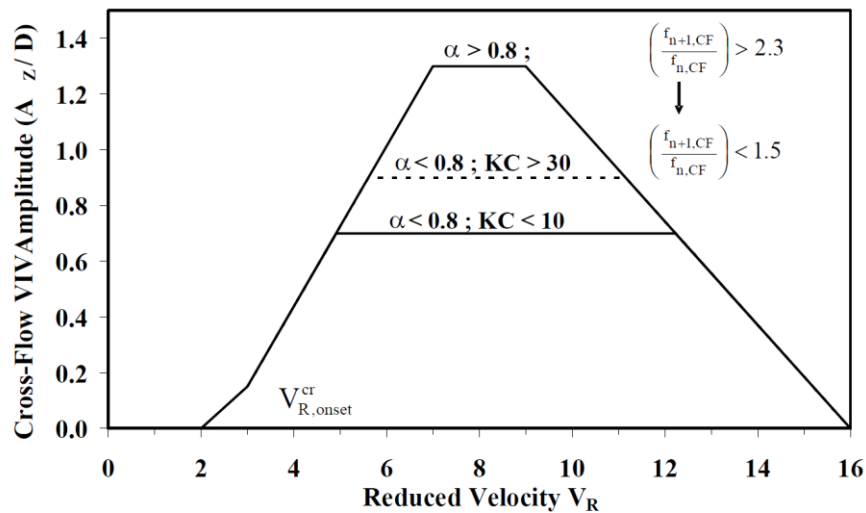
Figure 2-16: Cross-flow response amplitude (DNV RP-F105, 2021).

2.20 In-line VIV stress

In-line VIV stress can be obtained by using equation (2-46).

$$S_{IL} = 2A_{IL}\left(\frac{A_Y}{D}\right)\gamma_s\psi_{\beta,IL} \tag{2-46}$$

Where A_{IL} is in-line stress amplitude, $\frac{A_Y}{D}$ is normalized in-line amplitude, γ_s is safety factor for stress range, and $\psi_{\beta,IL}$ is the correction factor for fluid flow ratio β. Correction factor for flow rate β can be obtained by formula below:

$$\psi_{\beta,IL} = \begin{cases} 0.0 & \beta < 0.5 \\ \dfrac{\beta - 0.5}{0.3} & 0.5 < \beta < 0.8 \\ 1.0 & \beta > 0.8 \end{cases} \tag{2-47}$$

Since in cases of interest of this study the wave effect is neglected, therefore, we have $\psi_{\beta,IL} = 1$.

Table 2-5: General safety factors for fatigue analysis (DNV RP-F105, 2021)

Safety Factor	Safety Class		
	Low	Medium	High
η	1.0	0.5	0.25
γ_k	1.0	1.15	1.30
γ_s	1.3		
$\gamma_{on,IL}$	1.1		
$\gamma_{on,CF}$	1.2		
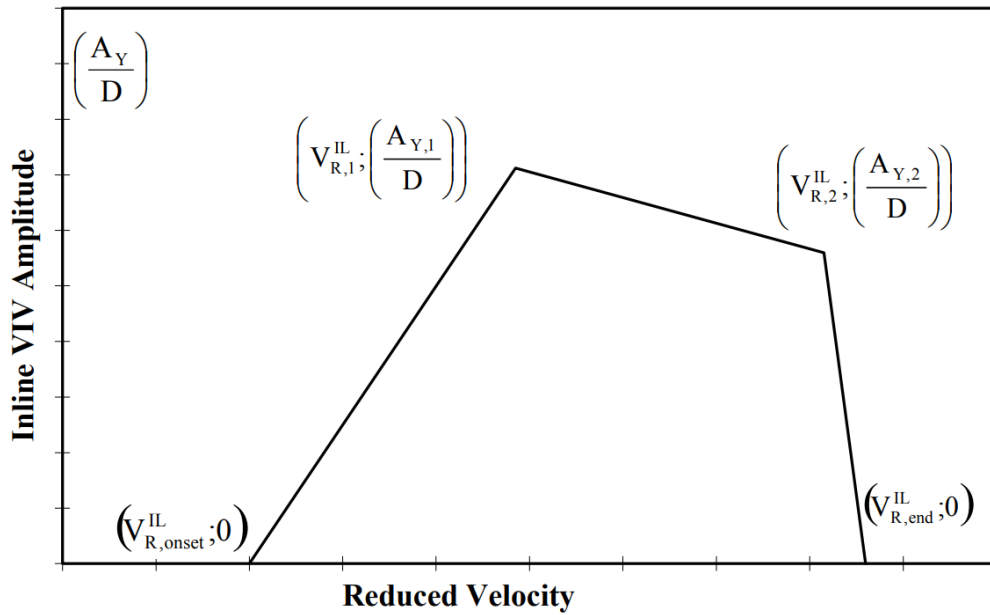
Figure 2-17: In-line model principal response (DNV RP-F105, 2021).

2.21 Cross-flow induced in-line vibrations.

In addition to eigen natural frequencies in in-line direction, the dominant cross-flow mode can also induce vibration in in-line direction. These in-line vibrations are due to motion of figure8. The figure 8 motion refers to the phenomenon that while the cross section of pipeline is following displacement path due to a cross-flow mode, it also has displacements in in-line directions and full pass of cross-sectional displacement is creating a pattern of shape of number 8. This motion is called motion of figure 8. The in-line natural mode shape with closest value of natural frequency to twice of the dominant cross-flow can be influenced by the dominant cross-flow mode.

For candidate in-line mode, the VIV stress of cross-flow induced in-line mode is calculated and then the largest value between original in-line VIV stress of candidate in-line mode and calculated cross-flow induced mode will determine value of in-line VIV stress in the mode. The first cross-flow mode is usually the dominant cross-flow mode with largest VIV stress.

$$S_{Cf-IL} = 0.8\, A_{IL} \left(\frac{A_{z_{\max}}}{D} \right) R_k \gamma_s \tag{2-48}$$

Chapter 3:

Numerical simulation

The key objective of this chapter is to simulate and study the impact of seabed and structural parameters on VIV fatigue performance of free-spanning and multi-spanning pipelines. Fatigue life and VIV stress have been calculated based on methods provided by DNV RP-F105. In this project, a thorough parametric study with multiple case for each variable has been conducted. Regarding the methodology presented in DNV RP-F-105, natural frequencies, mode shapes, and stresses resulting from deflection of in mode shapes are key parameters for VIV stress and VIV fatigue life calculation. In this project a finite element model for pipeline under free-spanning condition has been developed and different cases including seabed condition, single or multi-spanning, length of shoulder between neighboring spans, pipe properties including diameter, wall thickness, current flow speed, and mechanical properties of materials, and soil stiffness has been studied. Finite element modeling and analysis has been conducted by ABAQUS® software as an input keyword script. A comprehensive Python® script developed to conduct parametric study. The Python scripts has the ability to control Abaqus for developing new case studies, read Abaqus ODB files, extract necessary data from ODB files, and enhance simulation performance by cleaning output data, managing computational resource for optimum speed and accuracy.

3.1 Finite element model

The finite element model has been developed based on instructions of DNV RP-F105. In this model length of the free-spanning sections is within the range $60 < \frac{L}{D} < 140$, where based on DNV RP-F105, pipe behavior can be interpreted using beam elements. In this regard, the pipeline has been modeled as a three-dimensional beam element with respect to properties of a pipeline where the element type PIPE31is selected. The element type PIPE31 features a linear beam element with 2 nodes in space (three dimensional). Length of each element is equal to pipe diameter. Figure 3-1 present convention order of an element in ABAQUS.
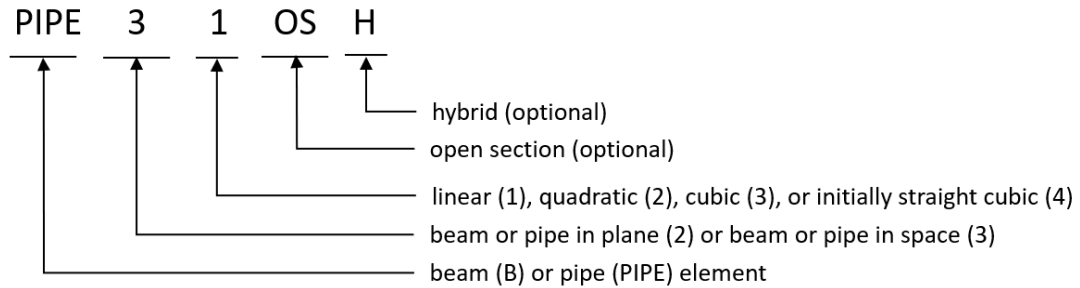
Figure 3-1: Abaqus Naming Convention.

The seabed has been modeled as an analytical rigid surface and soil-pipe interaction is modeled by non-linear springs in three dimensions. Lateral stiffness of soil is modeled by pair of springs which are perpendicular to central line of pipeline in downstream and upstream of in-line currents flow. Values of stiffness for spring has been extracted from instructions of DNV RP-F105 and stiffness of axial springs are equal to lateral springs. A It is assumed that current flows in Y direction and pipeline is extended along X direction, therefore; mode shapes deflecting in XY plane are the in-line modes and mode shapes

deflecting in XZ plane are cross-flow modes. In this this study for each case first eight natural frequencies have been extracted. It is determined that in majority of cases half of first eight natural frequencies are in in-line direction and the other half are in cross-flow direction.

Seabed is modeled as analytical rigid surface and fixed by applying boundary conditions (ENCASTRE) to prevent its displacement and rotation. Pipeline is modelled as a beam string type PIPE31, and one end of pipe string has been restrained (ENCASTRE) by applying boundary conditions. The other end of pipe string has no boundary condition. General morphology of assumed seabed is shown in Figure 3-2.
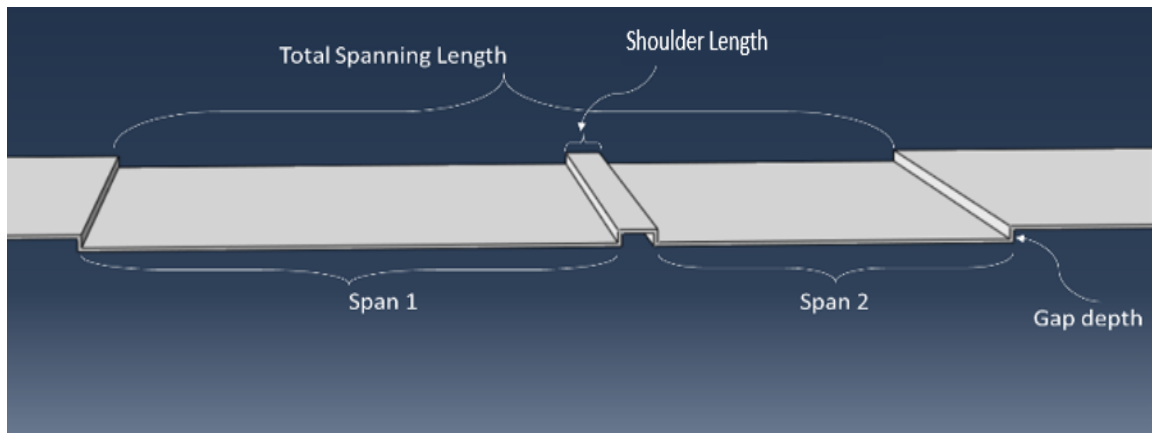
Figure 3-2: Seabed Morphology in finite element model.

3.2   Python® script

In order to have a comprehensive set of data, large number of numerical simulations have to be conducted which needs tremendous amount of time to complete the simulations. To overcome this issue, an external python script has been developed and employed which has the ability to create input files for each study case, access ABAQUS® and feed the input file to it and run the simulation, and simultaneously performs postprocessing on output ODB files to extract valuable numerical information.

Regarding large number of case studies, total required storage for all of the study cases exceeds 20 TB which is not available in most of commercial workstation computers. In order to overcome this limitation, the algorithm of the script is designed to access output models, extract all valuable information, save the extracted information in Excel® spreadsheets and then delete the files which can be considered redundant due as the valuable information have been preserved in excel format.
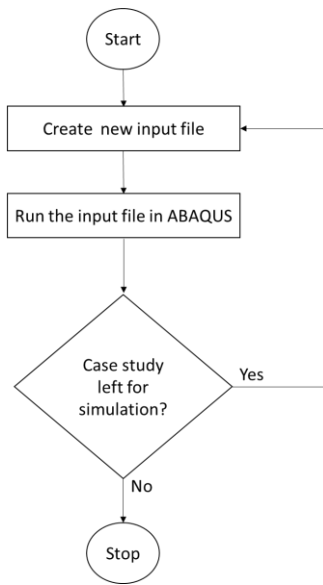
Figure 3-3: Flowchart of the case study simulation script.
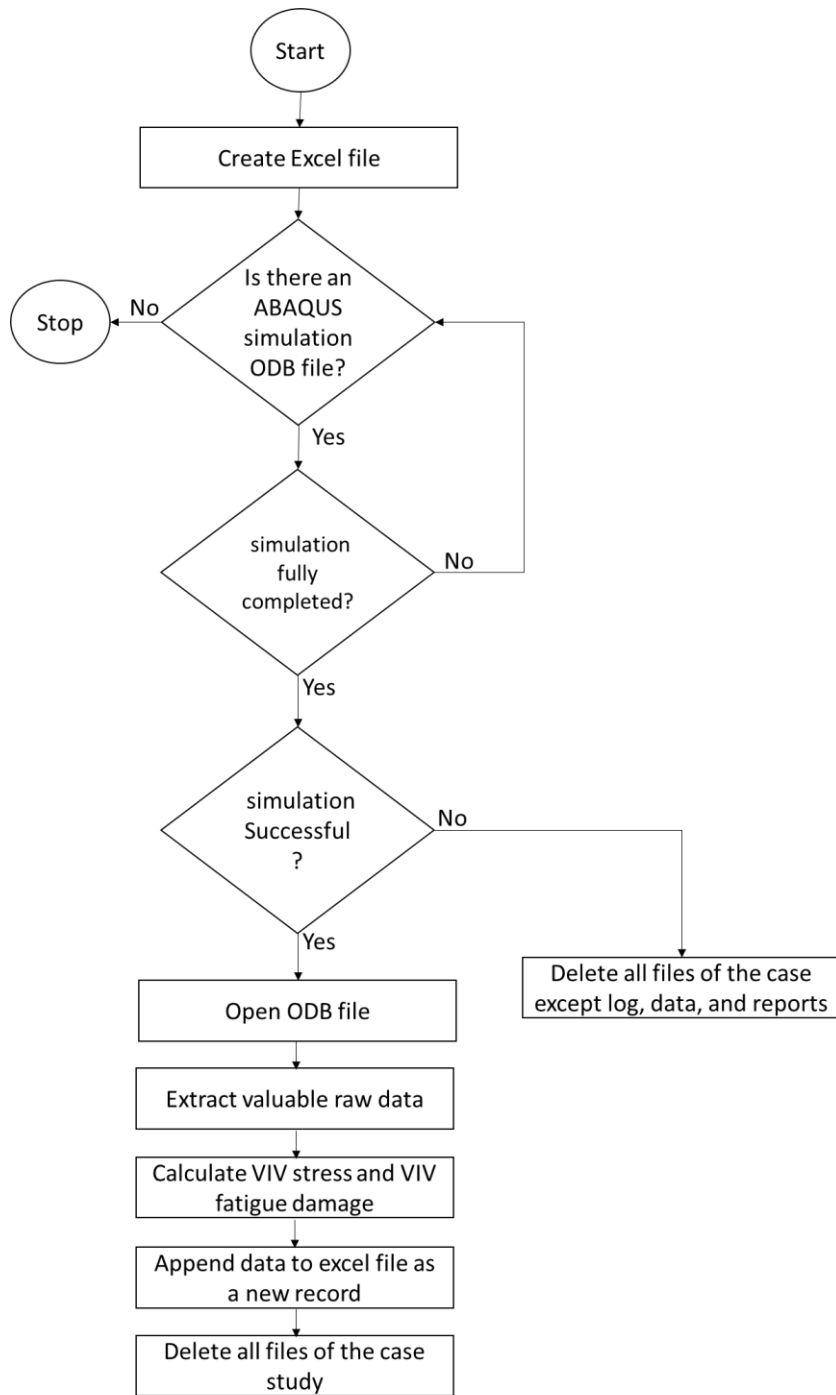
Figure 3-4: Flowchart of postprocessing script.

3.3　Case studies

This section presents detailed information about the simulated case studies. Some characteristics of model configuration remain intact in all the study cases. Common characteristics are outlined. Variation of parameters through study cases are presented in Table 3-2 and Table 3-3 representing variable properties in single-span and multi-span cases respectively. In all the cases studied in research, free-spanning start from the point of 100 m distance from start and the free-spanning will continue as per case configuration. Pipes are selected from commercially available products from ASME/ANSI B36.10/19 - Carbon, Alloy and Stainless-Steel Pipes.

Table 3-1: General characteristics of model.

Parameter	Symbol	Value
Total model Length	—	$250 m$
Pipe density	ρ_{steel}	$7800 \dfrac{kg}{m^3}$
Internal fluid density	ρ_{in}	$900 \dfrac{kg}{m^3}$
Installation depth	h	$600\ m$
Concrete coating thickness	$t_{concrete}$	$50\ mm$
Anti-corrosion coating thickness	t_{ac}	$8\ mm$
Soil type	—	Medium Sand
Current speed	u	$0.1 \dfrac{m}{s} < u < 4 \dfrac{m}{s}$
Pipe schedule		XS

Table 3-2: Variable parameters of single-span study cases.

Parameter	Range	
	MIN	MAX
Aspect ratio	60	210
Gap ratio	0.5	4
Pipe size	5	24

Table 3-3: Variable parameters of multi-span study cases.

Parameter	Range	
	MIN	MAX
Aspect ratio	60	210
Gap ratio	0.5	3
Pipe size	5	24
Spans aspect ratio	1	5
Shoulder aspect ratio	1	7

Table 3-4: Generally common characteristics of model.

Parameter	Symbol	Value
Total model Length	$-$	*250 m*
Pipe density	ρ_{steel}	$7800\dfrac{kg}{m^3}$
Internal fluid density	ρ_{in}	$900\dfrac{kg}{m^3}$
Installation depth	h	$600\ m$
Concrete coating thickness	$t_{concrete}$	$50\ mm$
Anti-corrosion coating thickness	t_{ac}	$8\ mm$
Pipe schedule		XS

Table 3-5: Reference pipe sizes.

Pipe size	Wall thickness (mm)	Outer diameter (mm)
5	9.53	141.3
6	10.97	168.3
8	12.7	219.1
10	12.7	273.1
12	12.7	323.9
14	12.7	355.6
16	12.7	406.4
18	12.7	457.2
20	12.7	508
22	12.7	559
24	12.7	609

3.4   Model Verification

Accuracy of modal analysis model has been cross-examined based on results by Pereira A, et al. Their research focuses on free-span assessment by using finite element analysis. The

article provides a comparison between FATFREE and their in-house program SPAN2B. Some of the main geometrical properties and pipe characteristics of the referenced study are presented in Table 3-6. Since there are lots of other parameters affecting natural frequencies of case studies and those parameters hasn't been revealed in the reference work, we are expecting a similar trend of changes between results from developed FE model and results from FATFREE. Similar to Pereira A, et al., results from modal analysis of developed finite element model has been compared with results from DNV FATFREE. Despite having an offset which in inevitable due to presence of unknown parameters such as residual axial tension and characteristics of coating layers, response of the finite element mode has good compliance with model of FATFREE. Results of conducted comparison are presented in Figure 3-5 and Figure 3-6.

Table 3-6: Model configuration of FATFREE case studies.

Parameter	Symbol	Value
Pipe diameter	D_o	$12.75\ in$
Pipe wall thickness	t	$0.875\ in$
Internal fluid density	ρ_{in}	$900\ \dfrac{kg}{m^3}$
Installation depth	h	$600\ m$
Concrete coating thickness	$t_{concrete}$	$50\ mm$
Anti-corrosion coating thickness	t_{ac}	$8\ mm$
Soil type	$-$	$Medium\ Sand$
Current speed	u	$0.1\dfrac{m}{s} < u < 4\dfrac{m}{s}$
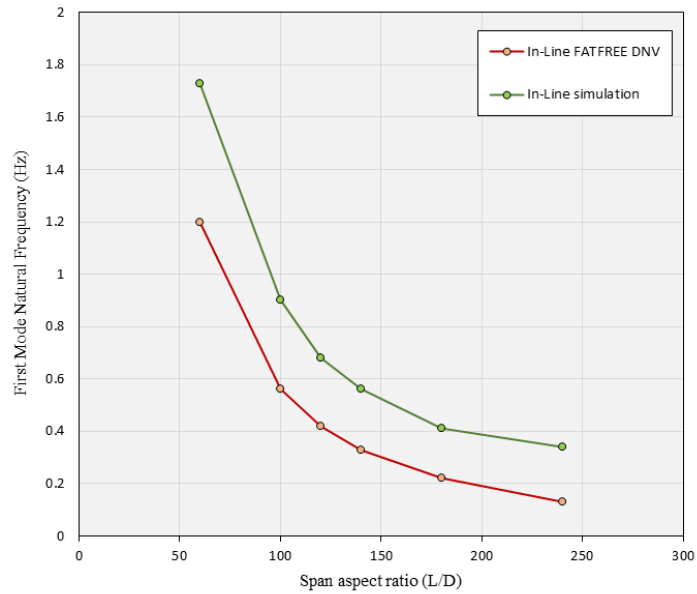
Figure 3-5: Comparison of in-line natural frequencies between DNV FATFREE and conducted FEA.
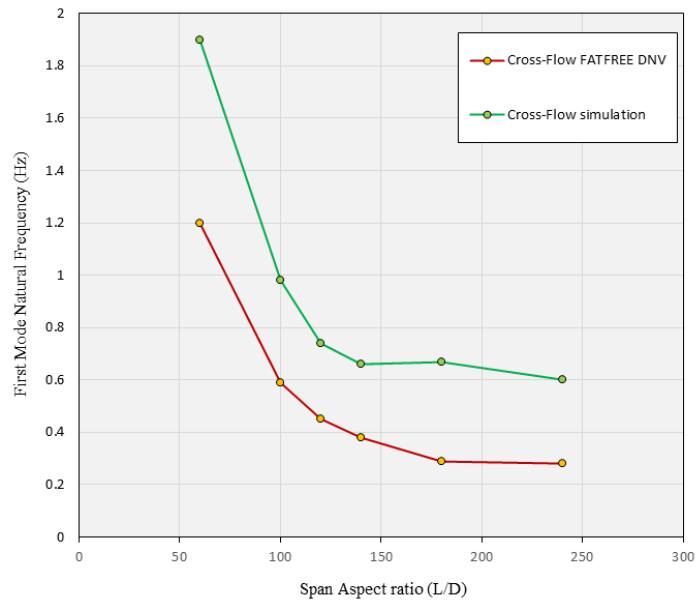
Figure 3-6: Comparison of cross-flow natural frequencies between DNV FATFREE and conducted FEA.

3.5 Single span

Result of simulation and post processing of single-span cases are presented. Figure 3-7 shows the initial condition of a single-span configuration. There are initial deflection and initial stress profile along pipeline which are due to pipeline weight acting as uniform distributed gravity force. initial gravitational force forms a sagging deflection toward span depth. Mode-shape of first natural mode of selected single-span sample is presented in Figure 3-8 and Figure 3-10 present the first cross-flow mode-shape of sample free-span sample. Details of selected sample of single-span cases are listed in Table 3-7. In all of the cases seabed is extended along XY plane; therefore, deflections related to in-line mode-shapes are expected to be in XY plane and likewise, cross-flow mode shapes will be in XZ plane. Second mode-shapes in in-line and cross-flow directions are presented in Figure 3-9 and Figure 3-11 respectively. Since size of pipe diameter is relatively smaller than span length, pipeline diameter is shown by up-scale render. Similarly, due to relatively smaller magnitude of lateral displacements during natural mode-shapes, deflections have been magnified by scale of 50x to make deflections intuitive.

Table 3-7: Configuration of sample single-span model.

Parameter	Value
Span aspect ratio	60
Pipe outer diameter (steel)	5.563 in
Pipe wall thickness	0.375 in
First in-line frequency	4.4628 Hz
Second in-line frequency	6.2583 Hz
First cross-flow frequency	3.9068 Hz
Second cross-flow frequency	9.1453 Hz
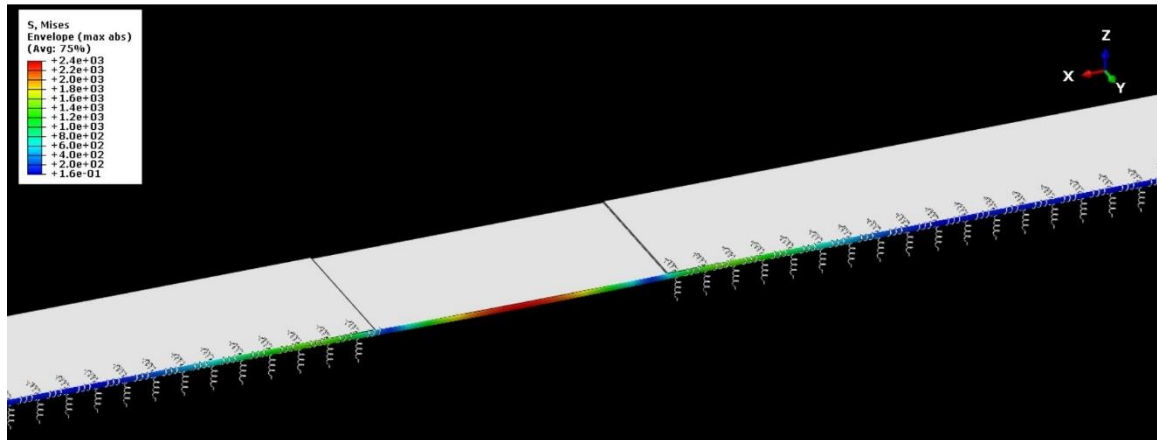
Figure 3-7: Initial condition of single span configuration.
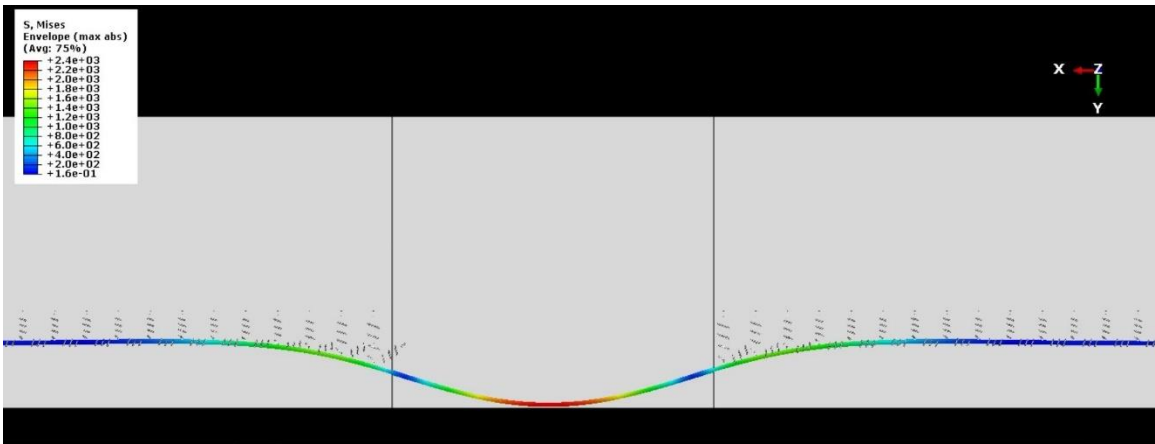
Figure 3-8: First in-line mode-shape of single span configuration.
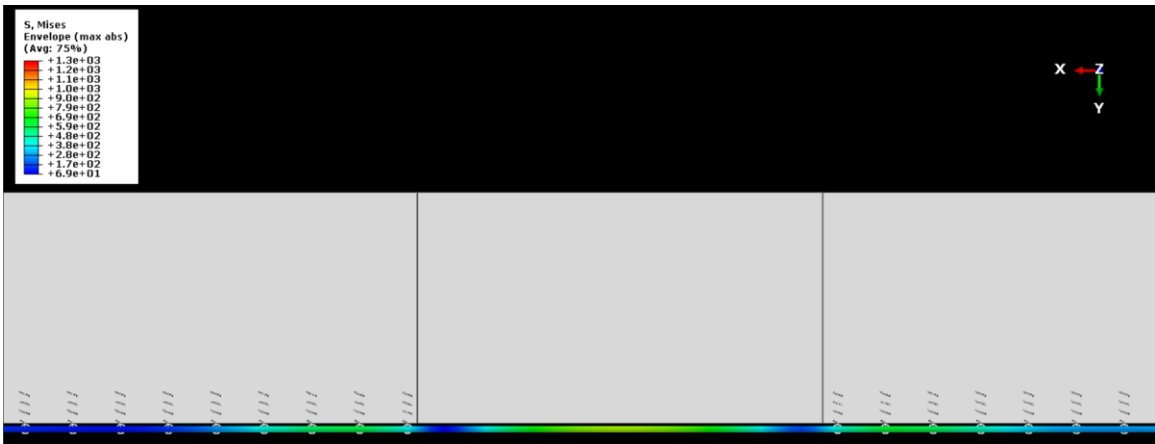
Figure 3-9: Second in-line mode-shape of single-span configuration.
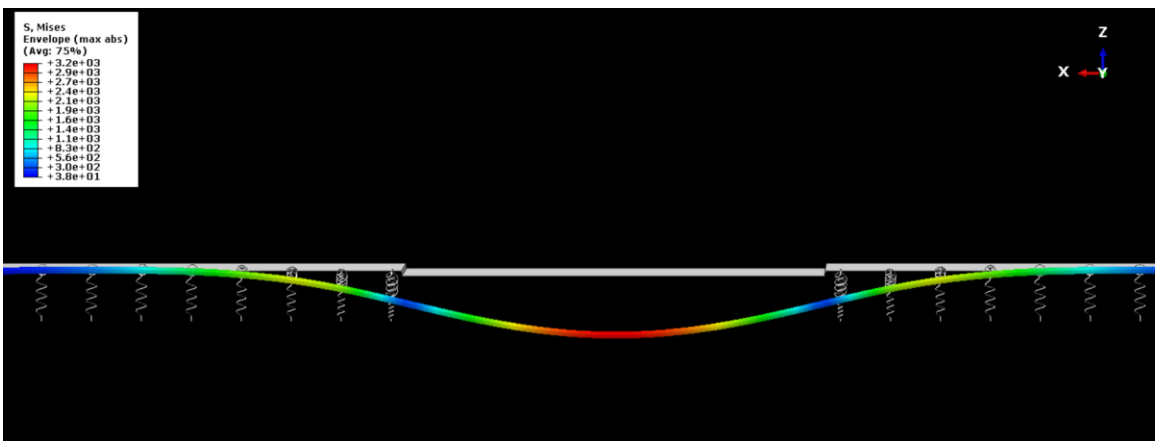
Figure 3-10: First cross-flow mode-shape single span configuration.
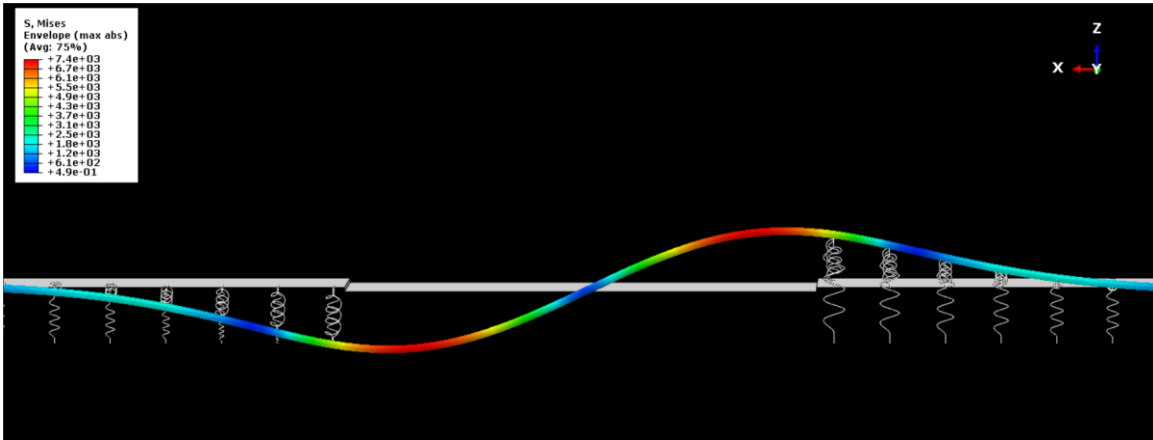
Figure 3-11: Second cross-flow mode-shape of single-span configuration.

3.6 Multi-span

Similar to single-span, a case from multi-span cases has been selected and it's first mode-shapes in in-line and cross-flow directions has been presented. Initial condition of this case is presented in Figure 3-12. Mode-shapes of first and second in-line natural frequencies are presented in Figure 3-13 and Figure 3-14 respectively. First and second cross-flow mode shapes of this are also presented in Figure 3-15 and Figure 3-16. For better visual understanding deflections in both in-line and cross-flow directions have been magnified by factor of 100x. Characteristics of selected multi-span case are outlined in Table 3-8.

Table 3-8: Configuration of sample multi-span model.

Parameter	Value
Span aspect ratio of total spanning length	120
Pipe outer diameter (steel)	8.625 in
Pipe wall thickness	0.500 in
Shoulder aspect ratio	7
Relative aspect ratio	2.33
First in-line frequency	1.1579 Hz
Second in-line frequency	2.3324 Hz
First cross-flow frequency	2.5858 Hz
Second cross-flow frequency	4.8363 Hz
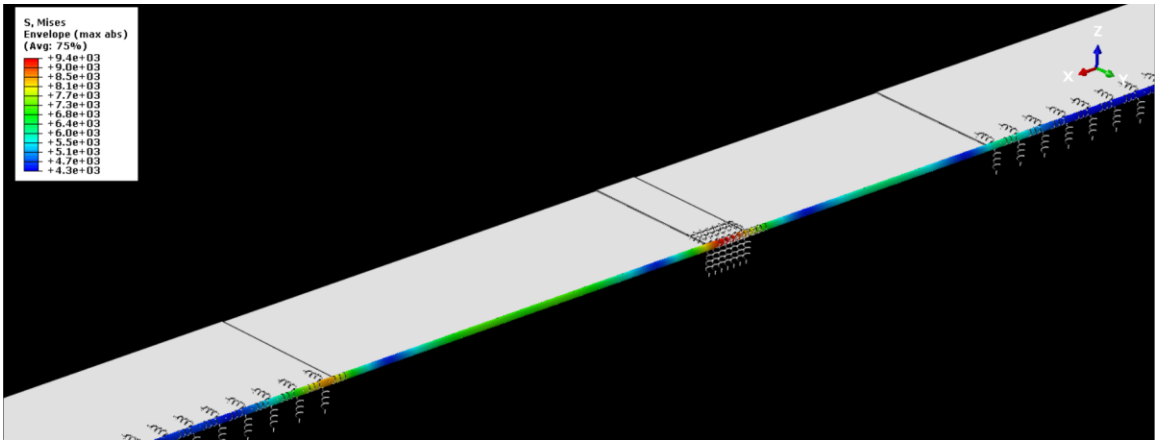
Figure 3-12:Initial condition of multi-span configuration.
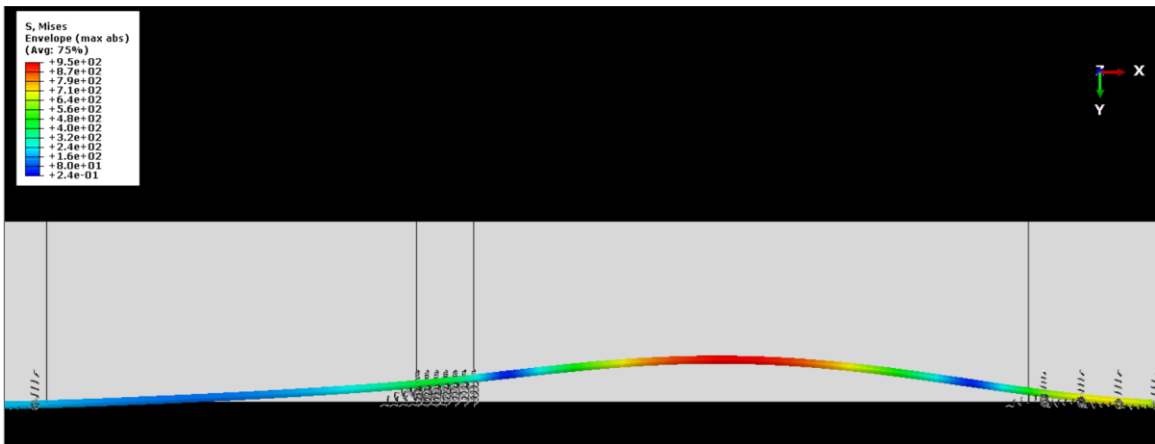
Figure 3-13: First in-line mode-shape of multi-span configuration.
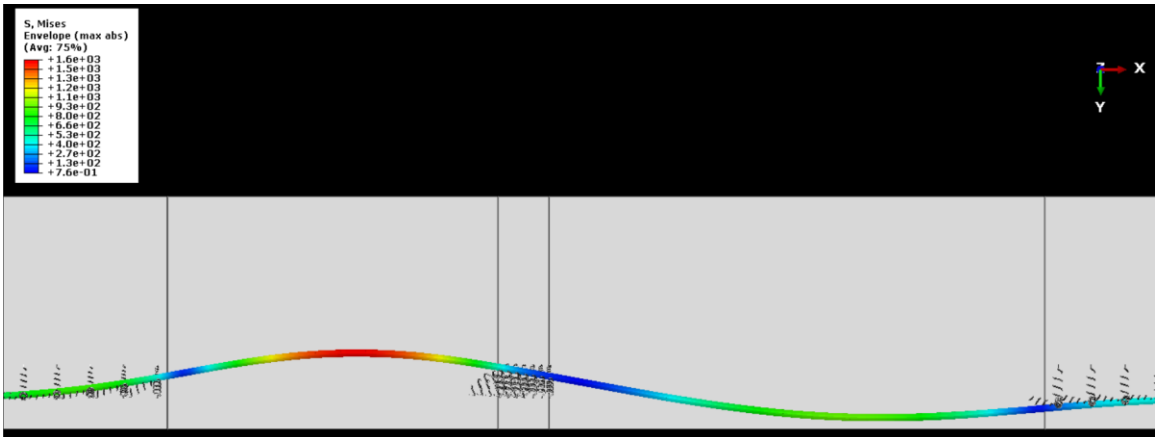
Figure 3-14: Second in-line mode-shape of multi-span configuration.
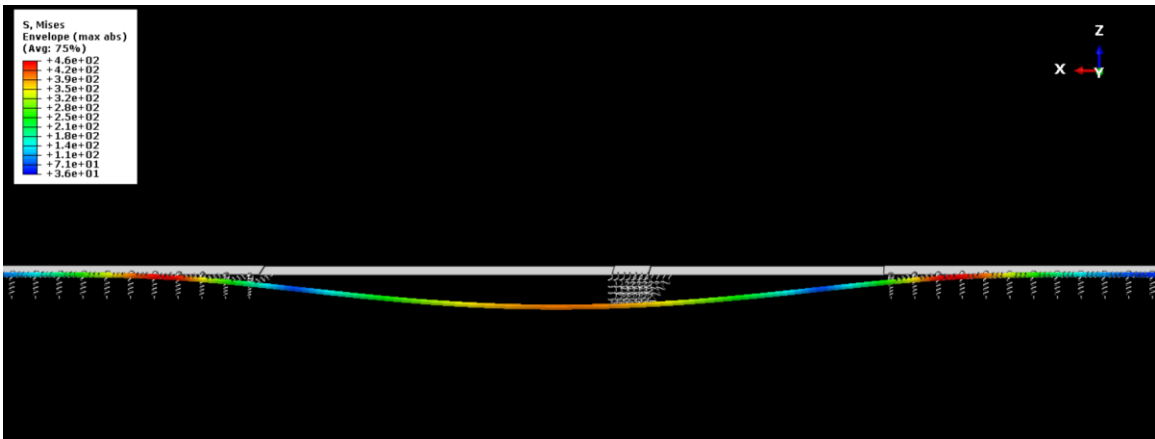
Figure 3-15:First cross-flow mode-shape of multi-span configuration.
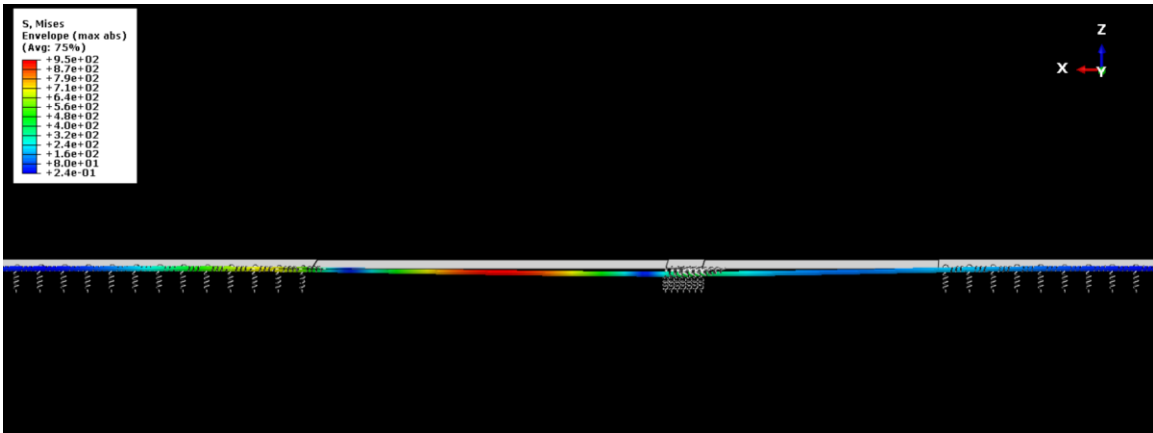
Figure 3-16: Second cross-flow mode-shape of multi-span configuration.

3.7   Selected stress analysis results

3.7.1   Pipe size 5 in single-span configuration

For pipe size 5, in-line mode and cross-flow mode stresses are presented in Figure 3-17 and Figure 3-18. For in-line mode, level of the stress is very low, and it is not expected to have significant impact on fatigue life. Cross-flow stresses found to be significantly higher. For shorter spans there first, end, and middle of the span are experiencing intensified level of stress while for longer spans, level of the stress in central region of the span length is weaker.
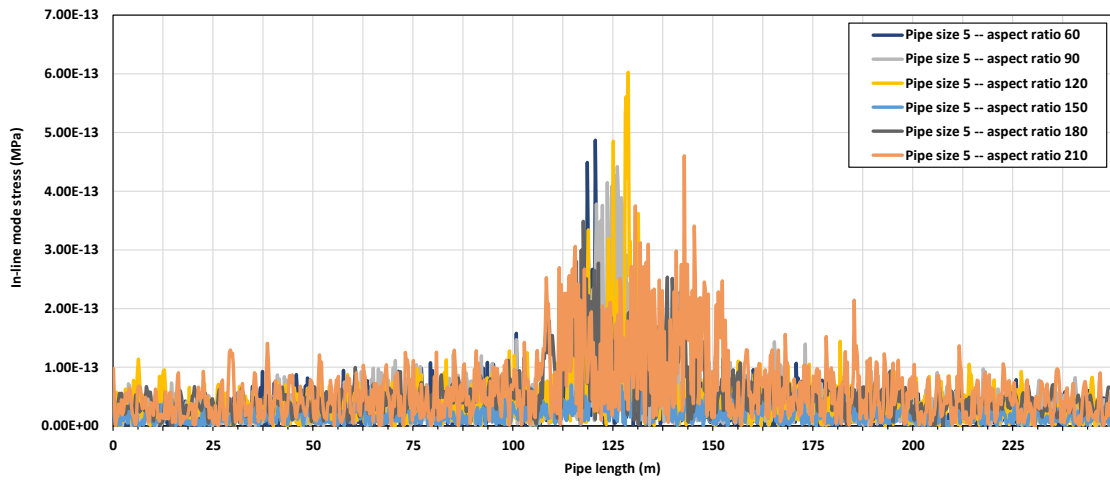
Figure 3-17: In-line mode stress of pipeline of pipe size 5 in single-span configuration.
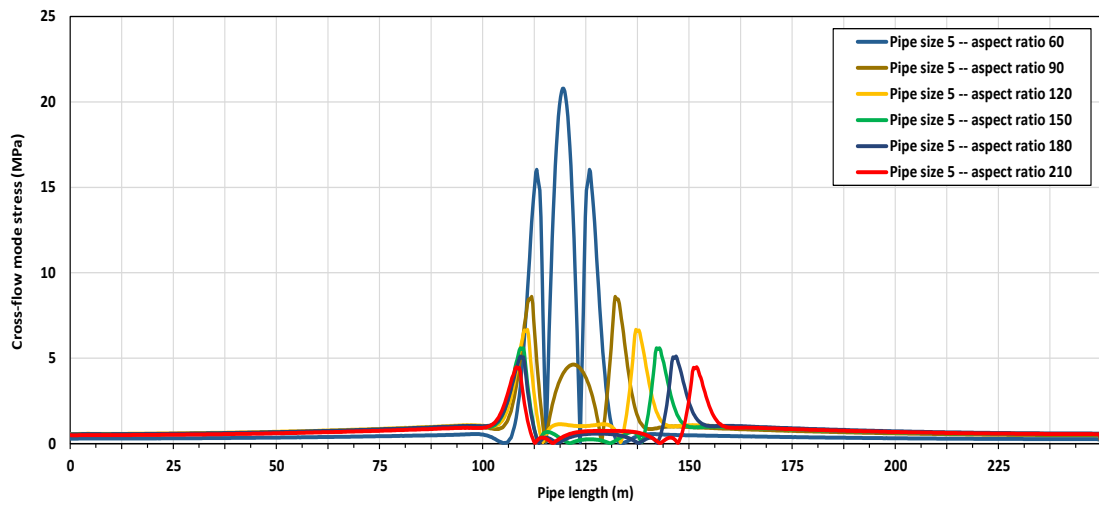
Figure 3-18: Cross-flow mode stress of pipeline of pipe size 5 in single-span configuration.

3.7.2 Pipe size 10 in single-span configuration

Stress profiles for natural frequencies of pipeline size 10 in in-line and cross-flow directions are presented in Figure 3-19 and Figure 3-20 respectively. Level of stress for in-

line mode shape fount be negligible and for the cross-flow direction by increase in length of the span, level of stress is declined.
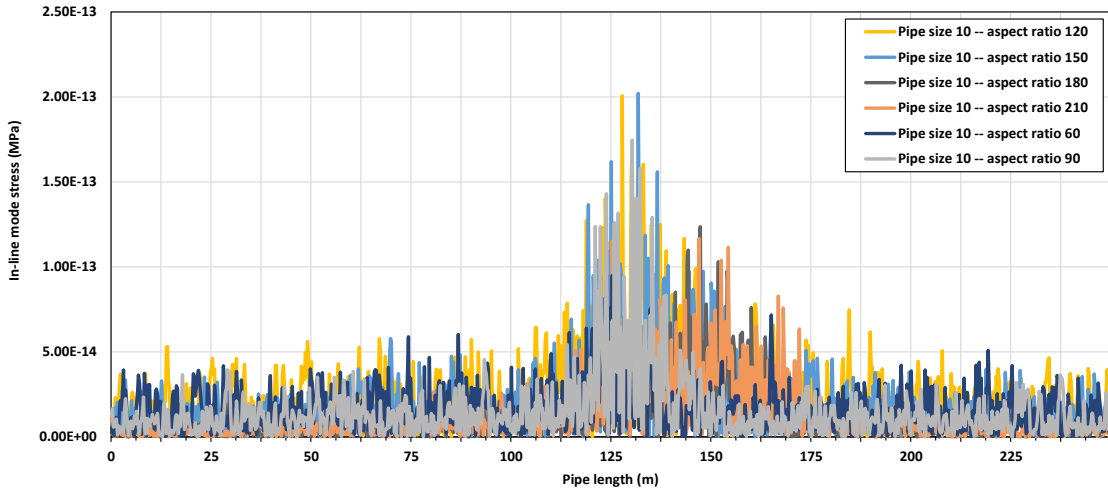
Figure 3-19: In-line mode stress of pipeline of pipe size 10 in single-span configuration.
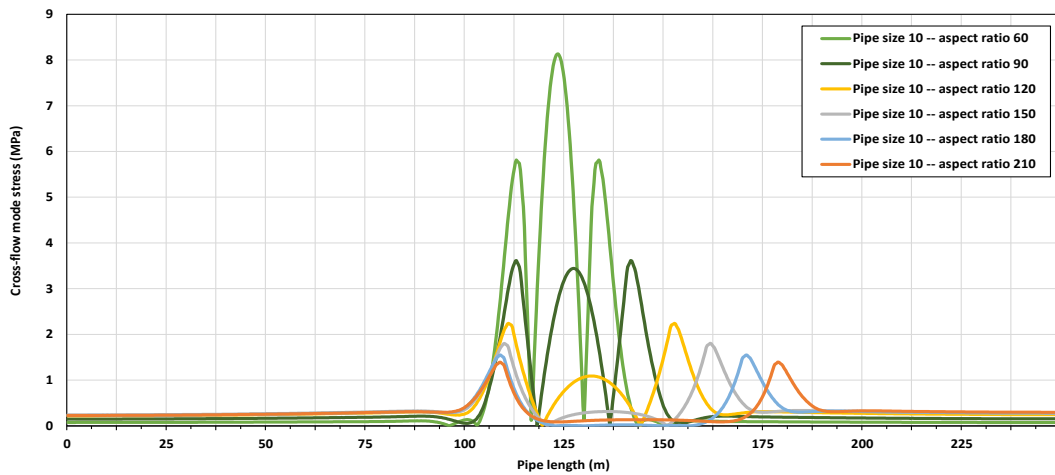
Figure 3-20: Cross-flow mode stress of pipeline of pipe size 10 in single-span configuration.

3.7.3 Pipe size 16 in single span configuration

Stresses due to in-line and cross-flow mode shapes are presented. Stresses profiles for in-line and cross-flow modes outlined in Figure 3-21 and Figure 3-22 respectively. For in-line modes, the increase in stress due to deflections in in-line natural mode found to be negligible. Level of the stress by increase in length of the span is decreasing.
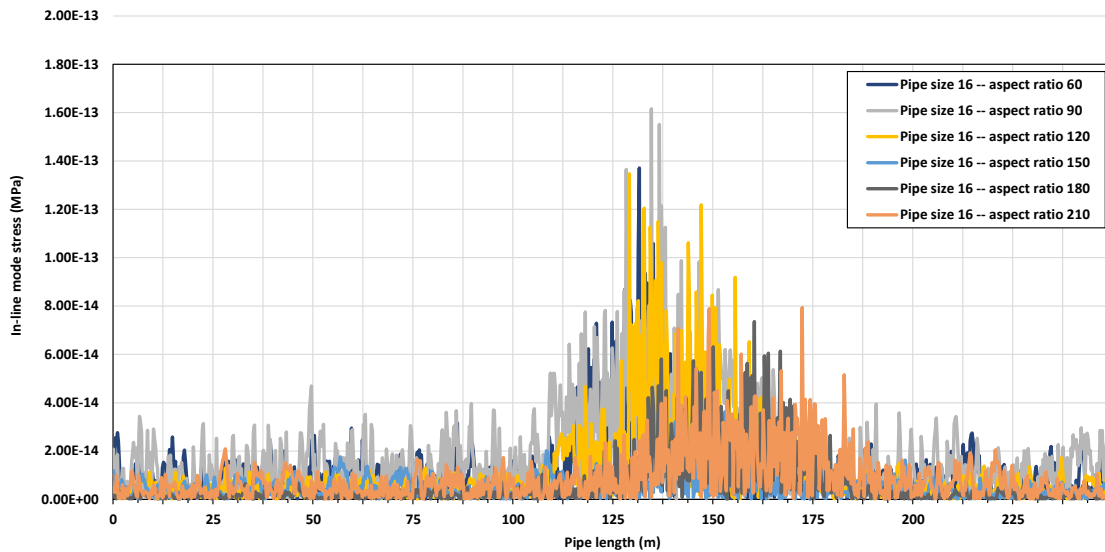
Figure 3-21: Cross-flow mode stress of pipeline of pipe size 16 in single-span configuration.
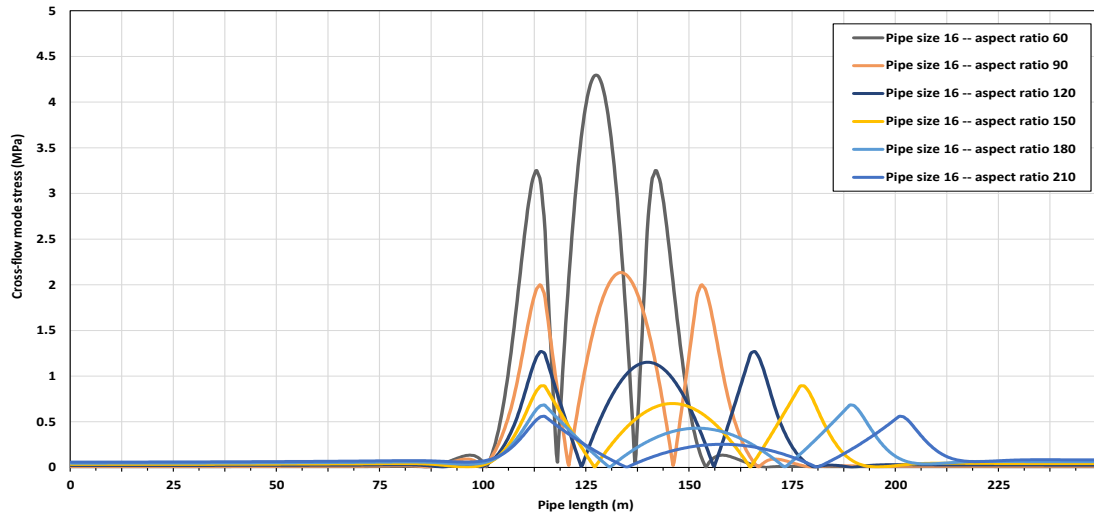
Figure 3-22: Cross-flow mode stress of pipeline of pipe size 16 in single-span configuration.

3.8 Rapid failure cases

During analysis it found that in some cases, pipeline structure undergoes severe loads leading the structure into rapid failure. Cases which undergo the rapid failure can be categorized in three groups including failed due to structure's self-weight and increased tension in shoulder edges, cases with shallow depth of span where dynamically resonated pipeline reach into a contact with seabed causing severe damage to pipeline structure, and cases where length of the shoulder is not long enough to avoid extensive concentrated load on pipeline over shoulder length and specifically over edges of shoulder. Table 3-9 demonstrates cases which will potentially experience rapid failure.

Table 3-9: Rapid failure of free-spanning pipelines.

Size	In single-span	In multi-span	reason	
			Single span	Multi-span
5	No	Yes	-	Shoulder
6	No	Yes	-	Shoulder
8	No	yes	-	Shoulder
10	No	No	-	-
12	No	No	-	-
14	No	No	-	-
16	No	Yes	-	Geometrical
18	Yes	Yes	Weight	Weight
20	Yes	Yes	Weight	Weight
22	Yes	Yes	Weight	Weight
24	Yes	Yes	Weight	Weight

Chapter 4:

Application of Machine Learning algorithms for VIV analysis

Within the past decade artificial intelligence (AI) has become one the dominant tools in almost every industrial and scientific field. Machine learning (ML) methods as a subfield of artificial intelligence have the most contribution in evolution of decision making based on AI. Application of ML methods are best when working on massive raw data when there is no analytical solution to detect the relation between inputs and out puts. Decision tree is a supervised learning method for building ML models. This method is the root mechanism of some of the most effective machine learning methods. ML models based on decision tree are applicable on both problems of classification and regression.

Precise estimation of VIV fatigue life requires the knowledge of exact current flow profiles exerting on pipeline structure throughout its course of operational life. Regarding the inevitable uncertainty in prediction of currents, the VIV stress applied due to list of selected current speeds have been selected as target to be predicted by trained machine learning models. Since the parameter stress has continues nature, ML models have been trained for regression purposes.

In this research performance of four different methods of training a ML model including Decision Tree Regression (DTR), Random Forest Regression (RFR), Extra Tree Regression (ETR), and Support Vector Regression (SVR) have been studied where ETR and RFR methods have roots in DTR model. In this research, 20% of datasets are randomly selected for test purposes and 80% of data are used for training ML models. The dataset

for single-span and multi-span configurations includes 634 and 14561 cases respectively where rapid failure cases have been excluded from datasets.

4.1 Terminology

In this section common terms used in machine learning are described.

4.1.1 Root node

Root node is the head node of tree which constitutes all the data samples. This node does not have any parents, instead, it is the starting point where divisions are started.

4.1.2 Parent and child

A node, which it's content is divided into two or more sub-nodes is parent node to the nodes sub-divided from it and sub-divided nodes are children of it.

4.1.3 Decision node

A node which has both parent and child roles is a decision node. A decision node is child to the upper, parent node and it has its own sub-divided children.

4.1.4 Splitting

The process of dividing contents of a node between two or more sub-nodes(children) is called splitting. Decision about a decision to occur depends on variety of variables based on employed algorithm.

4.1.5 Leaf or terminal node

A node which its content is not considered to be divided into sub-nodes is called a leaf or terminal node.

4.1.6 Pruning

Pruning is the process of eliminating unnecessary data from the tree which helps best to overcome overfitted models. This process is the opposite of splitting and sub-divided branches are removed.

4.1.7 Underfitting

Underfitting is a scenario where the trained model fails to learn the relationship between data and its attributes. An underfitted model is unable to predict the outcome correctly or with favorable precision.

4.1.8 Overfitting

Overfitting is a scenario where the model is trained extensively focusing on training data. An overfitted model will have outstanding precision predicting trained data but fails to offer acceptable performance on test data. In an overfitted model, the model learns the noises in addition to actual relationship in data and attributes.

4.1.9 Entropy

Entropy is the level of inhomogeneity in data. When a batch of data is nonhomogeneous, it means that there is a diversity in the data and therefore, the data can be categorized into

smaller divisions with higher homogeneity within the data in each division. Entropy in data can be calculated by formula below:

$$Entropy = H = \sum_{i=1}^{C} -p_i \log_2 p_i \qquad (4\text{-}1)$$

Where H is the entropy and its value ranges between 0 and 1 and p_i is the probability of an attribute in data. Splitting a node with higher entropy (close to 1) will result in higher quality in information gain due to split and lower entropy means that the data inside the node share more common features and splitting them is less likely to deliver extra information. Leaf nodes are nodes where entropy of data within data inside the node is zero. In other words, there are enough similarities between data in the leaf that there is no need to split data into sub-nodes.

4.1.10 Information gain

Information gain is a parameter to measure how well a split in a node affected model accuracy. in mathematical view, information gain is the difference between entropy of an attribute in dataset before and after splitting the node. The main goal is to reach lowest entropy and a splitting process is considered effective when entropy of attribute in children is lower than the entropy in parent node. information gain can be calculated by formula below.

$$Information\ gain = Entropy_{parent} - \sum_{}^{k} \left(\frac{n_i}{n_T}\right) Entropy_{child_i} \qquad (4\text{-}2)$$

Where $Entropy_{parent}$ is the entropy of attribute in the node before splitting process and $Entropy_{child_i}$ is the entropy in i^{th} sub-node resulted from splitting the parent node and k is number of division, n_i is number of data points in i^{th} node, and n_T is total number of data points in parent node.

In order to splitting to be successful, information gain must be a positive number. If the information gain is zero, the splitting had no effect on accuracy of model. This definition tried to be described in Figure 4-1.

a) Low information gain splitting.   b) High information gain splitting.
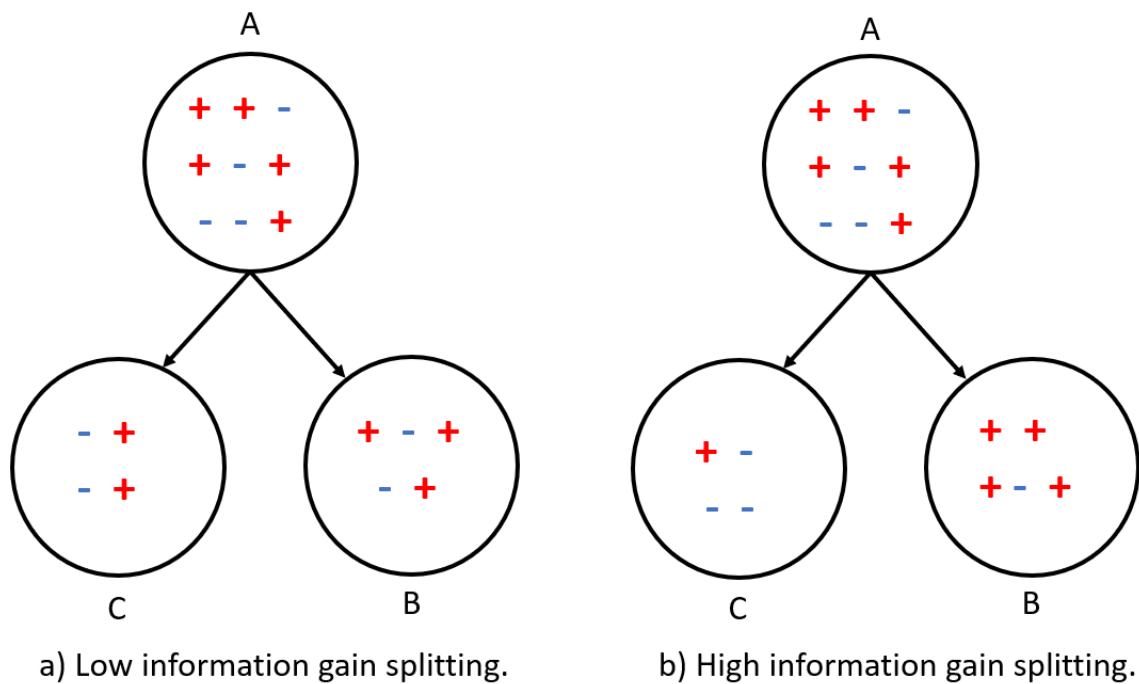
Figure 4-1: Information gain in splitting.

In this figure, parent data node A is divided into two sub-nodes B and C by two different splitting results. The entropy for node A can be calculated by formula below:

$$Entropy\ A = -p_{A-} \log_2 p_{A-} + -p_{A+} \log_2 p_{A+}$$

$$= -\left(\frac{4}{9}\right) \log_2 \left(\frac{4}{9}\right) - \left(\frac{5}{9}\right) \log_2 \left(\frac{5}{9}\right) = 0.99$$

Where P_{A+} is probability of + in node A and P_{A-} is the probability of – in node A. Similarly,

P_{B+}, P_{B-}, P_{C+}, and P_{C-} can be defined as probabilities of + and – in nodes B and C.

Entropies in nodes of B and C in each case can be calculated below.

$$Entropy\ B = -p_{B-} \log_2 p_{B-} \pm p_{B+} \log_2 p_{B+} \qquad (4\text{-}4)$$

$$Entropy\ C = -p_{C-} \log_2 p_{C-} \pm p_{C+} \log_2 p_{C+} \qquad (4\text{-}5)$$

case a:

$$-\left(\frac{2}{4}\right) \log_2 \left(\frac{2}{4}\right) - \left(\frac{2}{4}\right) \log_2 \left(\frac{2}{4}\right) = 1$$

$$Entropy\ B = -\left(\frac{3}{5}\right) \log_2 \left(\frac{3}{5}\right) - \left(\frac{2}{5}\right) \log_2 \left(\frac{2}{5}\right) = 0.97$$

$$information\ gain\ for\ case\ a = 0.99 - \left(\left(\frac{4}{9}\right) \times 1\right) - \left(\left(\frac{5}{9}\right) \times 0.97\right)$$

$$= 0.00$$

case b:

$$Entropy\ C = -\left(\frac{1}{4}\right) \log_2 \left(\frac{1}{4}\right) - \left(\frac{3}{4}\right) \log_2 \left(\frac{3}{4}\right) = 0.81$$

$$Entropy\ B = -\left(\frac{1}{5}\right) \log_2 \left(\frac{1}{5}\right) - \left(\frac{4}{5}\right) \log_2 \left(\frac{4}{5}\right) = 0.72$$

$$information\ gain\ for\ case\ b = 0.99 - \left(\left(\frac{4}{9}\right) * 0.81\right) - \left(\left(\frac{5}{9}\right) * 0.72\right)$$

$$= 0.23$$

4.1.11 Gini index

Gini Index or Gini impurity is the impurity within a node. In case all the data in a node are similar in measure of a specific feature, the node is considered pure regarding that feature and the Gini index is zero for that specific feature on the node. Gini index can have values anywhere between 0 and 1. The lower end of this range indicates full purity and the upper bound is for full impurity. Gini index can be calculated by formula below.

$$Gini\ index = 1 - \sum_{i=1}^{j} p_i^2 \tag{4-7}$$

Where p_i stands for probability of mode i in the node.

For illustrative purposes, structure on Figure 4-1 is considered and values of Gini index for nodes are presented in Table 4-1. Results indicates that distribution of method is not effective in terms of decreasing impurity as values of Gini index are relatively close or higher than the value of Gini index in parent node of A. on the other hand, splitting process in structure b could decrease values of Gini index in sub-nodes which indicates that this split decreases impurity.

Table 4-1: Gini index values for sample structures.

Parameter	Gini Index
Node A	0.49
Node C (case a)	0.5
Node B (case a)	0.32
Node C (case b)	0.37

4.2 Decision tree

Decision tree is a non-parametric supervised method for machine learning. Supervised learning methods are algorithms where the input variables(features) are determined and labeled. Decision tree has a hierarchical tree structure consisting of a root node, branches, internal nodes and leaf nodes. In the decision tree method, data are split into binary division where the classification is based on values of defined parameters known as features.

Decision tree models can be implemented by variety of algorithms such as ID3, C4.5, CART, and CHAID. Detailed about these algorithms are best described in core machine learning resources such as reference book by Tom Mitchell ($T. Mitchell, 1997$).

A simple tree of decision making in tree-based algorithm is shown in Figure 4-2. Figure 4-3 demonstrates a schematics of decision tree structure.
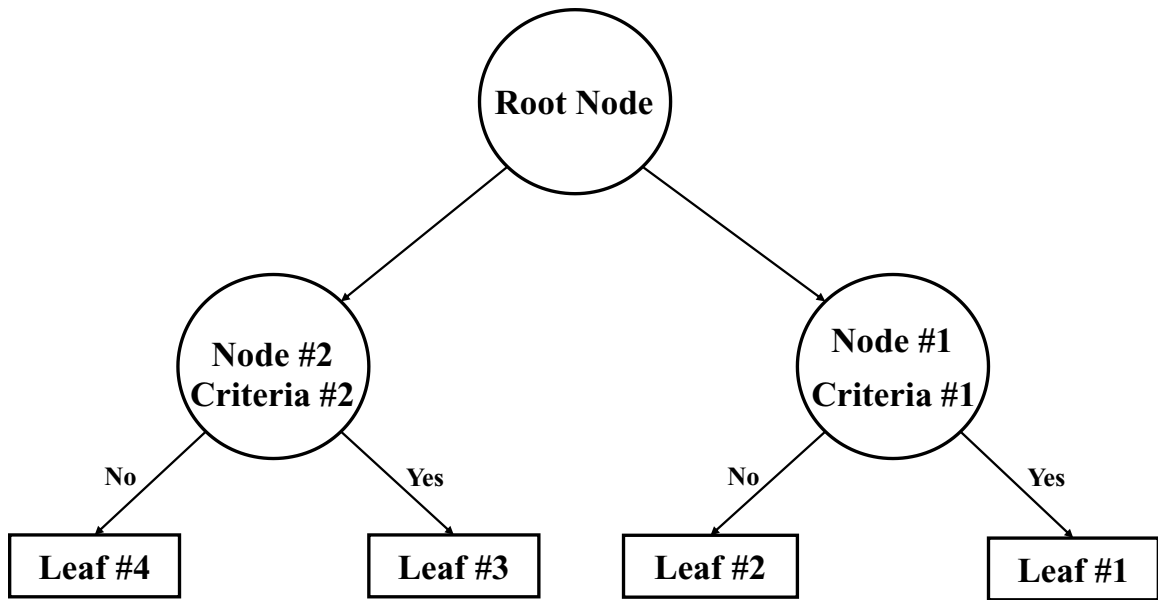
Figure 4-2: A basic tree of decision making.
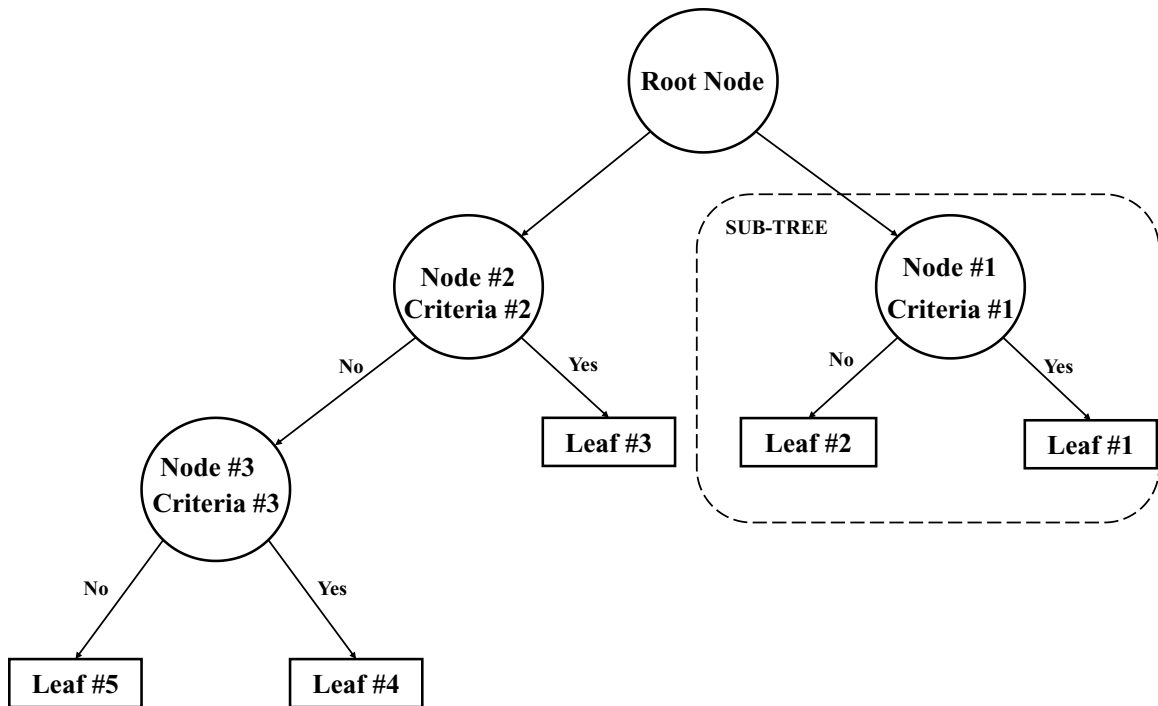
Figure 4-3: Structure of a decision tree algorithm.

4.3   Random forest

Random forest algorithm is an ensemble learning method for classification and regression problems (Azimi et al., 2022b; Breiman, 2001). This algorithm is an extended version of Classification and Regression Tree (CART) algorithm. While overfitting being a common problem for methods developed based on CART algorithm, Random Forest algorithm is robust against overfitting and therefore, has higher reliability (Breiman, 2001).

TRAINING DATASET

CREATING SUBDATASETS USING BOOTSTRAP DATA

DATASET 1   DATASET 2   DATASET n

Tree 1   Tree 2   ...   Tree n

Result 1   Result 2   Result n

Majority voting

Final Result
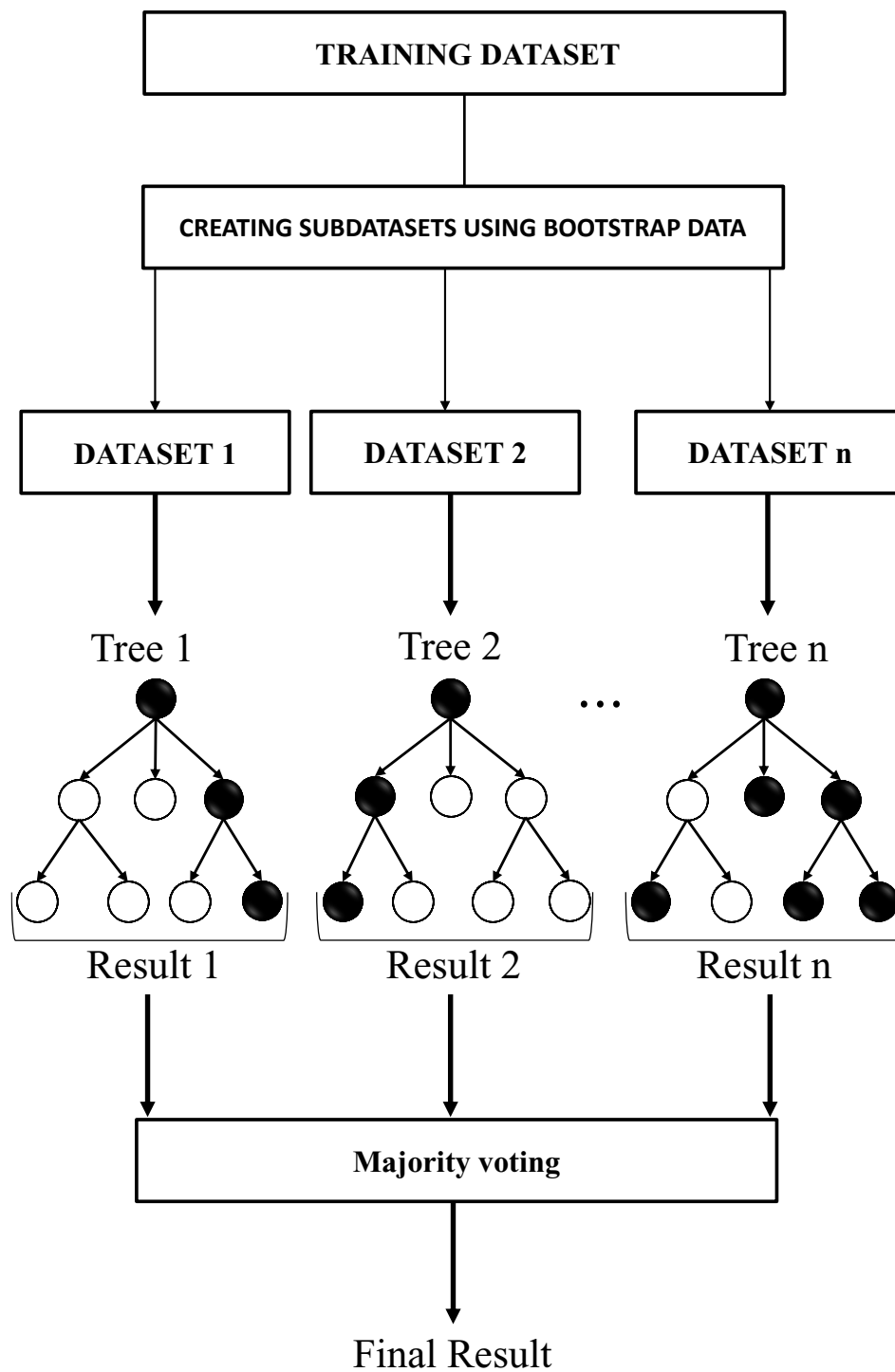
Figure 4-4: Schematic of random forest regression.

In this algorithm, various decision trees are developed, and results are selected based on highest number of votes (Azimi et al., 2022b; Breiman, 2001; Sahani & Ghosh, 2021). In random forest regression, there are increased number of trees for a random vector. The tree predictor, input, and output parameter are all considered numerical values. Since the vector of trees is randomly generated and trees are independently generated using training dataset; therefore, the mean squared generalization error is calculated (Azimi et al., 2022b; Sahani & Ghosh, 2021). Employment of weighted correlation between residuals and applied randomization reduces average error in random forest models. In this method, in addition to given set of training data, sets of bootstrap replicas are generated based on given data set to fulfill possible missed data or to boost quality of the tree.

4.4   Extra tree

The algorithm of support vector regression was initially developed by Geurts et al. (Geurts et al., 2006). Both algorithms are based on the development of multiple trees and to select the decisions based on popularity of results. There are two differences between random forest and extra tree, one is that in extra tree algorithm, there is no bootstrap replica data and only the whole given dataset is used for developing set of random trees, and the other is that in extra tree regression, the cutting point for splitting data between leaves is chosen by a random basis(Azimi et al., 2022c; Hameed et al., 2021). In this method, the splitting point is selected by parameters k and $n_{\min}$ where k is number of randomly selected features in the node and $n_{\min}$ is the minimum sample size for a node to be split. Parameters k and $n_{\min}$ are to improve precision and reduce overfitting respectively(Azimi et al., 2022c; Hameed et al., 2021). Flow chart of extra tree regression is presented in Figure 4-5.
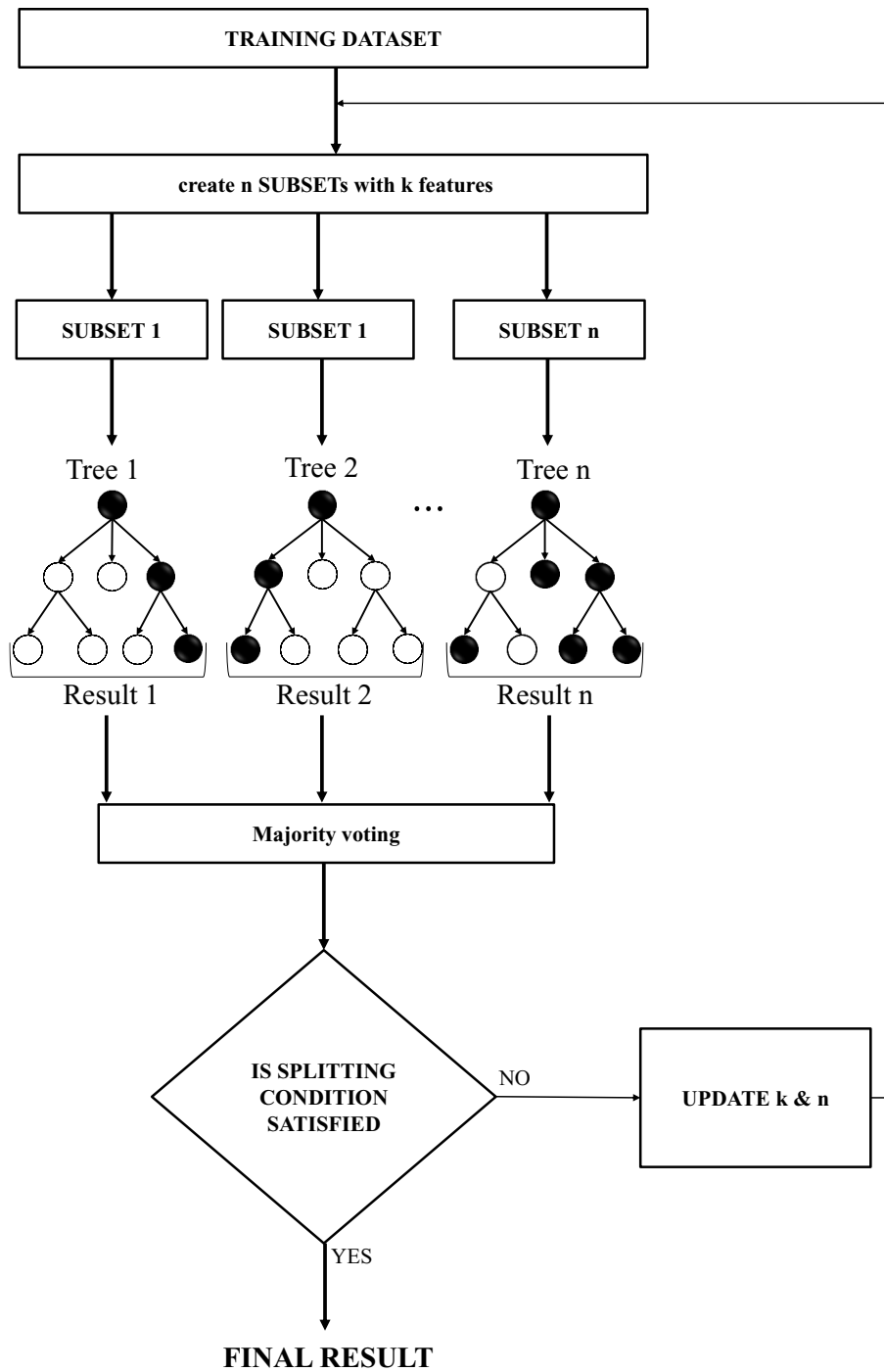
Figure 4-5: Flowchart of extra tree regression.

4.5   Support vector

Support vector algorithm is developed based on the theory of Vapnik-Chervonenkis (VC) theory which has been proposed by Vapnik (Vapnik, 1995). In this algorithm, a transform (Q) is used to map input parameters on a m-dimensional space where m is count of features. In the feature space, a hyperplane is defined to separate features with the highest margin. For regression problems, the transformation function is expected to be nonlinear. Dot product operations can be performed by the kernel functions in a low-feature multidimensional feature space. In practice, support vector regression algorithm employes variety of kernel functions including linear, polynomial, and radial basis functions (RBF) (Azimi et al., 2022a). This algorithm is applicable for a wide range of models covering both classification and regression problems. Performance of this algorithm decreases when modeling datasets with large number of input features. Regarding the nature of vector-approach, performance and accuracy of this method is declined when number of features and consecutively number of dimensions is increased (Rishal Hurbans, 2020).

4.6   Machine learning performance interpretation.

Accuracy of a machine learning model can be statistically measured by performance interpreters such as R^2 score, root mean square error, and mean absolute error. R^2 score is the variance between ML predictions and actual target data used as goal of prediction. R^2 score can range from 0 to 1. The ideal value of this parameter for a fully precise model is 1 and any number closer to 1 means higher accuracy; apparently, the worst condition of this parameter for a model is $R^2 = 0$.

$$R^2 = 1 - \frac{\Sigma \left(y_i - y_{i_p} \right)}{\Sigma (y_i - \bar{y})} \qquad (4\text{-}8)$$

Where y_{i_p} is the value predicted by ML model and y_i is the actual value of target. For an ideal model with 100% accuracy will obtain MAE=0. This parameter can obtain values ranging from 0 to MAE > 0. Regarding the range of inputs, an optimal range of MAE for a realistic approach might vary and there is no certain up limit for MAE.

For mean absolute error we have:

$$MAE = \frac{\Sigma \left(y_i - y_{i_p} \right)}{n} \qquad (4\text{-}9)$$

Where, n is the total number of datapoints.

The last parameter for evaluating performance of machine learning is to calculate deviation between observed data and predicted values through RMSE parameter. This parameter can range from 0 for an ideal model with 100% accuracy up to any value of RMSE > 0. The mean square error can also be obtained by equation below:

$$RMSE = \sqrt{\frac{\Sigma \left(y_i - y_{i_p} \right)^2}{n}} \qquad (4\text{-}10)$$

4.7   Results of machine learning analysis

Results achieved by application of machine learning methods on dataset presented. At first general correlations between input and output parameters are presented and then follows by performance of methods on dataset.

4.7.1   General correlation

General correlation between parameters for single-span cases and multi-span cases are provided in Figure 4-6 and Figure 4-7 respectively. Correlation outlines strength of relationship between two variables. Based on the performed correlation, the impact of parameter Gap aspect ratio on In-line and cross-flow stresses and also in-line and cross-flow natural frequencies is not momentous. the parameter span aspect ratio is significantly affecting all of the in-line and cross-flow stresses and in-line and cross-flow natural frequencies. Regarding the natural frequencies in single-span configuration, in addition to the span aspect ratio, Reynolds number and inverse wall thickness ratio are two influential parameters. For multi-span configuration, the span aspect ratio is also a substantial feature for all of the in-line and cross-flow stresses and in-line and cross-flow natural frequencies. Similar to the single-span configuration, gap ratio doesn't have noticeable impact on performance of multi-spanning pipelines. Based on the correlation between parameters of multi-span configuration, features of Inverse wall thickness ratio, relative span aspect ratio, and Reynolds number are expected to be important in in-line and cross flow-stresses and in-line and cross-flow natural frequencies.

Even though the gap aspect ratio has no significant impact of pipeline performance, this parameter plays a critical role on rapid failure of pipeline due to collision between seabed and pipeline during VIV vibrations.
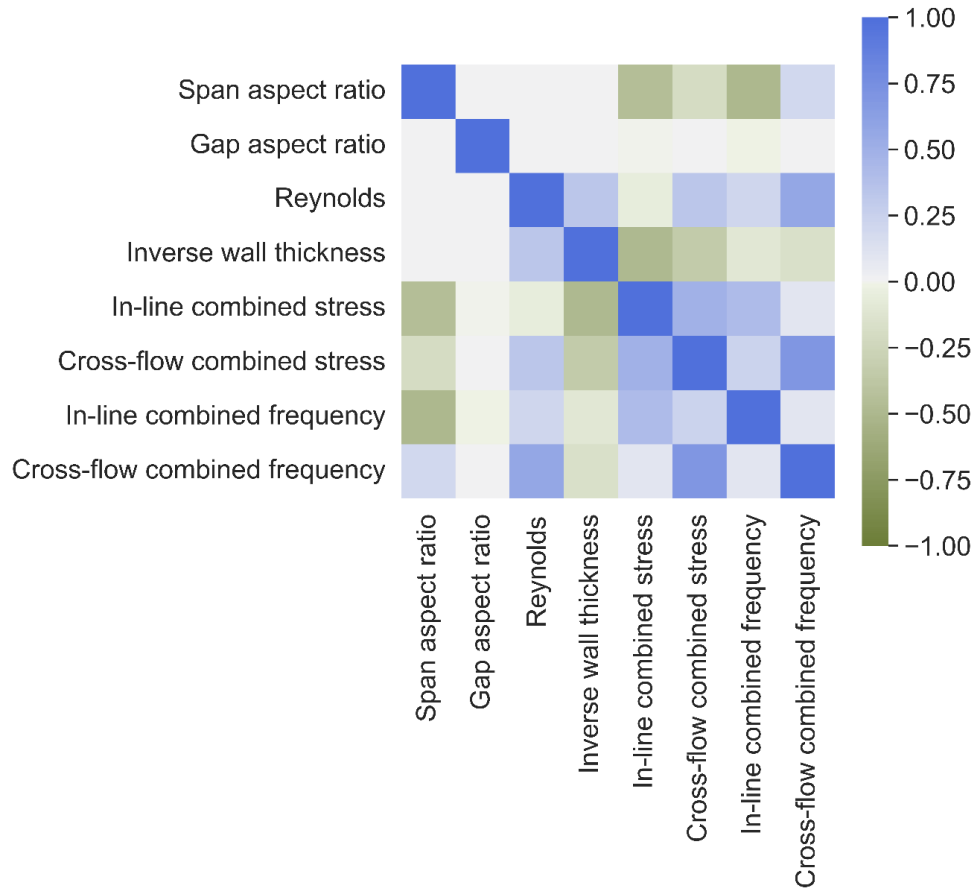
Figure 4-6: General correlation between input features and output parameters for single-spanning configuration.
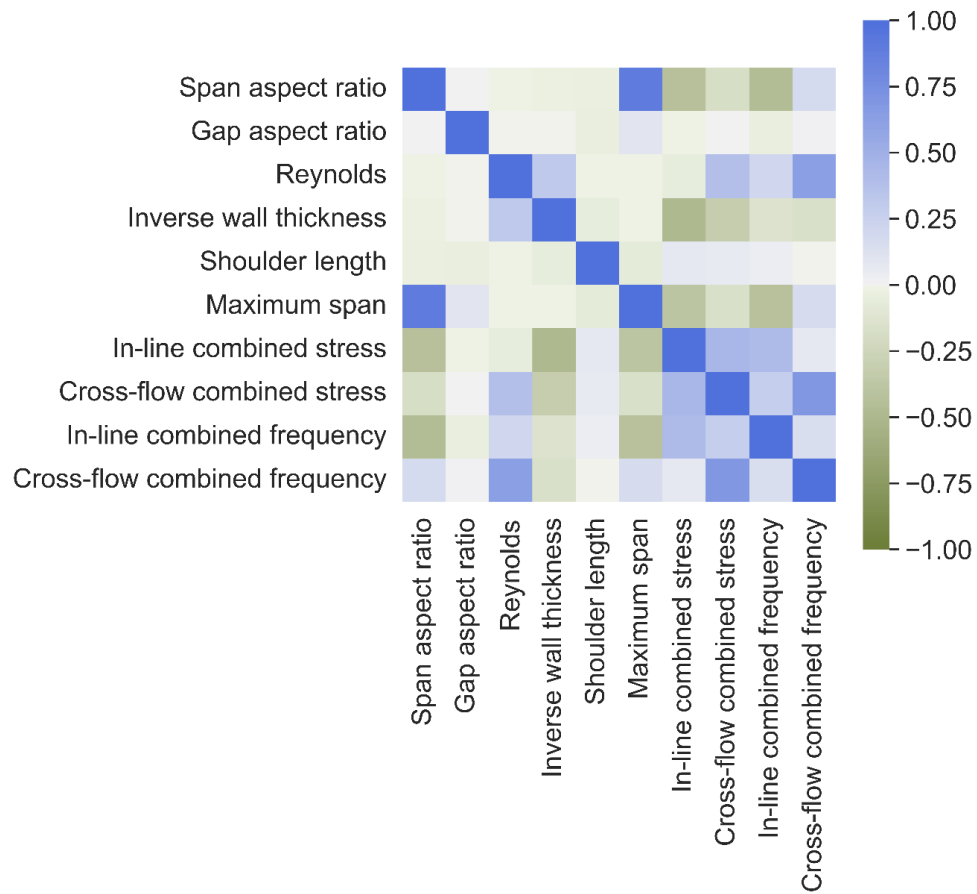
Figure 4-7: General correlation between input features and output parameters for multi-spanning configuration.

There are four different machine learning algorithms employed in this research including Decision Tree (DTR), Extra Tree (ETR), Random Forest (RFR), and Support Vector (SVR). The SVR model showed relatively lower precision in results. SVR is mostly a choice for problems with not too many involved features. Regarding low initial accuracy of SVR. Performance of employed methods on prediction of VIV stresses in in-line, cross-flow directions, structural natural frequencies in in-line and cross-flow direction, and the maximum VIV stress for single-span configuration are demonstrated are presented as follow.

4.7.2 In-line VIV stress of single-span configuration

Performance of different machine learning methods on prediction of combined VIV natural frequency in in-line direction of single span configuration are presented in Table 4-2 and Figure 4-8. For this parameter, decision tree model gives best precision followed by other Tree-base models. It can be concluded that method of decision tree regression (DTR) is fully compatible with this dataset and implementation of random forest regression (RFR), or extra tree regression (ETR) methods will not improve the results. The initial regression by method of support vector had no acceptable results, therefore, using hyper parameter optimization, the SVR model has been successfully tuned to be compatible with dataset. Even though the improvement in accuracy of SVR was noticeable, the SVR model could not surpass the DTR model; therefore, DTR model is considered best possible option for this dataset. The scatter plot of test dataset is presented Figure 4-9. As it noticeable within scatter plots, the deviation in SVR model is much higher than tree-base models. All of the tree-base model shown good accuracy with minor deviations.

Table 4-2: ML accuracy for prediction of in-line VIV stress in single-span configuration.

ML method	R2 score	MAE	RMSE
DTR	0.999	0.069	0.321
ETR	0.996	0.439	1.475
RFR	0.992	0.684	2.031
SVR	0.992	4.15	7.13
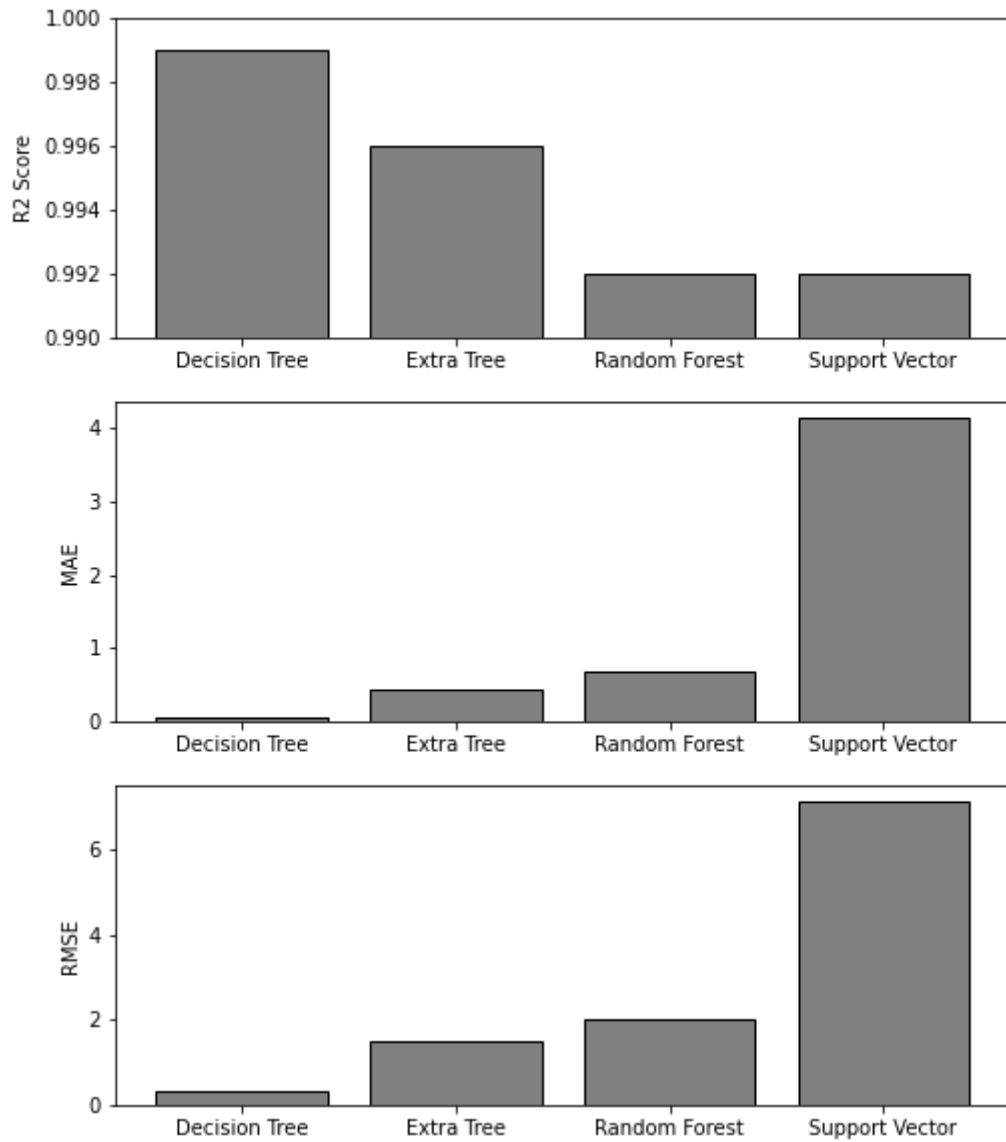
Figure 4-8: Comparative chart of ML accuracy for prediction of in-line VIV stress in

single-span configuration.
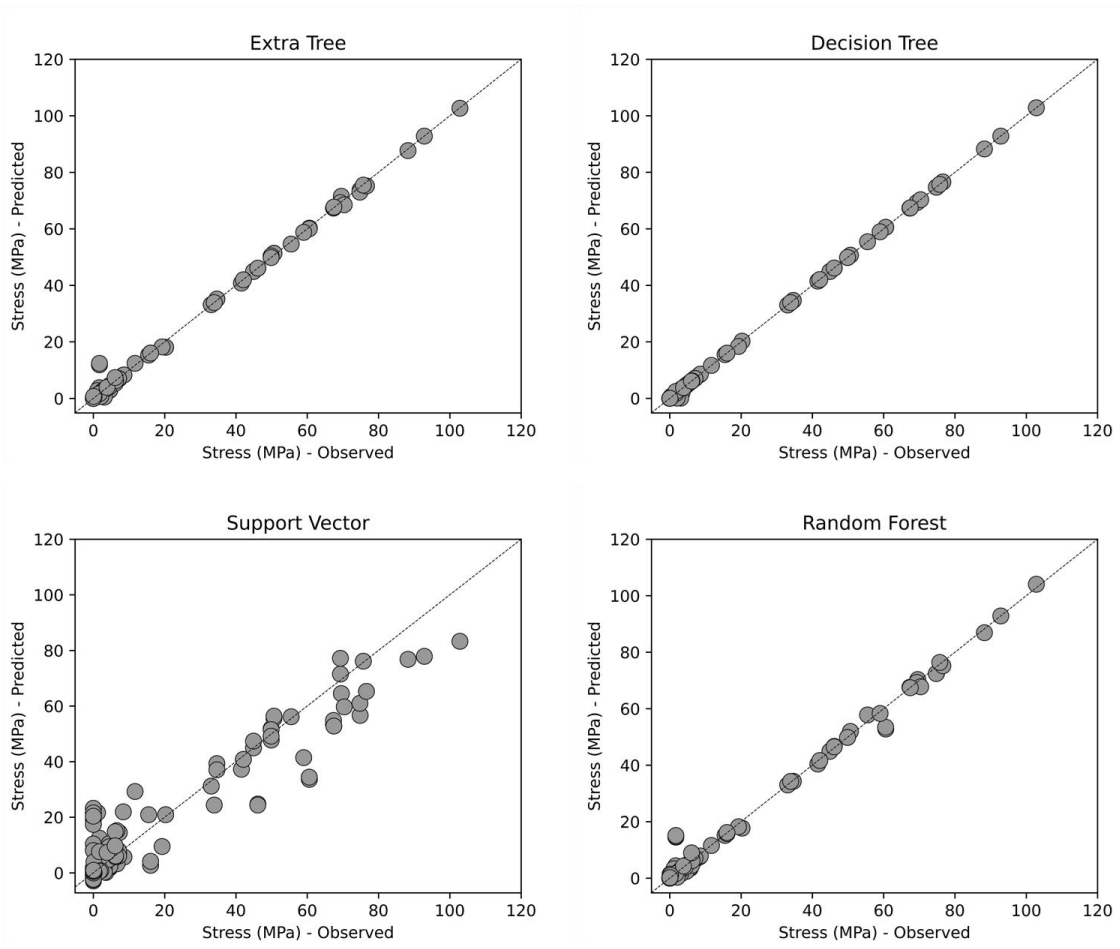
Figure 4-9: Scatter plot of ML models on prediction of in-line mode stress in single-span.

4.7.3   Cross-flow VIV stress of single-span configuration

Numerical results and comparative charts of performance of ML methods on this parameter are presented in Table 4-3 and Figure 4-10 respectively. Similar to in-line direction, the most accurate model for prediction of cross-flow VIV stress in single-span configuration can be achieved by using DTR method. ETR and RFR models could also deliver a great level of accuracy. Since implementation of SVR model could not deliver promising precision, the SVR model has been tuned by using hyper parameter optimization which could significantly improve the accuracy of model. Even though the tuned model had much higher accuracy, the accuracy of this model was not admissible; therefore, using SVR method is not recommended for this dataset. Scatter plot of results for this dataset are presented in Figure 4-11.

Table 4-3: ML accuracy for prediction of cross-flow VIV stress in single-span
configuration.

ML method	R2 score	MAE	RMSE
DTR	0.998	0.039	0.168
ETR	0.996	0.091	0.242
RFR	0.989	0.162	0.402
SVR	0.641	0.847	1.933
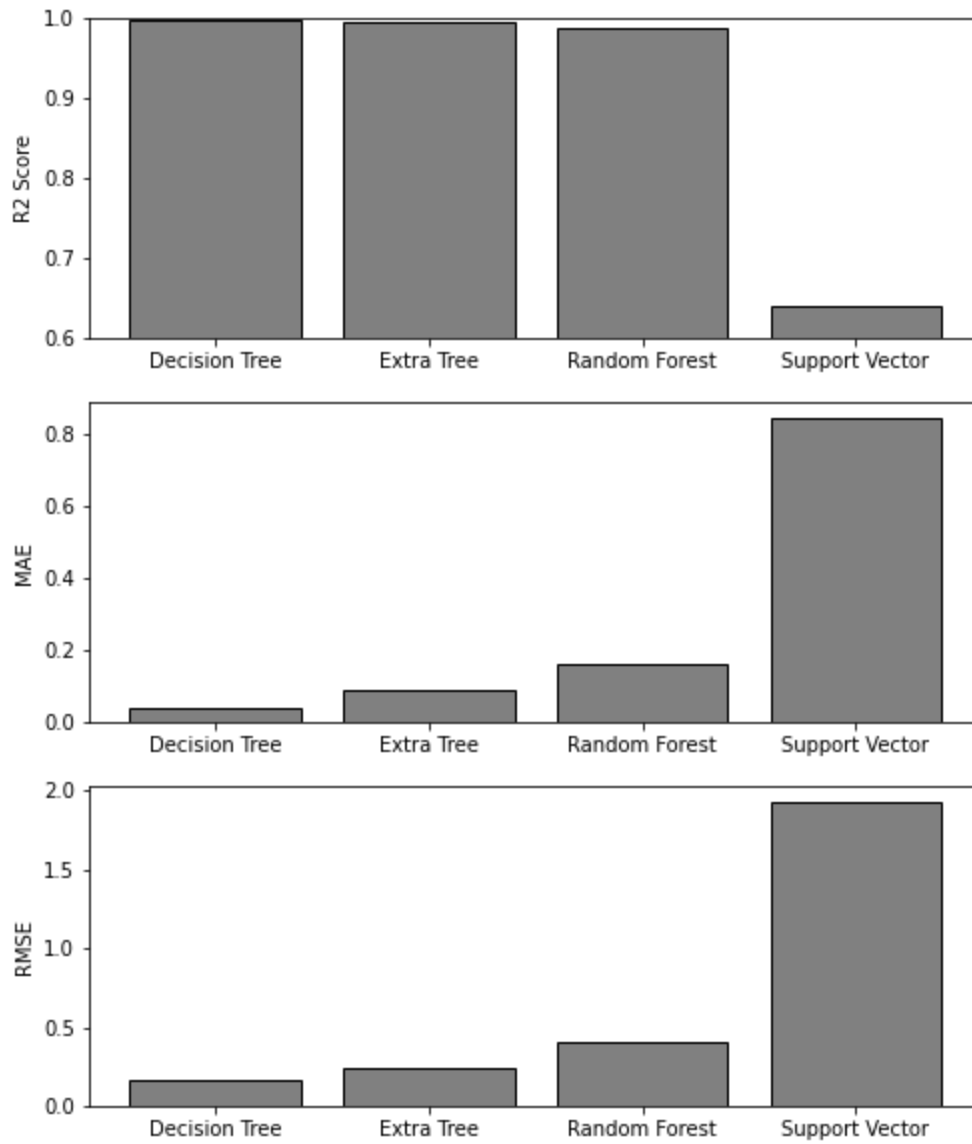
Figure 4-10: Comparative chart of ML accuracy for prediction of cross-flow VIV stress

in single-span configuration.
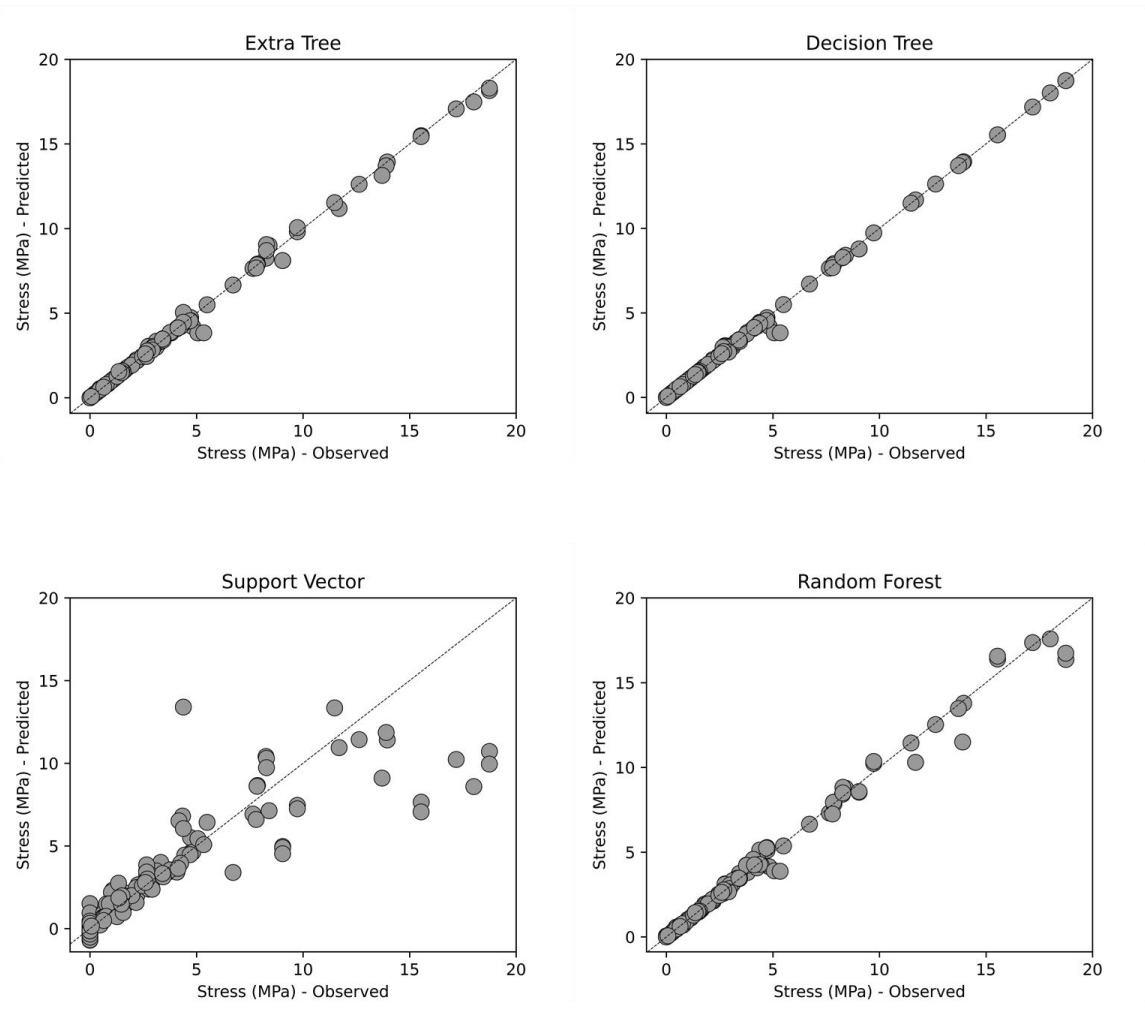
Figure 4-11: Scatter plot of ML models on prediction of Cross-flow mode stress in
single-span.

4.7.4 Maximum VIV stress of single-span configuration

The maximum cross-flow and in-line stresses of single-span configuration have been considered for this dataset. Tree-based methods namely DTR, ETR, and RFR proved to have decisive quality where ETR has minor advantage over two other methods. Numerical results and comparative charts are provided in Table 4-4 and Figure 4-12 followed by scatter plot presented in Figure 4-13. The model trained by method of ETR could give highest level of accuracy. RFR and DTR models have also great performance but the SVR model despite improvements achieved by hyper parameter optimization, has relatively lower accuracy. Figure 4-14 presents a comparison between maximum VIV stresses in in-line and cross-flow directions for single-span configuration. Based on the results, it can be concluded that the maximum in-line VIV stress for structures with pipe sizes 5,6, and 8 is significantly higher then maximum cross-flow VIV stress, while for pipelines with pipe sizes of 10,12, 14, and 16, the difference between values of maximum VIV stresses in in-line and cross-flow directions is relatively smaller. It can also be concluded that increase in size of the pipe has greater influence on maximum VIV stresses in in-line direction.

Table 4-4: ML accuracy for prediction of maximum VIV stress in single-span configuration.

ML method	R2 score	MAE	RMSE
DTR	0.992	0.319	2.030
ETR	0.998	0.349	1.019
RFR	0.995	0.606	1.636
SVR	0.880	3.919	7.097
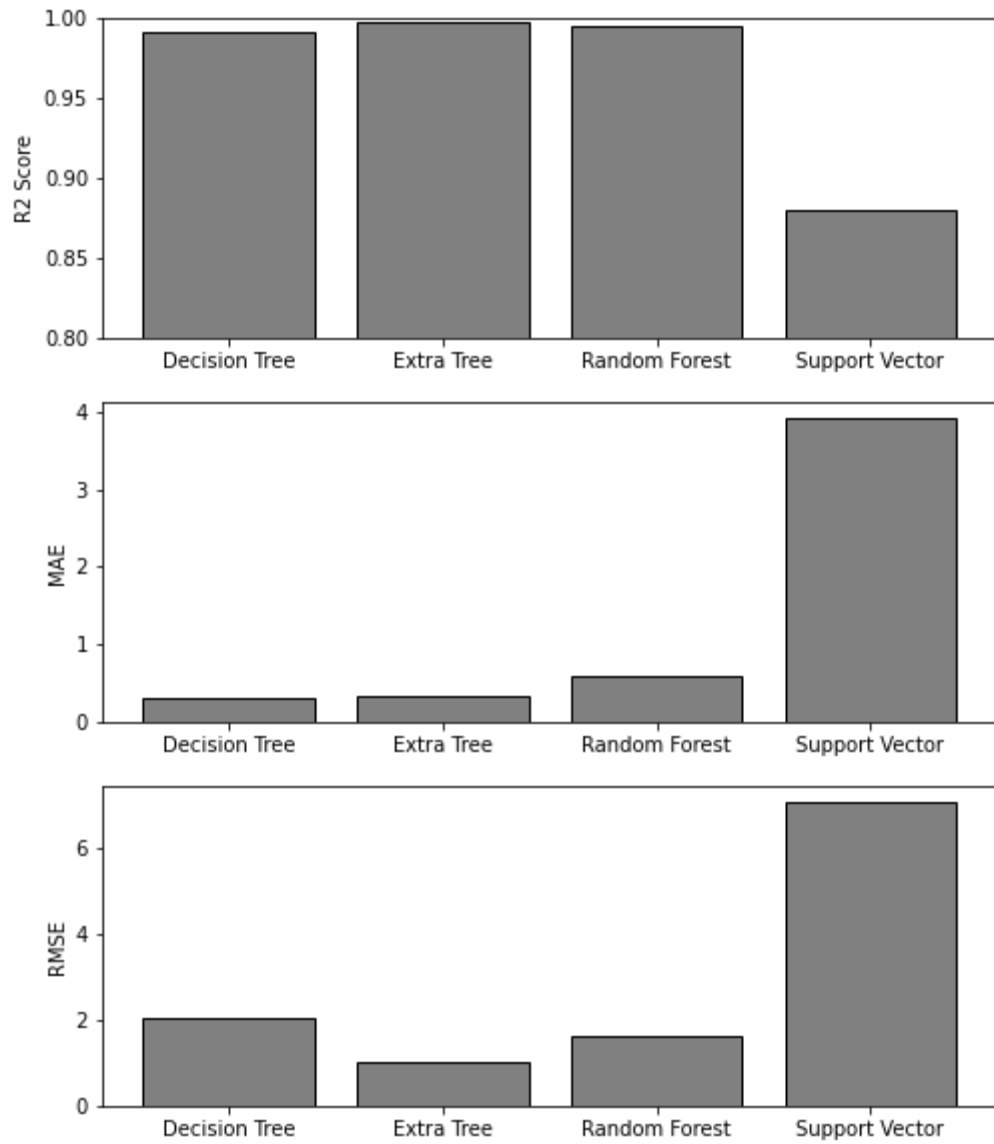
Figure 4-12: Comparative chart of ML accuracy for prediction of maximum VIV stress in

single-span configuration.
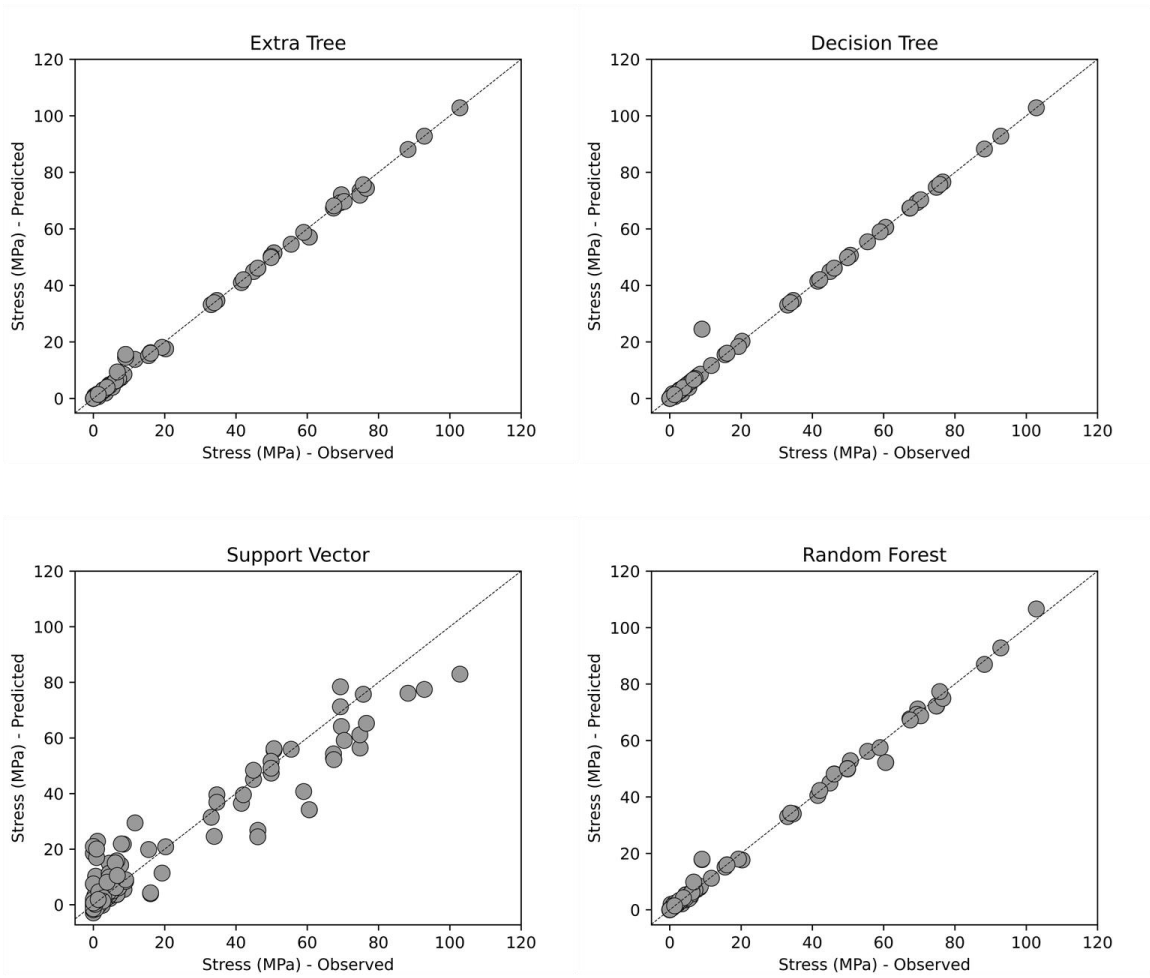
Figure 4-13: Scatter plot of ML models on prediction of maximum VIV stress in single-

span.
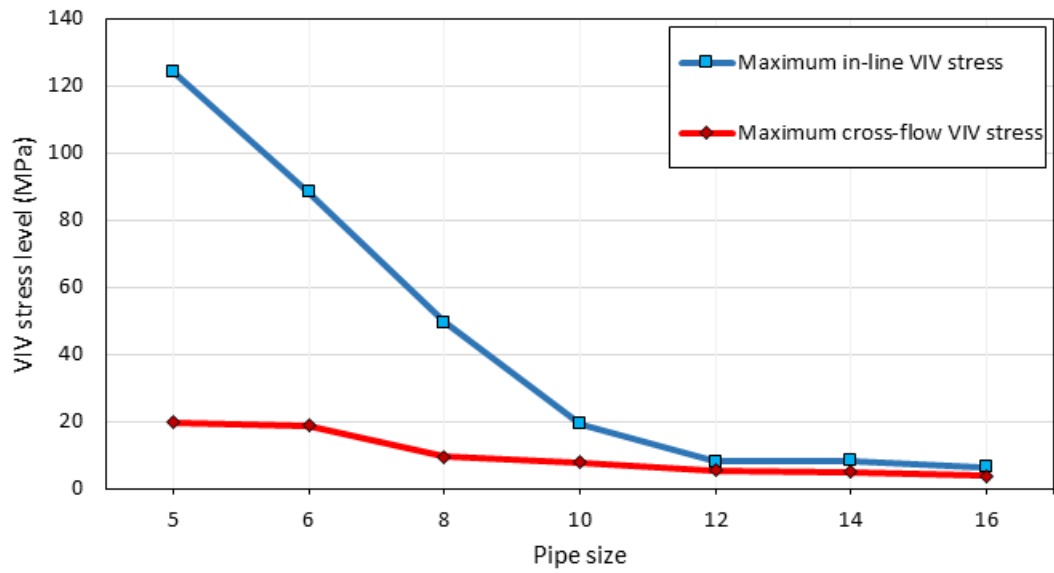
Figure 4-14: VIV stress level in single-span configuration.

4.7.5 In-line VIV frequency of single-span configuration

In this part, performance of machine learning methods in prediction of in-line VIV frequencies are presented. Numerical comparison and comparative performance chart presented in Table 4-5 and Figure 4-15. For this dataset, ETR was found to have the best performance while DTR and RFR have also great performance. Despite implementation of hyper parameter optimization, SVR model is not satisfactory. Scatter plots for different methods are outlined in Figure 4-16.

Table 4-5: ML accuracy for prediction of in-line VIV frequencies in single-span configuration.

ML method	R2 score	MAE	RMSE
DTR	0.961	0.127	0.590
ETR	0.987	0.105	0.327
RFR	0.978	0.188	0.426
SVR	0.586	1.029	1.491
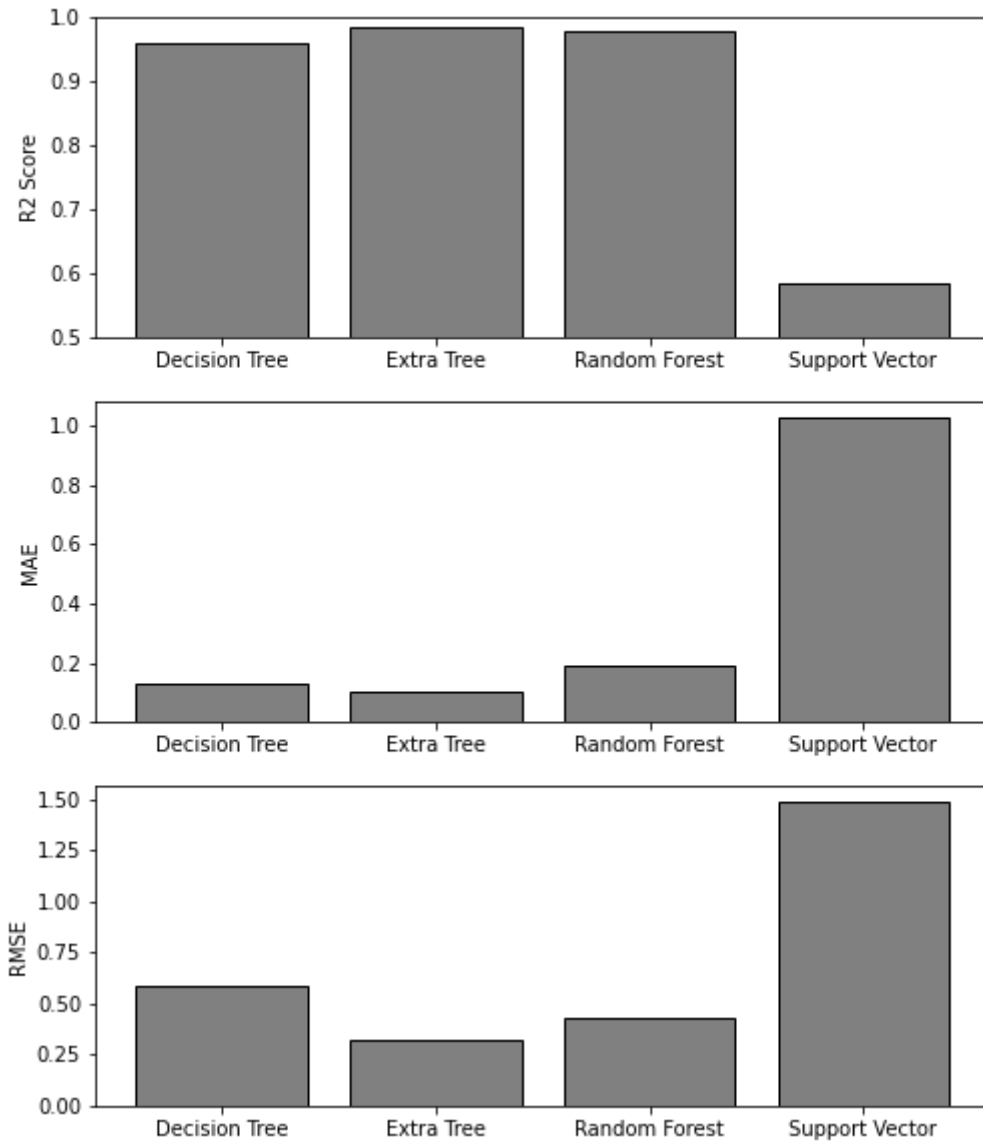
Figure 4-15: Comparative chart of ML accuracy for prediction of in-line VIV frequencies in single-span configuration.
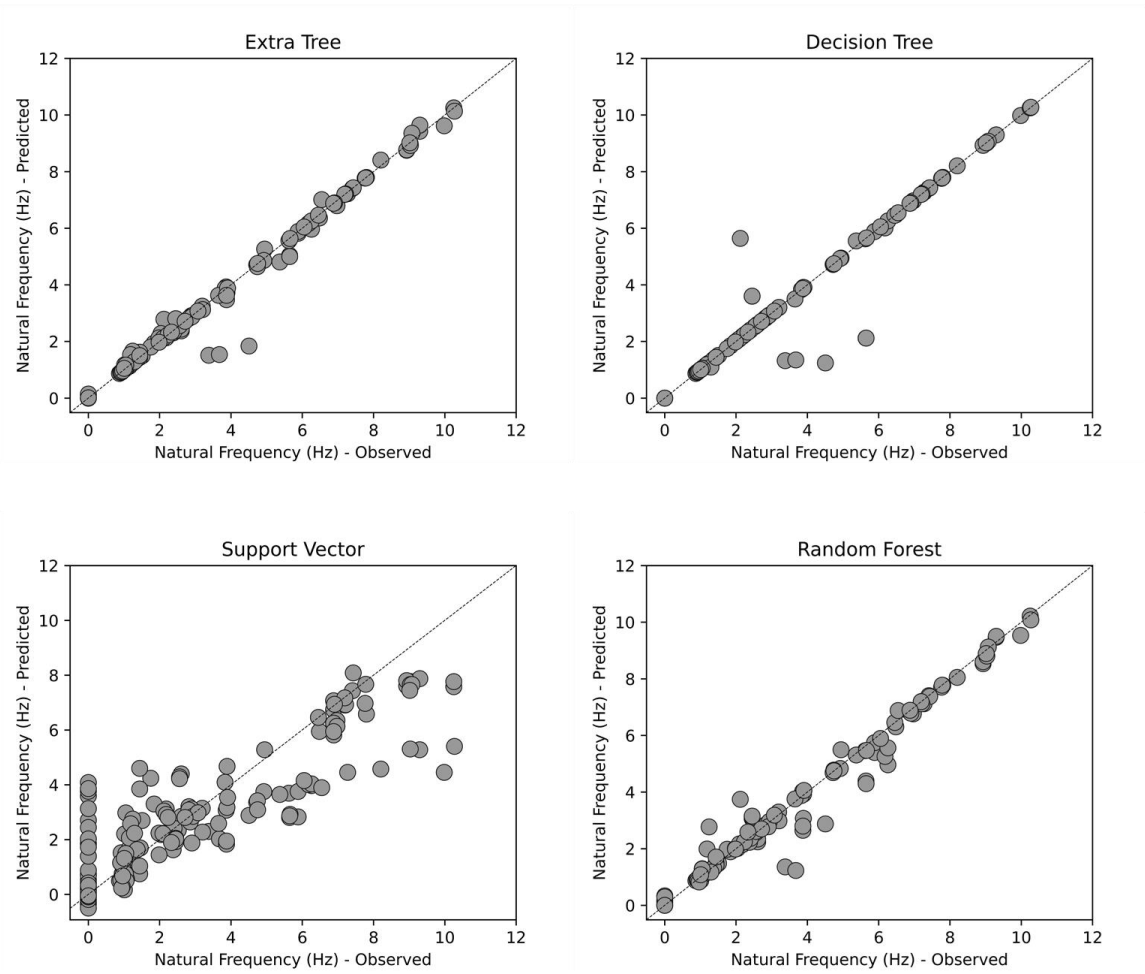
Figure 4-16: Scatter plot of ML models on prediction of in-line natural frequencies in

single-span.

4.7.6 Cross-flow VIV frequency of single-span configuration

Performance of different methods on prediction of combined VIV natural frequency in cross-flow direction are presented in Figure 4-17 respectively. For this dataset, the tree-based models showed great accuracy and none of them has significant superiority over others. The hyper parameter optimization has been implemented on SVR to improve the accuracy of SVR model of this dataset. The optimized SVR model resulted in good accuracy. Overall, the RFR model can be selected as the most accurate representative for the behavior of structure for this dataset. Divergence between predicted values of observed data (FEA) are presented in scatter plots of Figure 4-18 .

Table 4-6: ML accuracy for prediction of cross-flow VIV frequencies in single-span configuration.

ML method	R2 score	MAE	RMSE
DTR	0.994	2.257	3.451
ETR	0.989	2.254	3.450
RFR	0.992	2.214	3.402
SVR	0.838	1.969	2.891
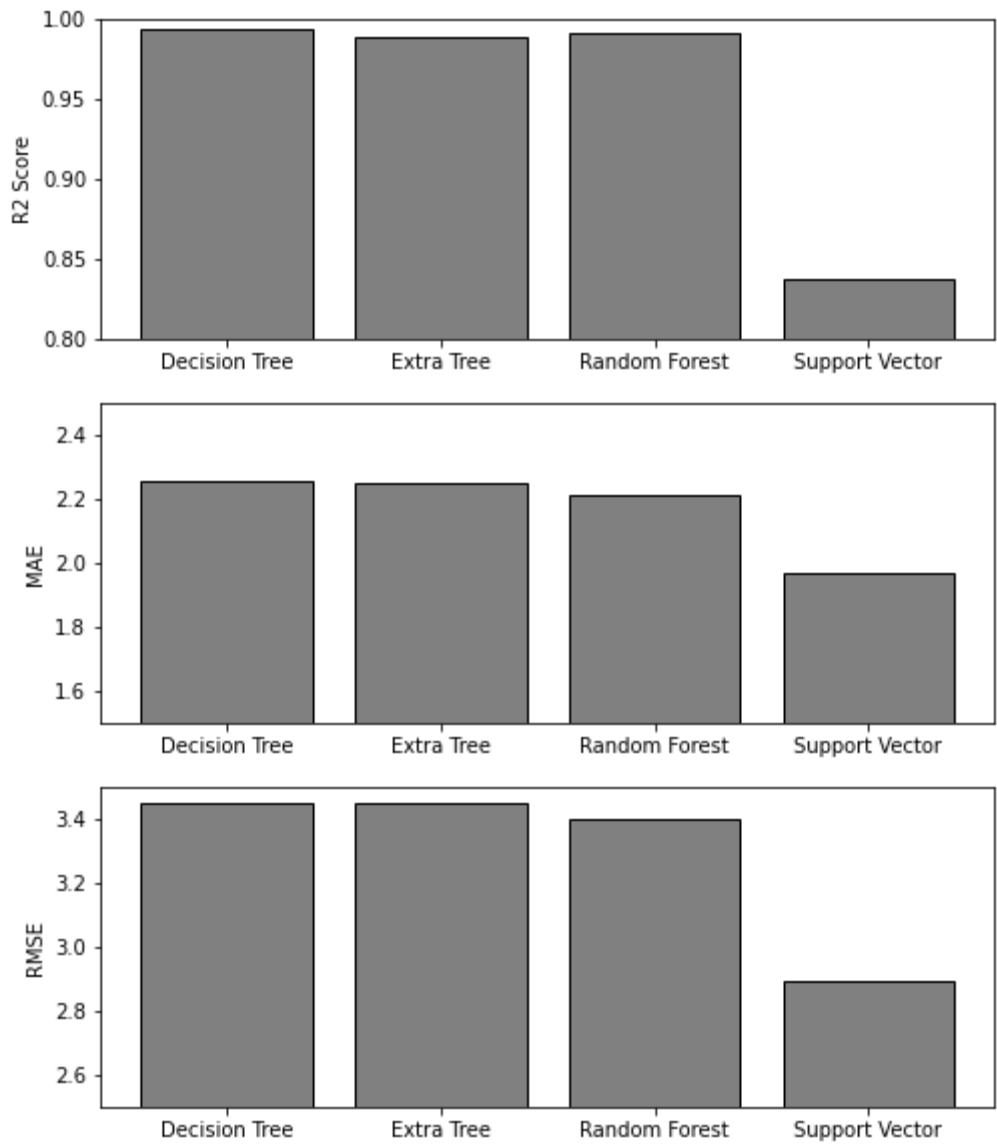
Figure 4-17: Comparative chart of ML accuracy for prediction of cross-flow VIV

frequencies in single-span configuration.
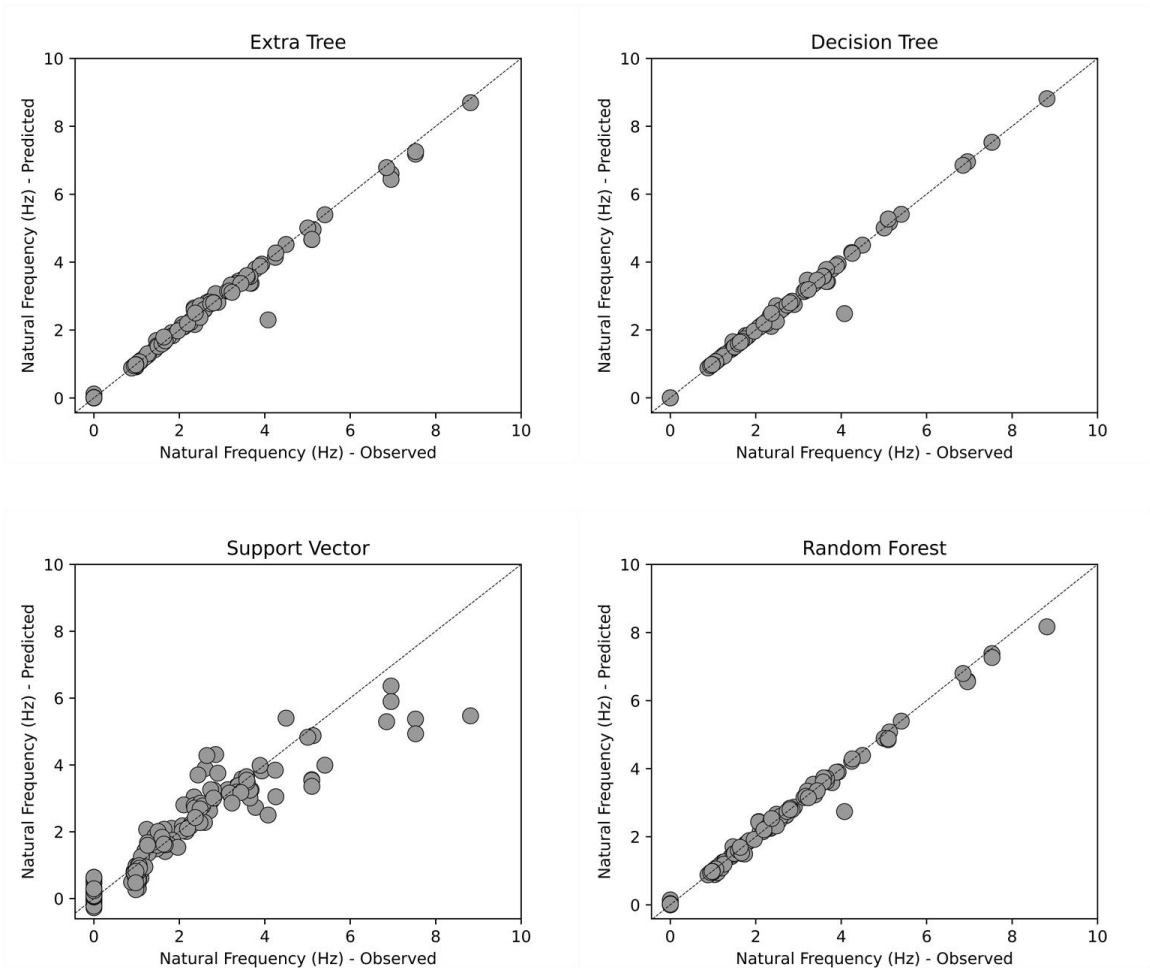
Figure 4-18: Scatter plot of ML models on prediction of cross-flow natural frequencies in single-span.

4.7.7 In-line VIV stress of multi-span configuration

Performance of machine learning methods for prediction of in-line VIV stress is presented. Performed comparison between performance of different methods is presented in Table 4-7 and Figure 4-19. All of the models proved to have great performance on this dataset

where RFR model had a slight advantage over DTR and ETR. Scatter plots of test data are presented Figure 4-20.

Table 4-7: ML accuracy for prediction of in-line VIV stress in multi-span configuration.

ML method	R2 score	MAE	RMSE
DTR	0.992	0.789	1.953
ETR	0.992	0.789	1.953
RFR	0.992	0.787	1.933
SVR	0.943	2.623	5.171
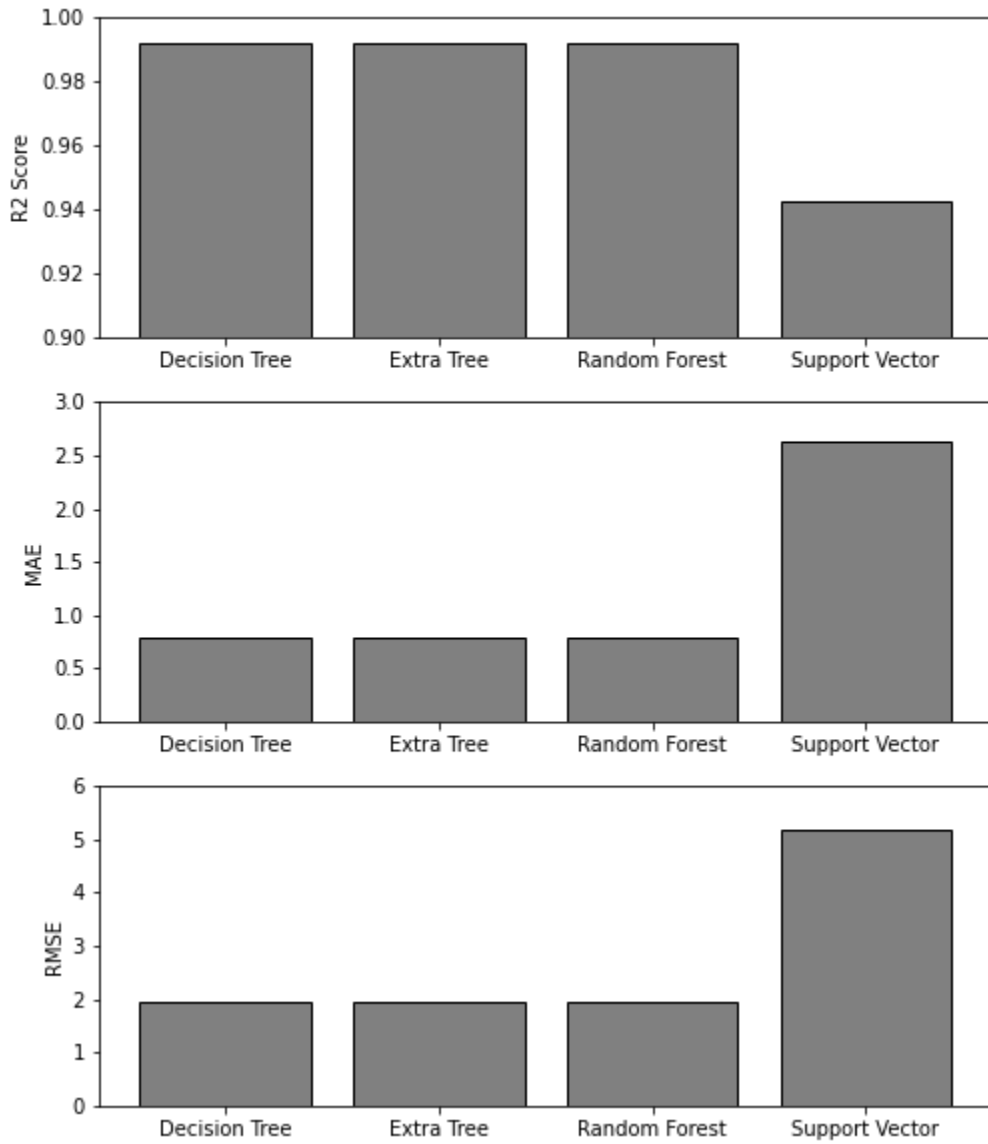
Figure 4-19: Comparative chart of ML accuracy for prediction of in-line VIV stress in

multi-span configuration.
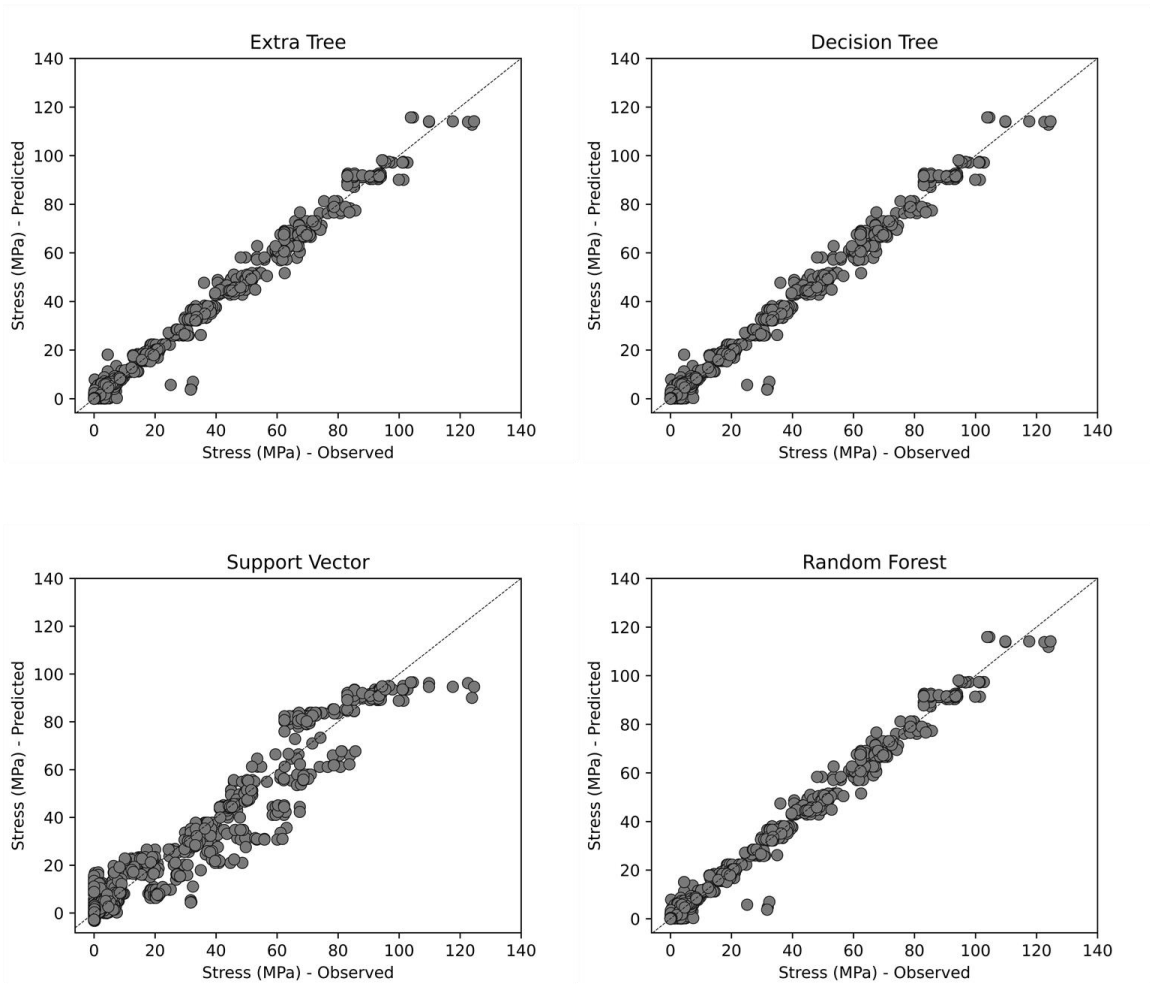
Figure 4-20: Scatter plot of ML models on prediction of In-line mode stress in multi-span.

4.7.8 Cross-flow VIV stress of multi-span configuration

Accuracy of different models for prediction of VIV stress in cross-flow direction is presented in Table 4-8 and Figure 4-21 where all of tree-based method showed great and identical performance and but SVR model had relatively lower performance. Scatter plots of this comparison are presented in Figure 4-22.

Table 4-8: ML accuracy for prediction of cross-flow VIV stress in multi-span configuration.

ML method	R2 score	MAE	RMSE
DTR	0.981	0.177	0.512
ETR	0.981	0.177	0.512
RFR	0.981	0.177	0.513
SVR	0.742	0.571	1.643
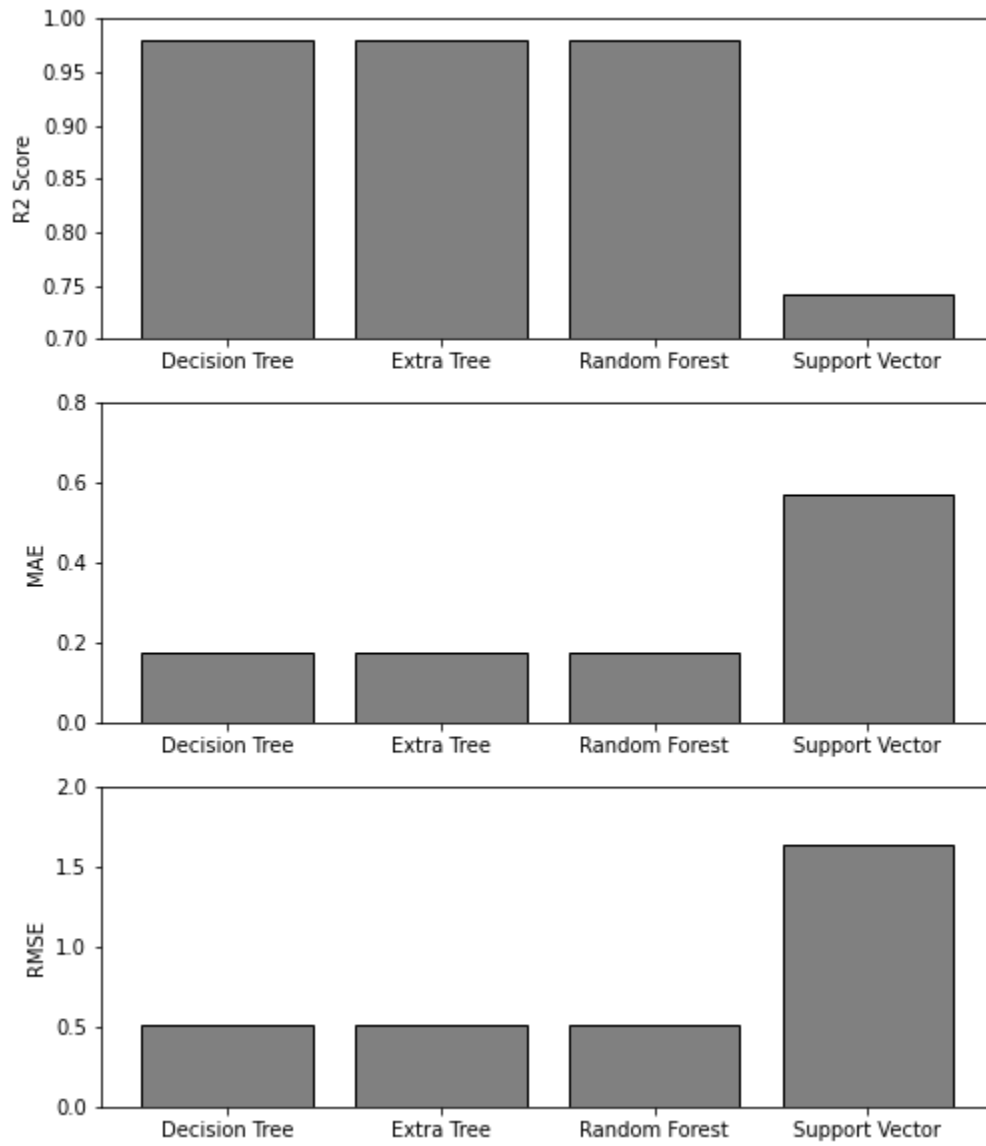
Figure 4-21: Comparative chart of ML accuracy for prediction of cross-flow VIV stress in multi-span configuration.
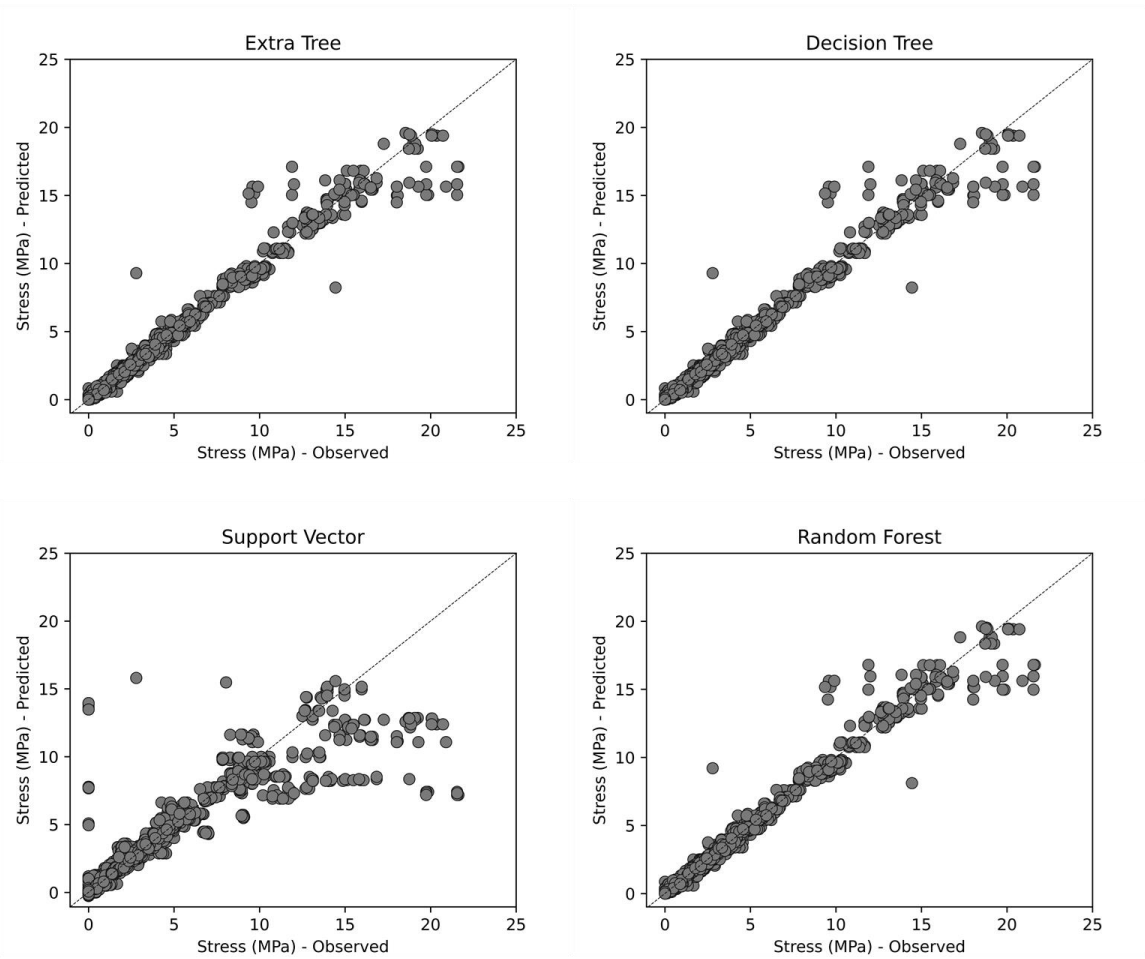
Figure 4-22: Scatter plot of ML models on prediction of cross-flow mode stress in multi-span.

4.7.9   Maximum VIV stress of multi-span configuration

Performance of machine learning models for prediction of maximum VIV stress in multi-span configuration are presented in Table 4-9 and Figure 4-23 where all of the tree-based models namely DTR, ETR, and RFR found to have great performance and their accuracy were relatively similar. The SVR model which is optimized by hyper parameter optimization also found to have decisive precision. Figure 4-25 presents a comparison between maximum VIV stresses in in-line and cross0flow directions where it can be concluded that by increase in pipe size, level of maximum stress in both of in-line and cross-flow directions is declining. For smaller size of pipes, the maximum in-line VIV stress is significantly higher than VV stress in cross-flow direction.

Table 4-9: ML accuracy for prediction of maximum VIV stress in multi-span configuration.

ML method	R2 score	MAE	RMSE
DTR	0.992	0.738	1.869
ETR	0.992	0.738	1.869
RFR	0.992	0.736	1.860
SVR	0.946	2.429	4.989
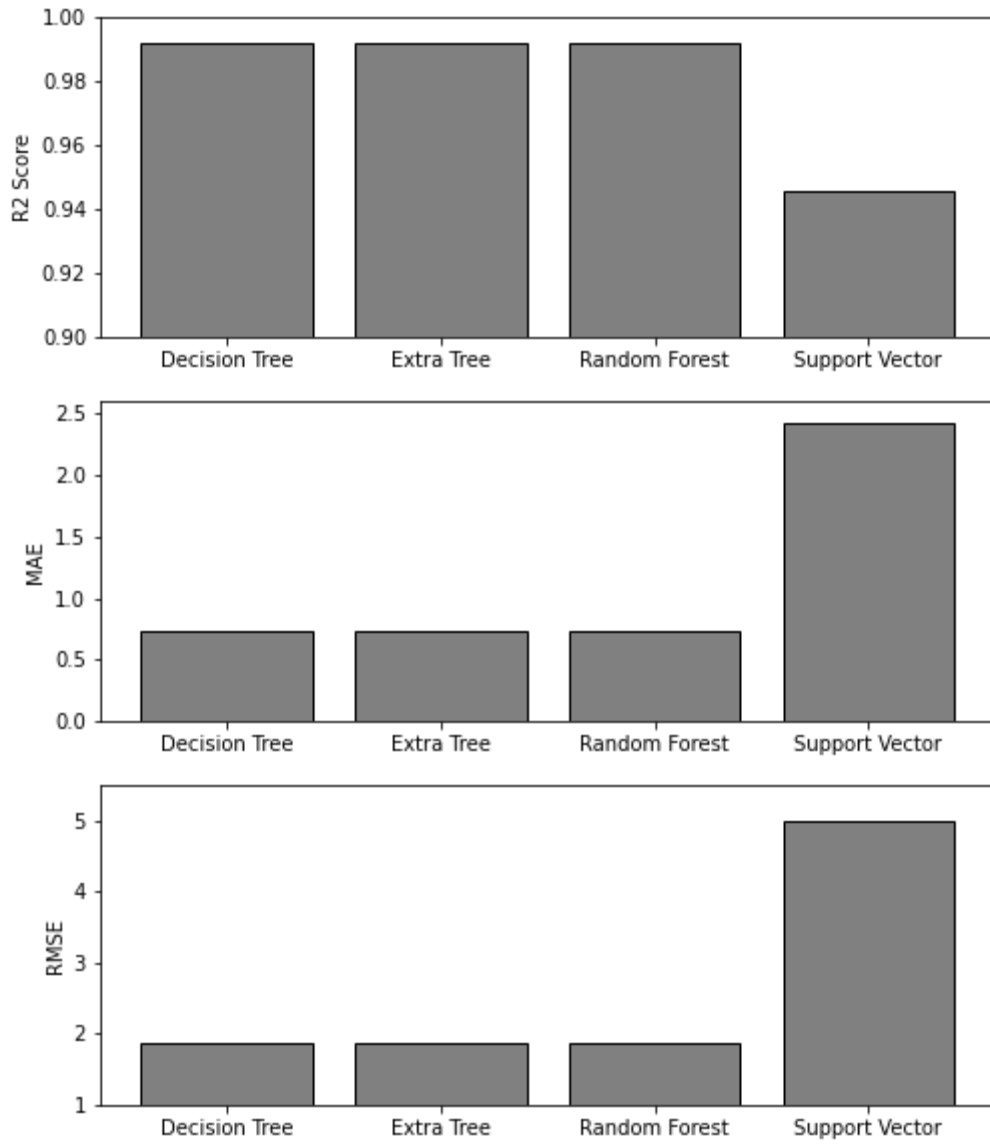
Figure 4-23: Comparative chart of ML accuracy for prediction of maximum VIV stress in multi-span configuration.
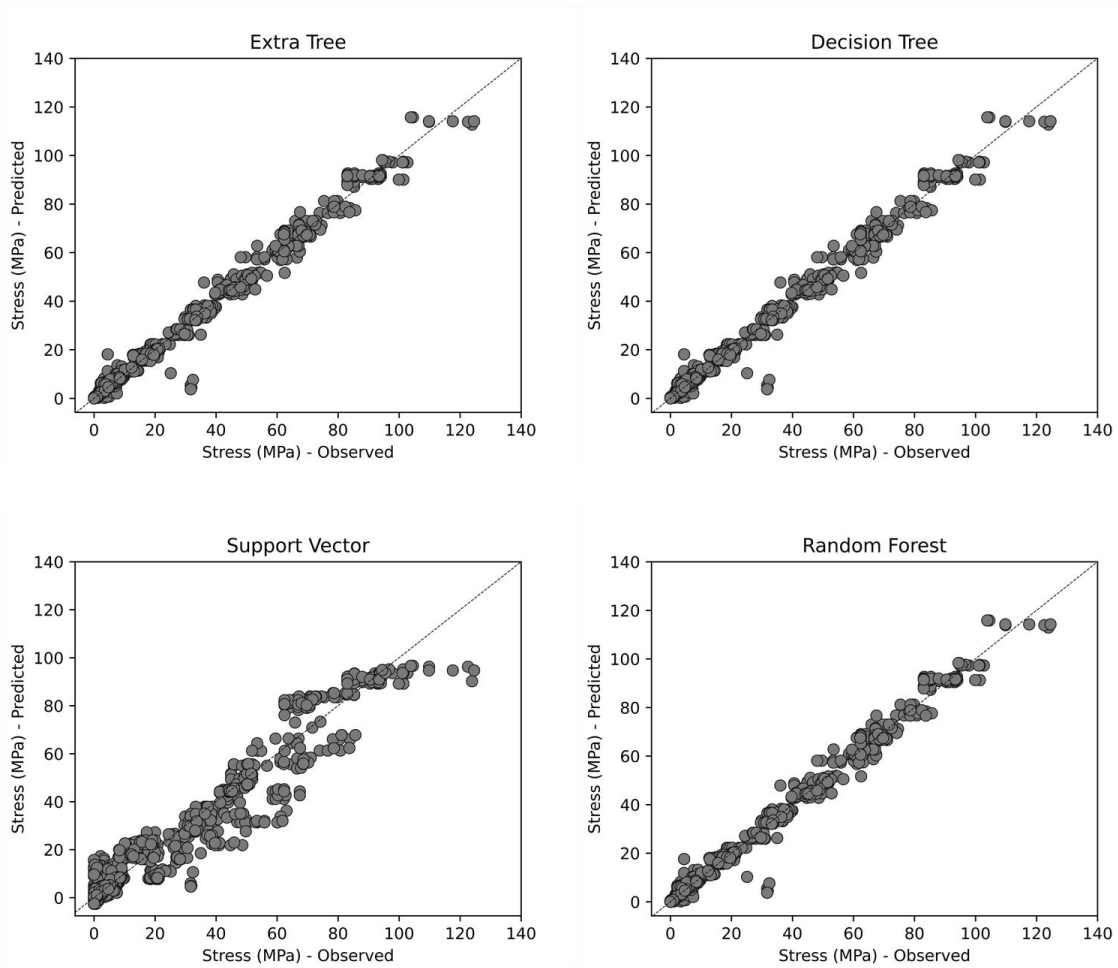
Figure 4-24: Scatter plot of ML models on prediction of maximum mode stress in multi-span.
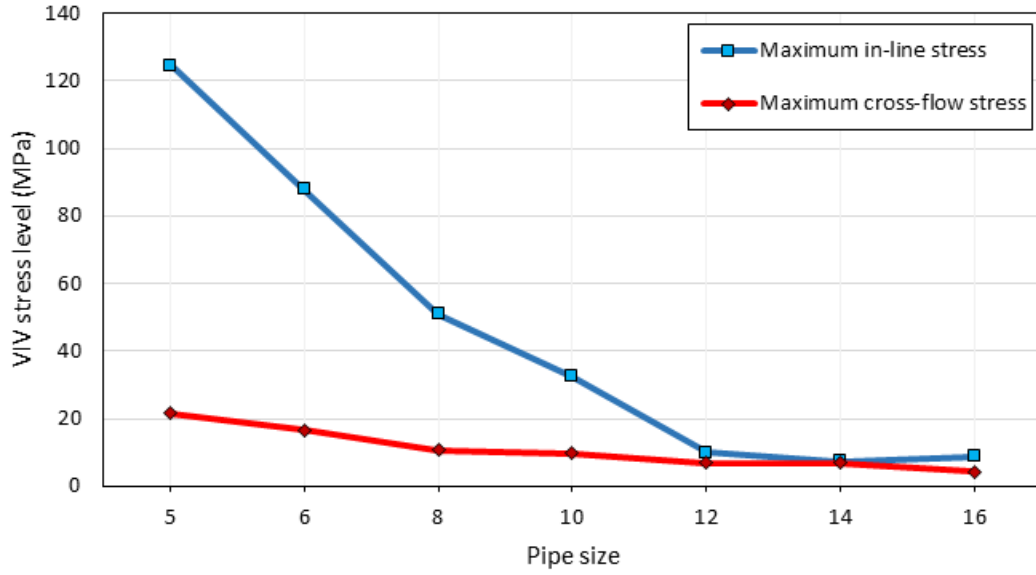
Figure 4-25: VIV stress level in multi-span configuration.

4.7.10 In-line VIV frequency of multi-span configuration

Accuracy of different ML models in prediction of in-line VIV frequency is presented in Table 4-10 and Figure 4-26 where DTR, ETR, and RFR models showed identical performance with good accuracy. The SVR model, which was optimized using hyper parameter optimization, failed to interpret acceptable accuracy. Scatter plots of comparisons are presented Figure 4-27.

Table 4-10: ML accuracy for prediction of in-line VIV frequencies in multi-span configuration.

ML method	R2 score	MAE	RMSE
DTR	0.956	0.170	0.537
ETR	0.956	0.170	0.537
RFR	0.956	0.170	0.538
SVR	0.34	0.98	1.61
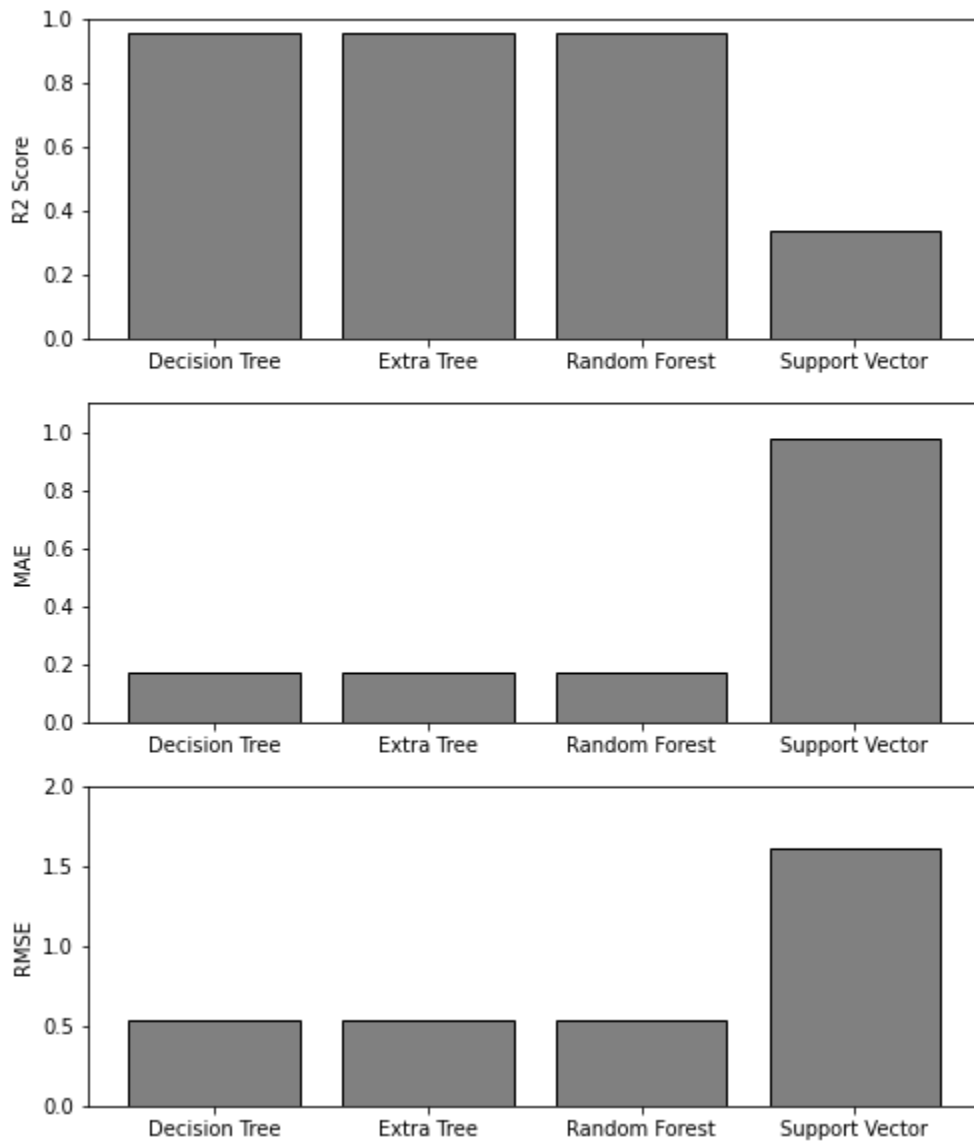
Figure 4-26: Comparative chart of ML accuracy for prediction of in-line VIV frequencies

in multi-span configuration.
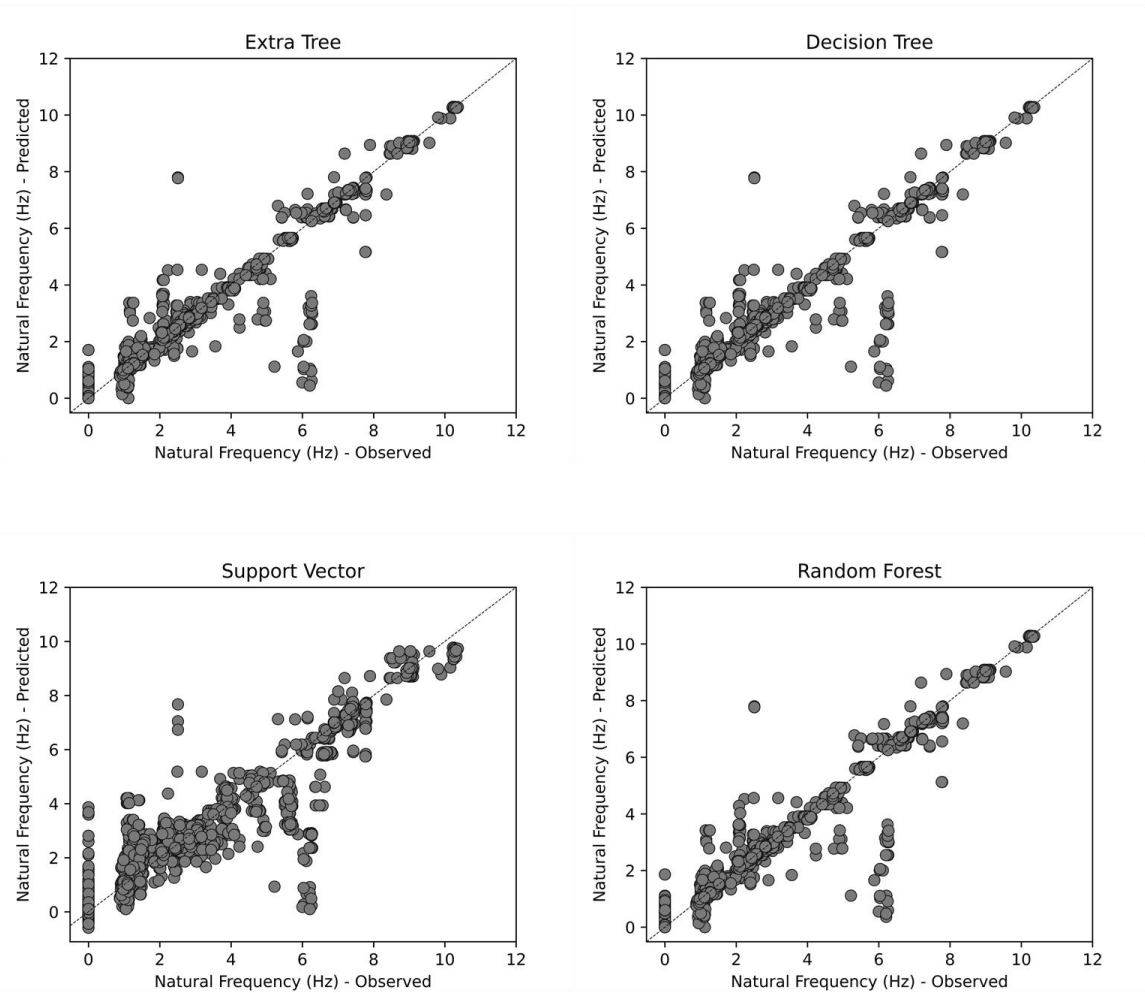
Figure 4-27: Scatter plot of ML models on prediction of In-line natural frequency in

multi-span.

4.7.11 Cross-flow VIV frequency of multi-span configuration

Accuracy of ML methods for VIV frequency in cross-flow direction is presented in.

Table 4-11 and Figure 4-28. DTR, ETR, and RFR models were all found to be accurate, and their performance was similar. Scatter plots for this comparison are presented in Figure 4-29.

Table 4-11: ML accuracy for prediction of cross-flow VIV frequencies in multi-span configuration.

ML method	R2 score	MAE	RMSE
DTR	0.984	1.852	3.017
ETR	0.984	1.852	3.017
RFR	0.984	1.852	3.017
SVR	0.887	1.853	2.967
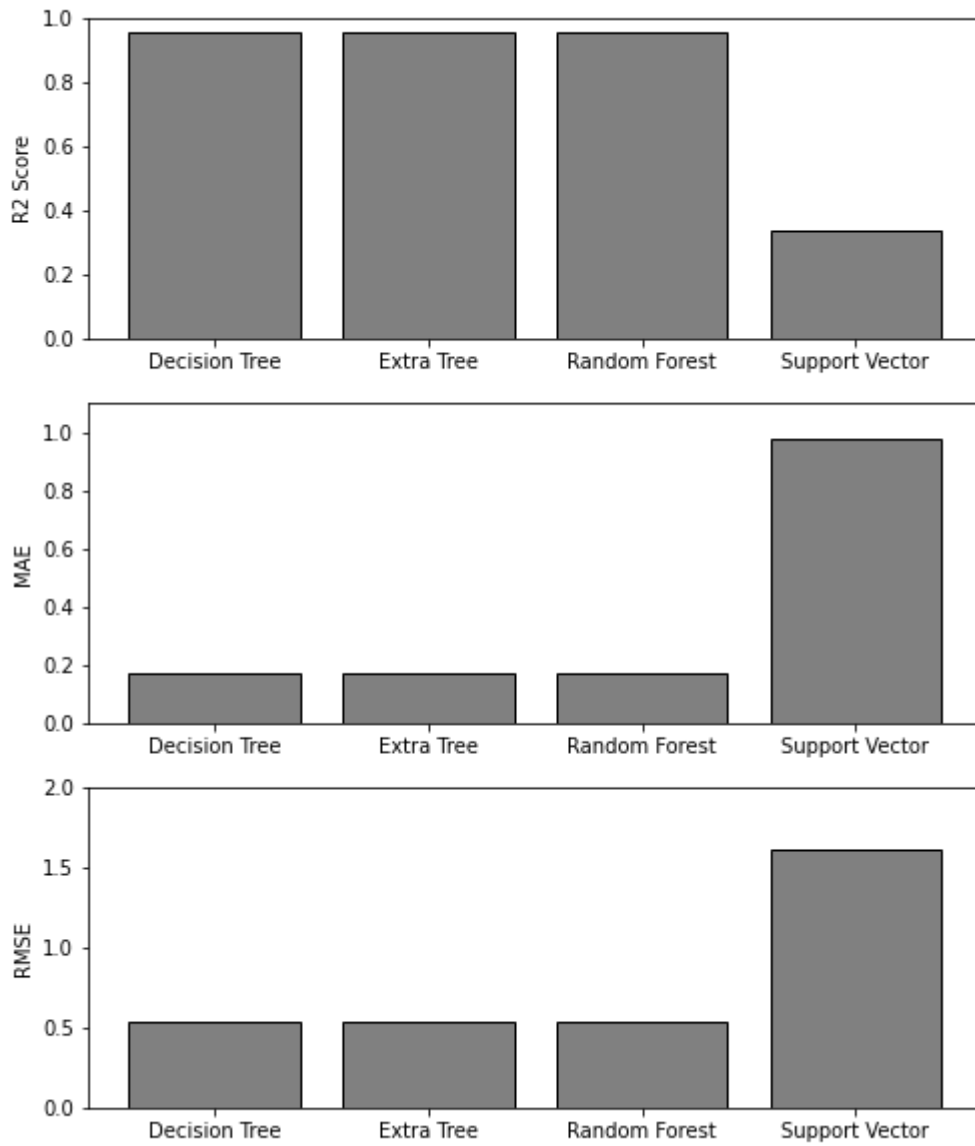
Figure 4-28: Comparative chart of ML accuracy for prediction of cross-flow VIV

frequencies in multi-span configuration.
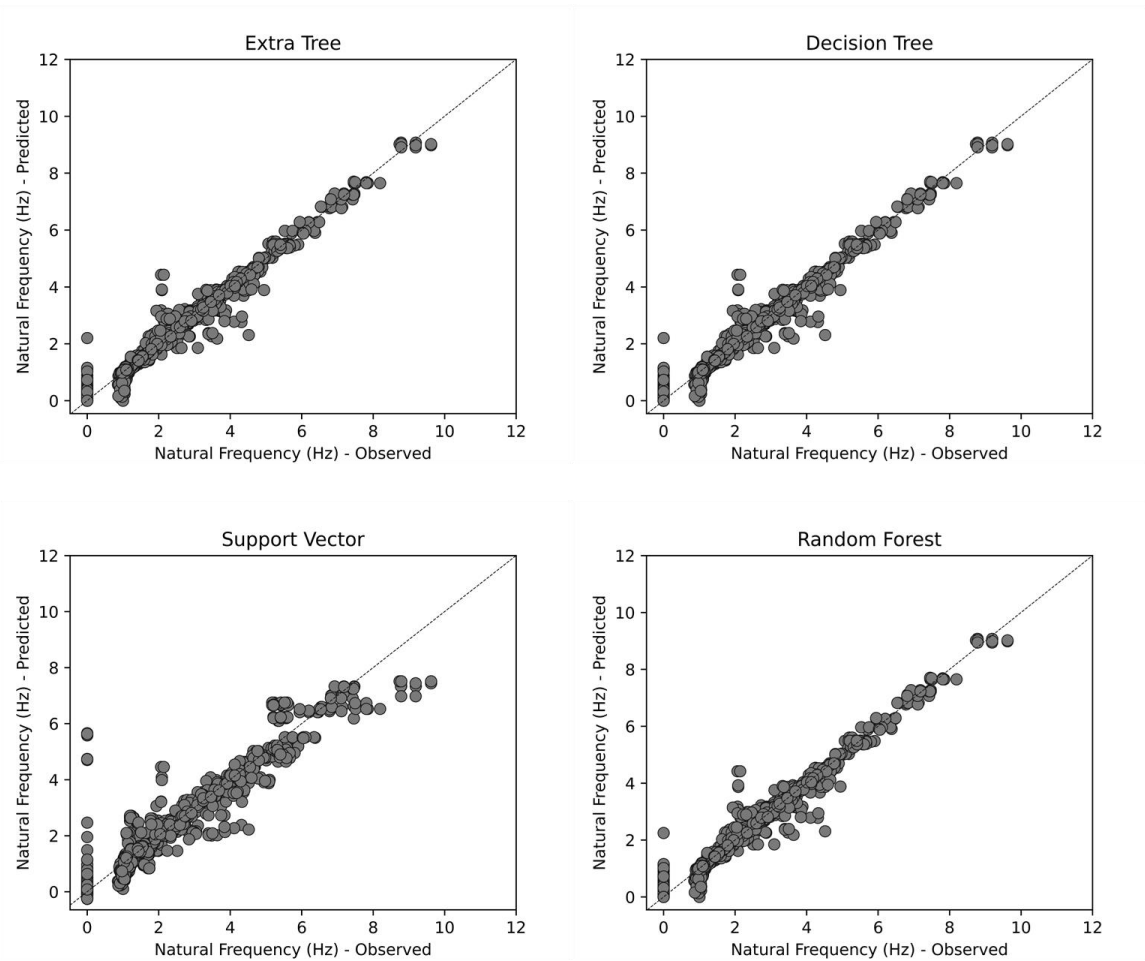
Figure 4-29: Scatter plot of ML models on prediction of cross-flow natural frequency in

multi-span.

Chapter 5:

Conclusions and recommendations for future studies

VIV fatigue performance of free-spanning pipelines was investigated by application of ML algorithms. The database was constructed by performing extensive case-studies using a set of FEA models developed in ABAQUS software. The model performance was verified against the DNV FATFREE data. Four different ML algorithms were employed to analyze the dataset. Main outcomes of this study are as follows:

- The machine learning algorithms was found to be an effective alternative solution for prediction of the VIV-induced fatigue life of multi-spanning pipelines. This approach will be particularly beneficial in the initial studies of pipeline engineering, where the cost effective experimental and numerical simulations are not conducted.

- It was observed that ML models based on Decision Tree Regression (DTR) have the best performance in modeling the dataset.

- Pipes of size No.16 and larger are more vulnerable against free-spanning and are potential for rapid failure.

- Higher width of the shoulder between two consecutive freespan can have positive impact in pipeline's performance against VIV fatigue loads.

- Pipes of size No.10, No.12, and No.14 have better performance against free-span configuration and the pipelines with pipe No.5 and No.6 experience the most severe

VIV stresses in both single-span and multi-span configurations and are more likely to have VIV fatigue failure.

- It was observed that the cross-flow induced in-line VIV stresses are generally stronger than cross-flow VIV and pure in-line stresses.

- Pure In-line stresses did not show significant impact on pipeline fatigue life.

- ML models based on DTR have great performance in modeling VIV related stresses and natural frequencies.

- ML models based on SVR are not suitable for modeling VIV related datasets.

Investigations shows that pipelines with pipe size No.5, No.6, and No.8 have the most vulnerability against VIV loads and risk of VIV fatigue failure is very high. Relative level of VIV stresses in in-line and cross-flow directions single-span configuration is presented in Figure 4-14 and Figure 4-25 shows the VIV stress levels for multi-span configuration.

5.1   Discussion on the rapid failure cases

VIV loads are mostly taken responsible for fatigue life deterioration, but this phenomenon is not the sole impact of span on pipeline's structure. In cases where span aspect ratio is too large and gap aspect ratio is too small, it is possible that during VIV vibrations, the VIV amplitude be larger than depth of gap. In such cases, a collision between pipe surface and seabed might occur. The collision might cause severe structural damages on pipeline such as buckling or tears on pipeline. In addition to this, in multi-spanning pipelines, there is significant intensity of stress on pipeline structure in shoulders. In cases where shoulder

is relatively narrow, concentrated forces might threaten the pipeline in shoulder specifically in both ends of shoulder where there are high gradients of deflections.

Rapid failure due to high stress over shoulder can only occur in multi-span cases. In general, stress of pipeline over shoulders is mainly governed by pipe characteristics and aspect ratio of span. The section of the pipeline laid over shoulder conveys large portion of the total gravitational force applied on free-spanning length of pipe. Therefor, higher width of shoulder will diminish the stress by expanding the total load over longer length. Pipe characteristics are also important factors for failure to occur or not. Pipelines with larger diameter of pipe will be heavier and also convey higher volume of fluids resulting increase in total weight per length of pipeline. Thickness of steel pipe is also important in pipeline's resistance against higher stresses. Higher thickness of pipe will help to improve pipe's strength.

All of the cases where the pipe is of size 18 with 18.00 x 0.500 in of diameter and wall thickness or larger pipes are subjected to immediate failure due to their high weight per length and relatively low pipe thickness. These pipelines are not recommended for projects where there are free-spanning ranges along pipeline installation path. Table 3-9 outlines list of main reasons for rapid failure of pipeline structure against free-spanning condition. There are three reasons mentioned in table as geometrical, weight, and shoulder. In cases with geometrical rapid failure, Amplitude of vibration is larger than 4x pipe diameter; therefore, pipeline touches seabed (not laid). In this research this type of collision is considered an immediate failure. Cases where the word "weight" mentioned as reason of failure, the pipe has large diameter and relatively small thickness. Large diameter pipes are

143

heavier, and the gravitational load deflects the pipelines. For pipes of sizes 5, 6, and 8, increased concentrated force in area laid over a narrow shoulder found to be main reason of rapid failure.

5.2   Recommendations for further studies

The following items are recommended to be considered in future studies:

- The current study has used numerical simulations to construct the database for training and testing of the ML algorithms. The numerical studies have inherited simplifications that may underplay some of the existing uncertainties. It is recommended to construct a database of existing experimental studies and verify the results using the test data. Further experimental would be beneficial to build a reliable dataset.

- Collision between pipeline and seabed might lead to a buckling damage on pipelines. It might be useful to study the buckling in pipeline due to VIV pipeline-seabed collision.

- There are different installation methods to lay offshore pipelines, studying efficiency, properties, post installation residual effects such as residual tension, and cost efficiency can pave the road to find optimum installation method to lay pipeline on severely uneven seabed where occurrence of multispanning is inevitable.

- The pipeline-soil interaction needs to be improved by incorporation of hysteretic non-linear models to capture the cyclic remoulding and penetration effects of the

pipeline. The performance of ML algorithms is suggested to be re-evaluated in presence of nonlinear hysteretic pipeline-seabed interaction.

- Incorporate the fluid-soil-pipeline interaction effects using the computational fluid dynamic (CFD) and coupled Eulerian-Lagrangian (CEL) methods.

- Pipeline behavior and also environmental parameters is shallow depth are different than deep waters, conducting research on pipelines installed in shallow depth might be a challenging but scientifically rewarding topic as in shallow waters some aqua related environmental parameters such as waves and temperature are in effect.

- It can be beneficial to extend this study to cover flexible pipelines which are largely in use for different purposes.

- In this study, seabed unevenness assumed to form one singlespan or a multispan consisting of two neighbouring spans. Studying more generalized set up of seabed configuration covering multispanning with more than two spans or freespanning length, where starting and ending edges of freespanning length have different elevations.

References

ABAQUS DOCUMENTATION. (n.d.). Choosing a beam element. ABAQUS. Retrieved October 19, 2022, from https://abaqus-docs.mit.edu/2017/English/SIMACAEELMRefMap/simaelm-c-beamelem.htm

Abeele, F.V., & Voorde, J.V. (2011). Stability of Offshore Pipelines in Close Proximity to the Seabed.

Achenbach, E. (1968). Distribution of local pressure and skin friction around a circular cylinder in cross-flow up to Re = 5×106. Journal of Fluid Mechanics, 34(4), 625-639. https://doi.org/10.1017/S0022112068002120

Achenbach, E., & Heinecke, E. (1981). On vortex shedding from smooth and rough cylinders in the range of Reynolds numbers 6×103 to 5×106. Journal of Fluid Mechanics, 109, 239-251. doi:10.1017/S002211208100102X

Anfinsen, K. A. (1995). Review of free spanning pipelines. Proceedings of the International Offshore and Polar Engineering Conference, 1995-June.

Aqilah Binti Abu Bakar, by, & Darul Ridzuan, P. (2014). Free Span Assessment of Offshore Pipeline by Using Finite Element Method. Universiti Teknologi PETRONAS.

Azimi, H., Shiri, H., & Mahdianpari, M. (2022a). Iceberg-seabed interaction analysis in sand by a random forest algorithm. Polar Science,34, Article 100902. https://doi.org/10.1016/J.POLAR.2022.100902

Azimi, H., Shiri, H., & Mahdianpari, M. (2022b). Iceberg-seabed interaction evaluation in clay seabed using tree-based machine learning algorithms. Journal of Pipeline Science and Engineering, 2(4), 100075. https://doi.org/10.1016/J.JPSE.2022.100075

Azimi, H., Shiri, H., & Mahdianpari, M. (2022c). Iceberg-seabed interaction evaluation in clay seabed using tree-based machine learning algorithms. Journal of Pipeline Science and Engineering, 2(4), 100075. https://doi.org/10.1016/J.JPSE.2022.100075

Bai, Q., & Bai, Y. (2014). Subsea Pipeline Design, Analysis, and Installation. In Subsea Pipeline Design, Analysis, and Installation. Elsevier Inc. https://doi.org/10.1016/C2010-0-67706-6

Bai, X.-D., & Zhang, W. (2022). Machine learning for vortex induced vibration in turbulent flow. Computers & Fluids, 235, 105266. https://doi.org/10.1016/j.compfluid.2021.105266

Bai, Y., Tang, J., Xu, W., & Ruan, W. (2015). Reliability-based design of subsea light weight pipeline against lateral stability. Marine Structures, 43, 107–124. https://doi.org/10.1016/j.marstruc.2015.06.002

Bearman, P. W. (1978). Flow-Induced Vibration. By R OBERT D. B LEVINS. Van Nostrand Reinhold, 1977. 363 pp. £13. 75.. Journal of Fluid Mechanics, 89(1). https://doi.org/10.1017/s0022112078232545

Bearman, P., & Zdravkovich, M. (1978). Flow around a circular cylinder near a plane boundary. Journal of Fluid Mechanics, 89(1), 33-47. doi:10.1017/S002211207800244X

Bishop, R. E. D., & Hassan A Y. (1964). The lift and drag forces on a circular cylinder
oscillating in a flowing fluid. Proceedings of the Royal Society of London. Series A.
Mathematical and Physical Sciences, 277(1368).
https://doi.org/10.1098/rspa.1964.0005

Blevin, R. D. (1990). Flow-Induced Vibrations.

Buurguet, R., Karniadakis, G., & Triantafyllou, M. (2011). Vortex-induced vibrations of
a long flexible cylinder in shear flow. Journal of Fluid Mechanics, 677, 342-382.
doi:10.1017/jfm.2011.90

Breiman, L. (2001). Random Forests. Machine Learning 2001 45:1, 45(1), 5–32.
https://doi.org/10.1023/A:1010933404324

Bryndum, M. B., & Smed, P. F. (1998). Application of the generalised force model for
VIV in pipeline span design. Proceedings of the International Conference on
Offshore Mechanics and Arctic Engineering – OMAE98-1053.

Cann, M., McConkey, R., Lien, F.-S., Melek, W., & Yee, E. (2021). Mode classification
for vortex shedding from an oscillating wind turbine using machine learning. Journal
of Physics: Conference Series, 2141(1), 012009. https://doi.org/10.1088/1742-
6596/2141/1/012009

Chen, C., Li, C., Reniers, G., & Yang, F. (2021). Safety and security of oil and gas
pipeline transportation: A systematic analysis of research trends and future needs
using WoS. Journal of Cleaner Production, 279, Article 123583.
https://doi.org/10.1016/j.jclepro.2020.123583

Choi, H., Jeon, W. P., & Kim, J. (2008). Control of flow over a bluff body. In Annual
Review of Fluid Mechanics, 40(1), 113-139.
https://doi.org/10.1146/annurev.fluid.39.050905.110149

Choi, H. S. (2001). Free spanning analysis of offshore pipelines. Ocean Engineering,
28(10), 1325-1338. https://doi.org/10.1016/S0029-8018(00)00071-8

D.Blevin, R. (2001). Flow-Induced Vibrations (2nd ed.). Krieger Publishing.

DET NORSKE VERITAS. (2006). dnv-rp-f105 freespanning pipelines recommended
practice (p. 2).In DNV.

DET NORSKE VERITAS. (2021). Dnvgl-rp-f105 freespanning pipelines. In DNV.

Det Norske Veritas Germanischer Lloyd (DNV GL). (2017). Recommended practice
DNVGL-RP-F114: Pipe-soil interaction for submarine pipelines. Dnvgl-Rp-F114,
May.

DNV. (2012). det norske veritas tm report fatigue calculations for existing gulf of mexico
fixed structures for. https://www.bsee.gov/sites/bsee.gov/files/tap-technical-
assessment-program//675aa.pdf

DNV GL. (2016). DNVGL-RP-C203: Fatigue design of offshore steel structures The.
DNV GL - Recommended Practice, April.

DNV GL Group. (2016). DNVGL-RP-C203: Recommended practice - Fatigue design of
offshore steel structures. January.

DNV RP F105. (2006). DNV-RP-F105: Free Spanning Pipelines. Dnv Rp F105, 163(February).

Elbanhawy, A. (2011). On Numerical Investigations of Flow-Induced Vibration and Heat Transfer for Flow Around Cylinders [Doctoral dissertation - The University of Manchester].

Facchinetti, M. L., de Langre, E., & Biolley, F. (2004). Coupling of structure and wake oscillators in vortex-induced vibrations. Journal of Fluids and Structures, 19(2), 123–140. https://doi.org/10.1016/J.JFLUIDSTRUCTS.2003.12.004

Farshidianfar, A., & Zanganeh, H. (2010). A modified wake oscillator model for vortex-induced vibration of circular cylinders for a wide range of mass-damping ratio. Journal of Fluids and Structures, 26(3), 430–441. https://doi.org/10.1016/J.JFLUIDSTRUCTS.2009.11.005

Finnemore, E. J., & Franzini, J. B. (2002). Fluid mechanics with engineering applications (10th Edition). John Finnemore y Joseph B. Franzini. McGraw Hill. https://www.accessengineeringlibrary.com/content/book/9780072432022

Fu, B., Zou, L., & Wan, D. (2018). Numerical study of vortex-induced vibrations of a flexible cylinder in an oscillatory flow. Journal of Fluids and Structures, 77,170-181. https://doi.org/10.1016/j.jfluidstructs.2017.12.006

Furnes, G. K., & Berntsen, J. (2003). On the response of a free span pipeline subjected to ocean currents. Ocean Engineering, 30(12), 1553-1577. https://doi.org/10.1016/S0029-8018(02)00138-5

Fyrileiv, O., Mørk, K., & Chezhian, M. (2005). Experiences using DNV-RP-F105 in assessment of free spanning pipelines. Proceedings of the International Conference on Offshore Mechanics and Arctic Engineering - OMAE, 3. https://doi.org/10.1115/OMAE2005-67453

Gabbai, R. D., & Benaroya, H. (2005). An overview of modeling and experiments of vortex-induced vibration of circular cylinders. Journal of Sound and Vibration, 282(3–5), 575–616. https://doi.org/10.1016/J.JSV.2004.04.017

Geurts, P., Ernst, D., & Wehenkel, L. (2006). Extremely randomized trees. Machine Learning 2006 63:1, 63(1), 3–42. https://doi.org/10.1007/S10994-006-6226-1

Green, K. P., & Jackson, T. (2015). Safety in the Transportation of Oil and Gas: Pipelines or Rail?. Fraser Institute.

Gu, S., Wang, J., Hu, G., Lin, P., Zhang, C., Tang, L., & Xu, F. (2021). Prediction of wind-induced vibrations of twin circular cylinders based on machine learning. Ocean Engineering, 239, 109868. https://doi.org/10.1016/j.oceaneng.2021.109868

Hameed, M. M., Alomar, M. K., Khaleel, F., & Al-Ansari, N. (2021). An Extra Tree Regression Model for Discharge Coefficient Prediction: Novel, Practical Applications in the Hydraulic Sector and Future Research Directions. Mathematical Problems in Engineering, 2021, Article 7001710. https://doi.org/10.1155/2021/7001710

Hiramoto, R., & Higuchi, H. (2003). Vortex shedding behind a nonparallel pair of

circular cylinders. Journal of Fluids and Structures, 18(1),131-143.

https://doi.org/10.1016/S0889-9746(03)00089-6

Hirdaris, S. E., Bai, W., Dessi, D., Ergin, A., Gu, X., Hermundstad, O. A., Huijsmans, R.,

Iijima, K., Nielsen, U. D., Parunov, J., Fonseca, N., Papanikolaou, A., Argyriadis,

K., & Incecik, A. (2014). Loads for use in the design of ships and offshore

structures. In Ocean Engineering, 78, 131-174.

https://doi.org/10.1016/j.oceaneng.2013.09.012

Jo, C. H., Lee, S. B., Shin, Y. S., Hong, S. G., & Min, K. H. (2002). Numerical and

Experimental Study of Offshore Pipeline Stability in Trench. Journal of Waterway,

Port, Coastal, and Ocean Engineering, 128(6), 258-270.

https://doi.org/10.1061/(asce)0733-950x(2002)128:6(258)

Journee, J. M. J., & Massie, W. W. (2001). Offshore Hydrodynamics, First Edition. In

Delft University of Technology.

Rakhmat Kabul, E., & Madiistriyatno, H. (2021). Evaluation of implementation of health,

safety and environment (hse) program in oil and gas transportation company (in the

human resource management approach). Dinasti International Journal of

Management Science, 2(3), 360-370. https://doi.org/10.31933/dijms.v2i3.696

Kaneko, S. (Shigehiko), Nakamura, T. (Tomomichi), Inada, F., Kato, M. (Engineer),

Ishihara, K., Nishihara, T., Mureithi, N. W., & Langthjem, M. A. (2014). Flow-

induced vibrations: classifications and lessons from practical experiences. Elsevier.

Kármán, Th. von. (2012). Ueber den Mechanismus des Widerstandes, den ein bewegter Körper in einer Flüssigkeit erfährt. Nachrichten von Der Gesellschaft Der Wissenschaften Zu Göttingen, Mathematisch-Physikalische Klasse, 1911, 509–517.

Kenny, J. P. (1993). Structural analysis of pipeline spans. In Health and Safety Executive (HSE).

Keprate, A., & Ratnayake, R. M. C. (2016). Enhancing offshore process safety by selecting fatigue critical piping locations for inspection using Fuzzy-AHP based approach. Process Safety and Environmental Protection, 102, 71-84. https://doi.org/10.1016/j.psep.2016.02.013

Khalak, A., & Williamson, C. H. K. (1999). motions, forces and mode transitions in vortex-induced vibrations at low mass-damping. Journal of Fluids and Structures, 13(7–8), 813–851. https://doi.org/10.1006/JFLS.1999.0236

Knoll, D. A., & Herbich, J. B. (1980). Wave and current forces on a submerged offshore pipeline. Proceedings of the Annual Offshore Technology Conference, 1980-May. https://doi.org/10.4043/3762-ms

Krenk, S., & Nielsen, S. R. K. (1999). Energy Balanced Double Oscillator Model for Vortex-Induced Vibrations. Journal of Engineering Mechanics, 125(3), 263-271. https://doi.org/10.1061/(asce)0733-9399(1999)125:3(263)

Kurushina, V., & Pavlovskaia, E. (2017). Wake oscillator equations in modelling vortex-induced vibrations at low mass ratios. OCEANS 2017 - Aberdeen, 2017-October. https://doi.org/10.1109/OCEANSE.2017.8084644

Li, S., Laima, S., & Li, H. (2018). Data-driven modeling of vortex-induced vibration of a
long-span suspension bridge using decision tree learning and support vector
regression. Journal of Wind Engineering and Industrial Aerodynamics, 172, 196–
211. https://doi.org/10.1016/j.jweia.2017.10.022

Liang, D., Cheng, L., & Li, F. (2005). Numerical modeling of flow and scour below a
pipeline in currents. Part II. Scour simulation. Coastal Engineering, 52(1), 43-62.
https://doi.org/10.1016/j.coastaleng.2004.09.001

Lin, W.-J., Lin, C., Hsieh, S.-C., & Dey, S. (2009). Flow Characteristics around a
Circular Cylinder Placed Horizontally above a Plane Boundary. Journal of
Engineering Mechanics, 135(7), 697-716.
https://doi.org/10.1061/(asce)0733-9399(2009)135:7(697)

Ma, L., Resvanis, T. L., & Vandiver, J. K. (2020, August 3). Using Machine Learning to
Identify Important Parameters for Flow-Induced Vibration. Volume 4: Pipelines,
Risers, and Subsea Systems. https://doi.org/10.1115/OMAE2020-18325

Marhavilas, P. K., Filippidis, M., Koulinas, G. K., & Koulouriotis, D. E. (2021). Safety
Considerations by Synergy of HAZOP/DMRA with Safety Color Maps—
Applications on: A Crude-Oil Processing Industry/a Gas Transportation
System. Processes, 9(8), 1299. MDPI AG. Retrieved from
http://dx.doi.org/10.3390/pr9081299

Mei, Y.-F., Zheng, C., Aubry, N., Li, M.-G., Wu, W.-T., & Liu, X. (2021). Active control
for enhancing vortex induced vibration of a circular cylinder based on deep

reinforcement learning. Physics of Fluids, 33(10), 103604.

https://doi.org/10.1063/5.0063988

Mode, G., Holden, K., & Yttervoll, P. O. (1994). Motion of spring supported cylinders in

subcritical and critical water flows (Conference) | OSTI.GOV. U.S. Department of

Energy, Office of Scientific and Technical Information (OSTI).

https://www.osti.gov/biblio/404222

Moe, G., & Wu, Z. J. (1990). The Lift Force on a Cylinder Vibrating in a Current.

Journal of Offshore Mechanics and Arctic Engineering, 112(4), 297–303.

https://doi.org/10.1115/1.2919870

Mohaddes Pour, M., Razavi Taheri, S. S., & Amirhosein Moniri Abyaneh. (2021). Free

Span Analysis for Submarine Pipelines. In Shock and Vibration (Vol. 2021).

https://doi.org/10.1155/2021/9305129

Morison, J. R., Johnson, J. W., & Schaaf, S. A. (1950). The Force Exerted by Surface

Waves on Piles. Journal of Petroleum Technology, 2(05).

https://doi.org/10.2118/950149-g

Mureithi, N. W., Kanki, H., & Nakamura, T. (2000). Bifurcation and perturbation

analysis of some vortex shedding models. Proceedings of the 7th International

Conference on Flow-Induced Vibrations. https: ://doi.org/10.1088/1742-

6596/64/1/012015

Nair, A. (2020, December 13). DNV GL Pipeline Day 2016. DNV GL.

    https://www.dnvgl.us/training/welcome-to-dnv-gl-pipeline-day-2016-day-1-

    offshore-75501

Ole-Erik Vestøl Endrerud. (2013). Parameter Study of the Effect of Boulders on Pipeline

    Free Span Sections [Master's thesis, University of Stavanger-Norway].

    Studentoppgaver (TN-IKM / TN-IMBM). http://hdl.handle.net/11250/183032

Ooi, C. S., Lim, M. H., Lee, K. Q., Kang, H. S., & Leong, M. S. (2020). System

    Identification of Helical Strakes Suppressed Vortex-induced Vibration for Flexible

    Pipes. Pertanika Journal of Science & Technology, 28(2), 493-508.

Pantazopoulos, M. S., Crossley, C. W., Orgill, G., & Lambrakos, K. F. (1993). Fourier

    methodology for pipeline span vortex-induced vibration analysis in combined flow.

    Proceedings of the International Conference on Offshore Mechanics and Arctic

    Engineering - OMAE, 5.

Paterson, E. G. Approximate solutions of navier-stokes equations, Spring 2005.

Pereira, A., Bomfimsilva, C., Franco, L., Tardelli, L., & Eigbe, U. (2008). In-Place Free

    Span Assessment Using Finite Element Analysis. Volume 3: Pipeline and Riser

    Technology; Ocean Space Utilization, 191–196.

    https://doi.org/10.1115/OMAE2008-57272

Plaschko, P. (2000). Global chaos in flow-induced oscillations of cylinders. Journal of

    Fluids and Structures, 14(6), 883–893. https://doi.org/10.1006/JFLS.2000.0298

Price, S. J., Sumner, D., Smith, J. G., Leong, K., & Païdoussis, M. P. (2002). Flow visualization around a circular cylinder near to a plane wall. Journal of Fluids and Structures, 16(2). https://doi.org/10.1006/jfls.2001.0413

Rao, S., & Yap, F. (2011). Mechanical vibrations (5th ed. in SI units ed.). In Singapore: Prentice Hall.

Rashidi, S., Hayatdavoodi, M., & Esfahani, J. A. (2016). Vortex shedding suppression and wake control: A review. In Ocean Engineering, (126). https://doi.org/10.1016/j.oceaneng.2016.08.031

Reid, A., Grytten, T. I., & Nystrom, P. R. (2000). Case studies in pipeline free span fatigue. Proceedings of the International Offshore and Polar Engineering Conference, 3.

Riemer-Sørensen, S., Wu, J., Lie, H., Sævik, S., & Kim, S. W. (2019). Data-driven prediction of vortex-induced vibration response of marine risers subjected to three-dimensional current. Communications in Computer and Information Science, 1056, 78-89. https://doi.org/10.1007/978-3-030-35664-4_8

Rishal Hurbans. (2020). grokking artificial intelligence algorithms. In Manning Publications.

Ronold, K. O. (1995). A probabilistic approach to the lengths of free pipeline spans. Applied Ocean Research, 17(4), 225-232. https://doi.org/10.1016/0141-1187(95)00015-1

safety4sea. (2019, December 3). Case study: Mooring line failure onboard - SAFETY4SEA. https://safety4sea.com/cm-case-study-mooring-line-failure-onboard/

Sahani, N., & Ghosh, T. (2021). GIS-based spatial prediction of recreational trail susceptibility in protected area of Sikkim Himalaya using logistic regression, decision tree and random forest model. Ecological Informatics, 64, 101352. https://doi.org/10.1016/J.ECOINF.2021.101352

Saheed Adekunle Shittu. (2022). Numerical simulation of vortexinduced vibration of free spanning underwater pipeline close to the seabed. In University of Manchester.

Salehi, M. A., Mazaheri, S., & Kazeminezhad, M. H. (2018). Study of Flow Characteristics around a Near-Wall Circular Cylinder Subjected to a Steady Cross-Flow. International journal of coastal & offshore engineering, 1(4), . https: 10.29252/ijcoe.1.4.45

Sarpkaya, T. (2004). A critical review of the intrinsic nature of vortex-induced vibrations. Journal of Fluids and Structures, 19(4), 389-447. https://doi.org/10.1016/j.jfluidstructs.2004.02.005

Schewe, G. (1983). On the force fluctuations acting on a circular cylinder in crossflow from subcritical up to transcritical Reynolds numbers. Journal of Fluid Mechanics, 133, 265-285. https://doi.org/10.1017/S0022112083001913

Skaugset, K. Bjørn. (2003). On the suppression of vortex induced vibrations of circular cylinders by radial water jets [Norwegian University of Science and Technology

(NTNU)]. In XVI, 227, 6 s. ill. https://ntnuopen.ntnu.no/ntnu-xmlui/handle/11250/229076

Song, J. N., Lu, L., Teng, B., Park, H. il, Tang, G. Q., & Wu, H. (2011). Laboratory tests of vortex-induced vibrations of a long flexible riser pipe subjected to uniform flow. Ocean Engineering, 38(11–12). https://doi.org/10.1016/j.oceaneng.2011.05.020

Song, X., & Wang, S. (2019). A novel spectral moments equivalence based lumping block method for efficient estimation of offshore structural fatigue damage. International Journal of Fatigue, 118. https://doi.org/10.1016/j.ijfatigue.2018.09.016

Søreide, T., Paulsen, G., & Nielsen, F. G. (2001). Parameter study of long free spans. Proceedings of the International Offshore and Polar Engineering Conference, 2.

Sumer, B. M., & Fredsøe, J. (1990). Scour below pipelines in waves. Journal of Waterway, Port, Coastal, and Ocean Engineering, 116(3), 307-323. https://doi.org/10.1061/(asce)0733-950x(1990)116:3(307)

Sumer, B. M., & Fredsøe, J. (2006). Hydrodynamics around cylindrical structures (revised edition). In world scientific. https://doi.org/10.1142/6248

Vapnik, V. N. (1995). The Nature of Statistical Learning Theory - Vladimir Vapnik - Google Books. In M. Jordan & S. L. Lauritzen (Eds.), Springer (Second). Springer.

Williamson, C. H. K. (1988). The existence of two stages in the transition to three-dimensionality of a cylinder wake. Physics of Fluids, 31(11), 3165–3168. https://doi.org/10.1063/1.866925

Williamson, C. H. K., & Jauvtis, N. (2004). A high-amplitude 2T mode of vortex-induced vibration for a light body in XY motion. European Journal of Mechanics - B/Fluids, 23(1), 107–114. https://doi.org/10.1016/J.EUROMECHFLU.2003.09.008

Yang, B., Gao, F., Jeng, D. S., & Wu, Y. (2009). Experimental study of vortex-induced vibrations of a cylinder near a rigid plane boundary in steady flow. Acta Mechanica Sinica/Lixue Xuebao, 25(1), 51-63. https://doi.org/10.1007/s10409-008-0221-7

Yang, J., Low, Y. M., Lee, C. H., & Chiew, Y. M. (2018). Numerical simulation of scour around a submarine pipeline using computational fluid dynamics and discrete element method. Applied Mathematical Modelling, 55, 400-416. https://doi.org/10.1016/j.apm.2017.10.007

Yang, J., Wu, X., & Wang, Q. (2012). Channel parameter estimation for scatter cluster model using modified MUSIC algorithm. International Journal of Antennas and Propagation, 2012, Article 619817. https://doi.org/10.1155/2012/619817

Yang, R., Gao, F. P., Wu, Y. X., & Li, D. H. (2006). Experimental study on vortex-induced vibrations of submarine pipeline near seabed boundary in ocean currents. China Ocean Engineering, 20(1),113-121.

Zang, Z., Chen, Y., Zhang, J., Tian, Y., & Esteban, M. D. (2021). Experimental study on local scour and onset of VIV of a pipeline on a silty seabed under steady currents. Applied Ocean Research, 109, 102560. https://doi.org/10.1016/j.apor.2021.102560

Zhang, X., Thompson, D., & Sheng, X. (2020a). Differences between Euler-Bernoulli and Timoshenko beam formulations for calculating the effects of moving loads on a

periodically supported beam. Journal of Sound and Vibration, 481, 115432.

https://doi.org/10.1016/J.JSV.2020.115432

Zhang, X., Thompson, D., & Sheng, X. (2020b). Differences between Euler-Bernoulli

and Timoshenko beam formulations for calculating the effects of moving loads on a

periodically supported beam. Journal of Sound and Vibration, 481, 115432.

https://doi.org/10.1016/J.JSV.2020.115432

Appendix A:

Stress profile of pipeline due to deflections in natural mode shapes

In this Appendix, stress profile of pipeline under first in-line and cross flow mode shapes are presented. For multi-spanning cases, series have been noted in abbreviated format where OD stands for pipe size, LD stands for span aspect ratio, R is the relative span aspect ratio, and the #X is presenting length of shoulder. A profile with 1x in it means that length of shoulder in model equals 1x of outer diameter of the pipe and similarly, kX means the length of shoulder is k times the outer diameter of the pipe in the configuration.

Cross-flow mode stress profiles for single-span configuration.
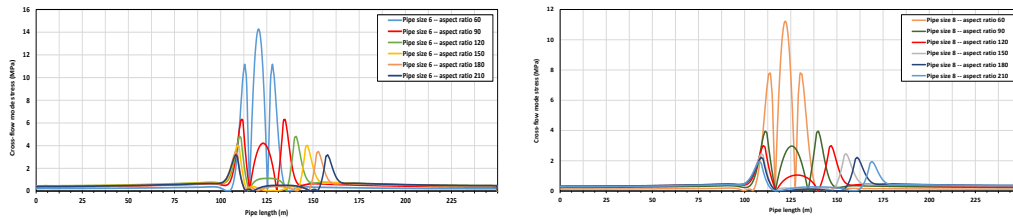
Figure A- 1: Single-span cross-flow mode stress profile 1.
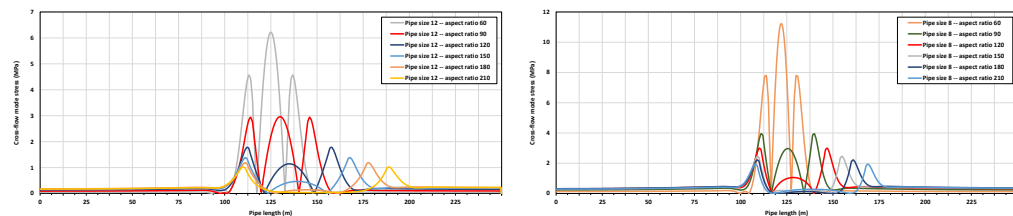
Figure A- 2: Single-span cross-flow mode stress profile 2.
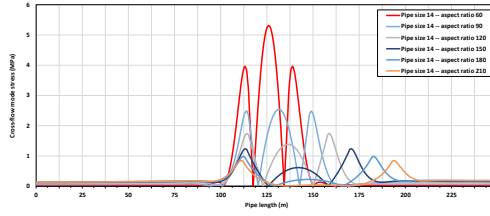
Figure A- 3: Single-span cross-flow mode stress profile 3.

In-line mode stress profiles for single-span configuration.
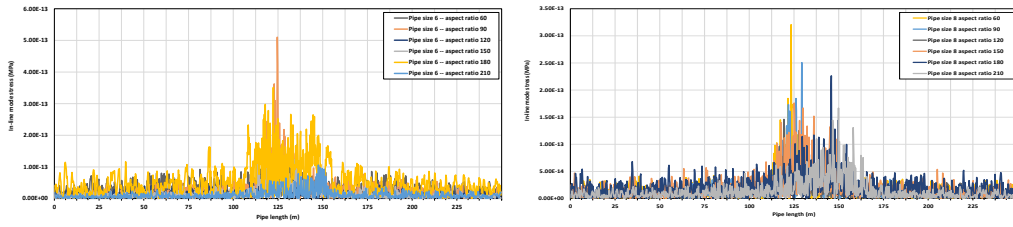
Figure A- 4: Single-span in-line mode stress profile 1.
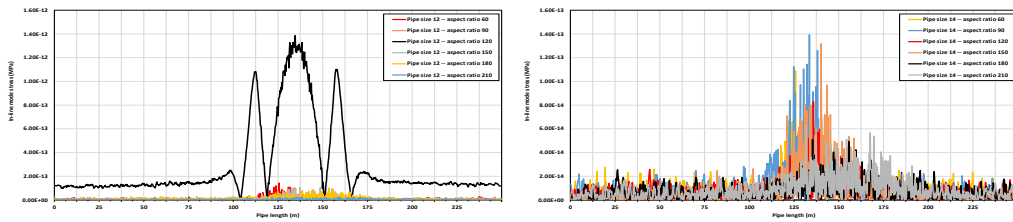
Figure A- 5: Single-span in-line mode stress profile 2.

# Cross-flow mode stress profiles for multi-span configuration.
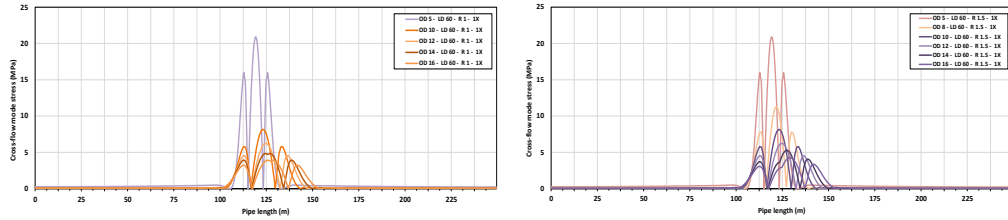
Figure A- 6: Multi-span cross-flow mode stress profile 1.
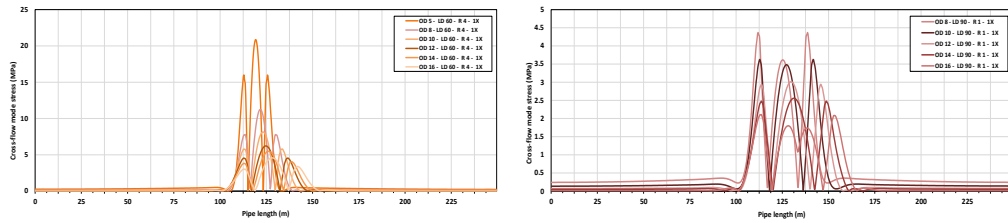
Figure A- 7: Multi-span cross-flow mode stress profile 2.
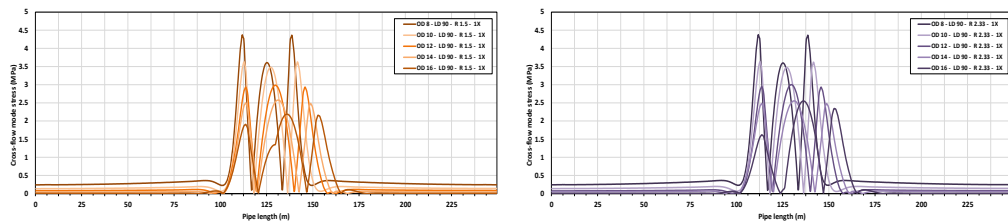
Figure A- 8: Multi-span cross-flow mode stress profile 3.
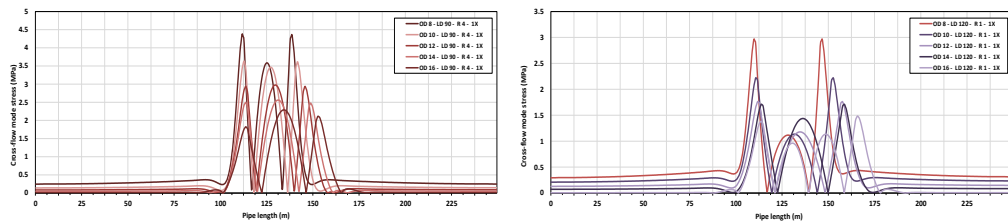
Figure A- 9: Multi-span cross-flow mode stress profile 4.
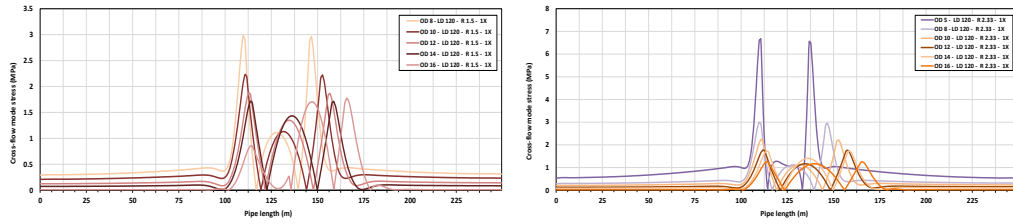
Figure A- 10: Multi-span cross-flow mode stress profile 5.
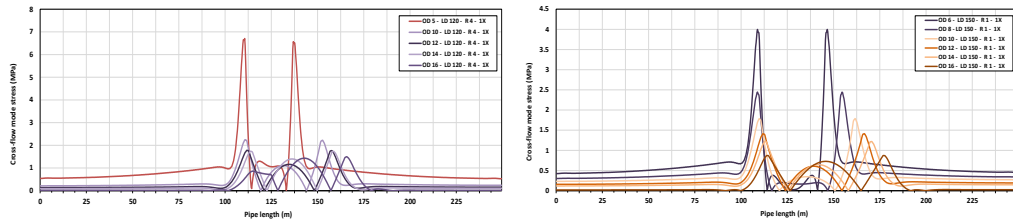
Figure A- 11: Multi-span cross-flow mode stress profile 6.
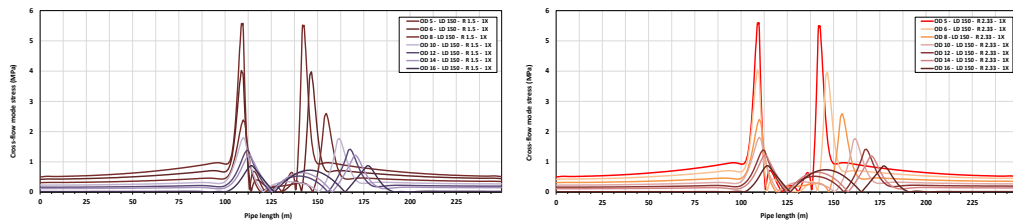
Figure A- 12: Multi-span cross-flow mode stress profile 7.
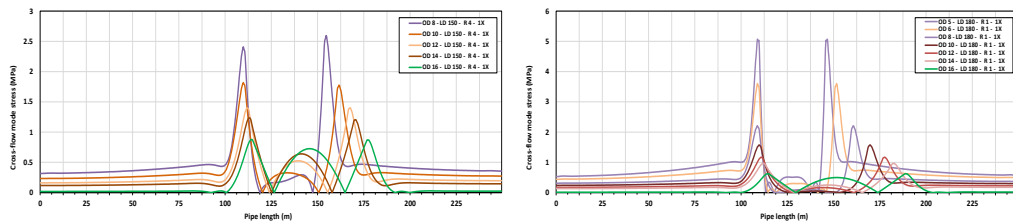
Figure A- 13: Multi-span cross-flow mode stress profile 8.
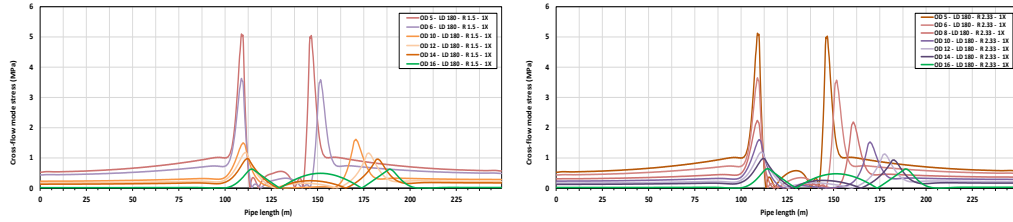
Figure A- 14: Multi-span cross-flow mode stress profile 9.
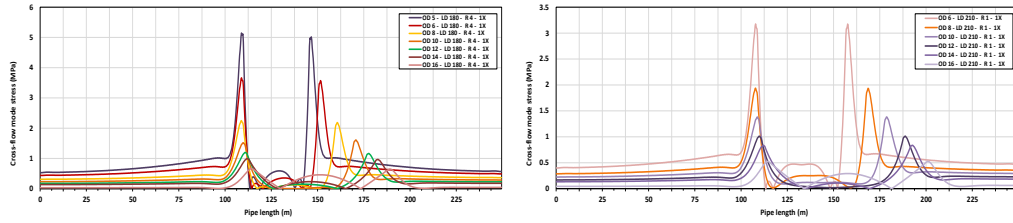
Figure A- 15: Multi-span cross-flow mode stress profile 10.
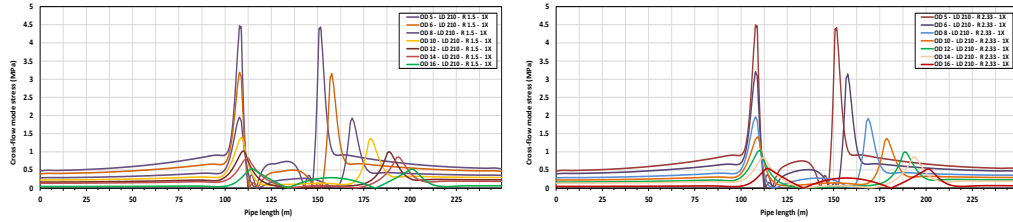
Figure A- 16: Multi-span cross-flow mode stress profile 11.
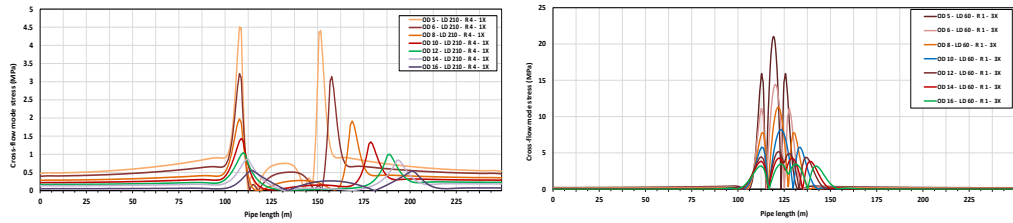
Figure A- 17: Multi-span cross-flow mode stress profile 12.
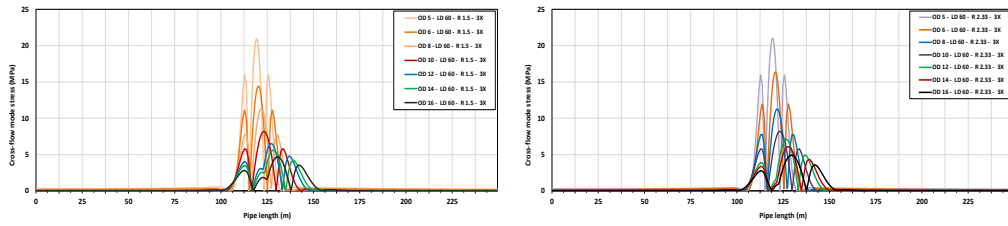
Figure A- 18: Multi-span cross-flow mode stress profile 13.
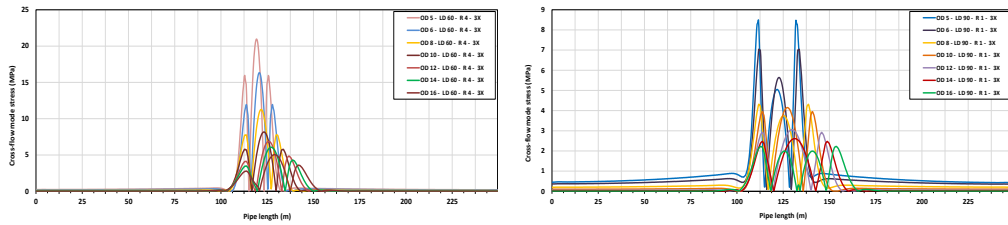
Figure A- 19: Multi-span cross-flow mode stress profile 14.
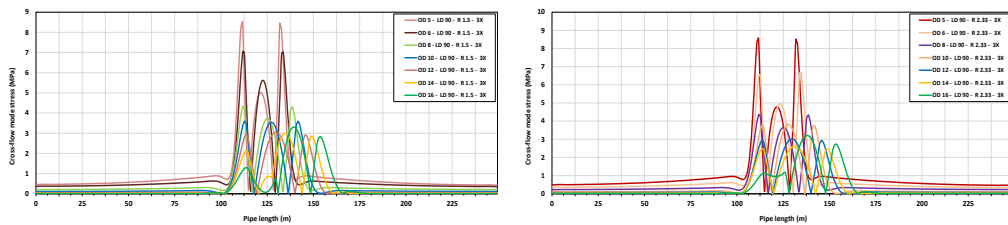
Figure A- 20: Multi-span cross-flow mode stress profile 15.
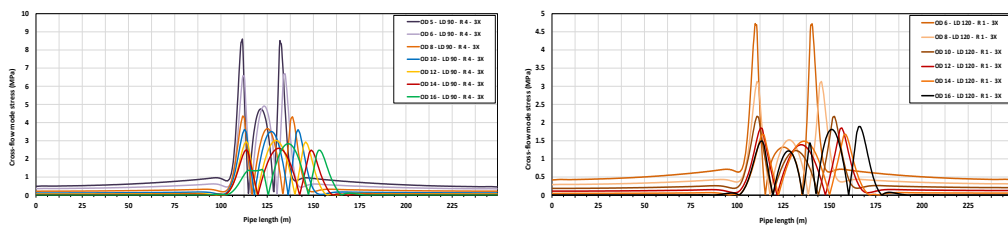
Figure A- 21: Multi-span cross-flow mode stress profile 16.
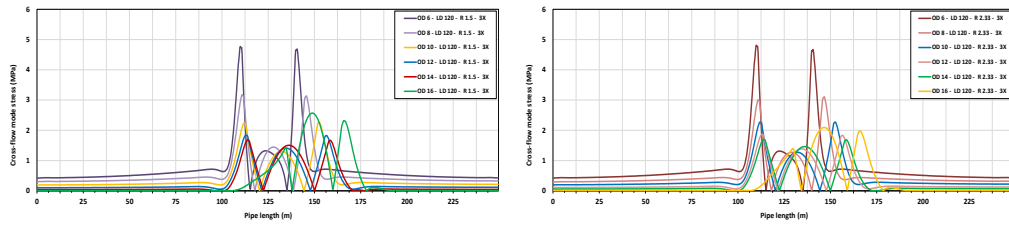
Figure A- 22: Multi-span cross-flow mode stress profile 17.
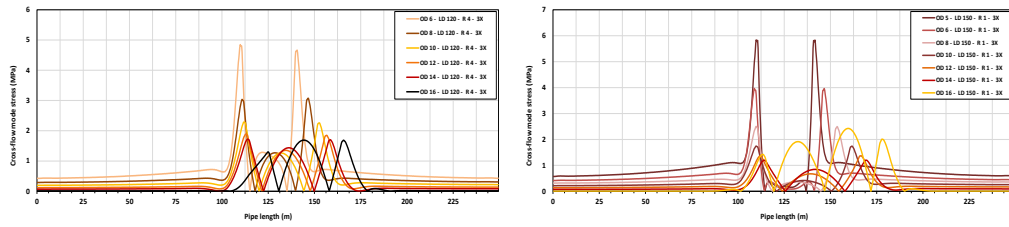
Figure A- 23: Multi-span cross-flow mode stress profile 18.
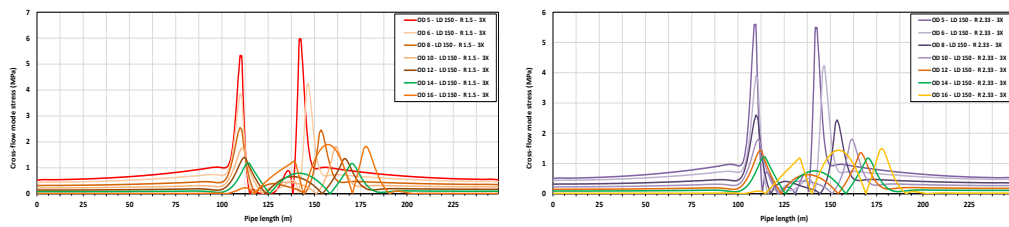
Figure A- 24: Multi-span cross-flow mode stress profile 19.
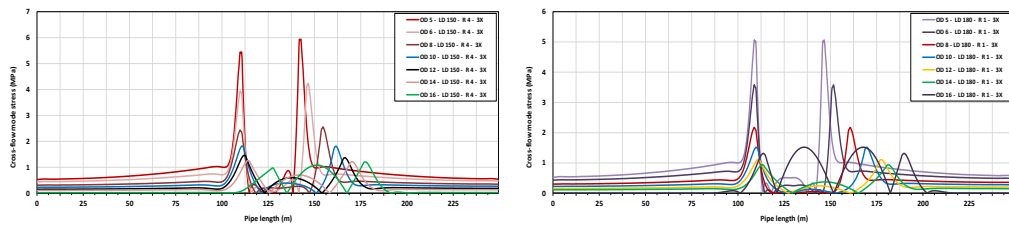
Figure A- 25: Multi-span cross-flow mode stress profile 20.

168
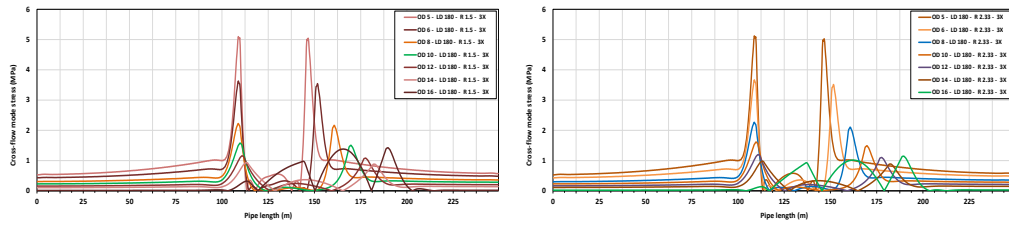
Figure A- 26: Multi-span cross-flow mode stress profile 21.
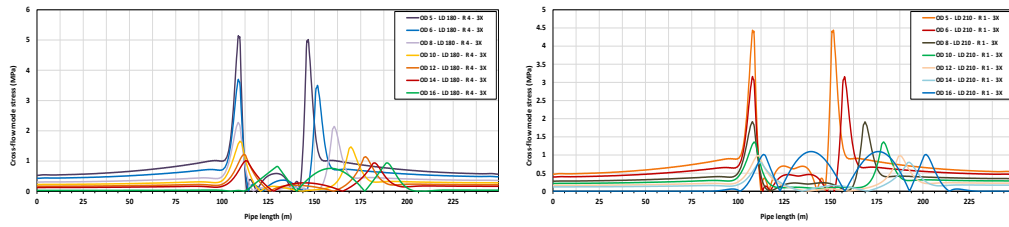
Figure A- 27: Multi-span cross-flow mode stress profile 22.
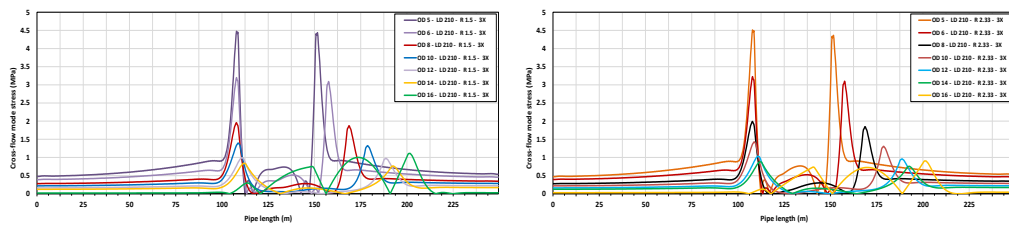
Figure A- 28: Multi-span cross-flow mode stress profile 23.
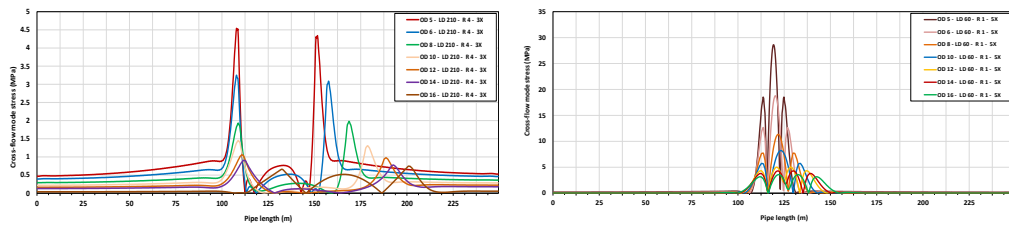
Figure A- 29: Multi-span cross-flow mode stress profile 24.
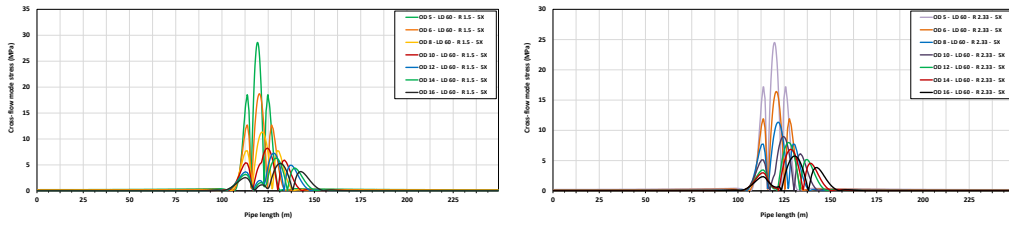
Figure A- 30: Multi-span cross-flow mode stress profile 25.
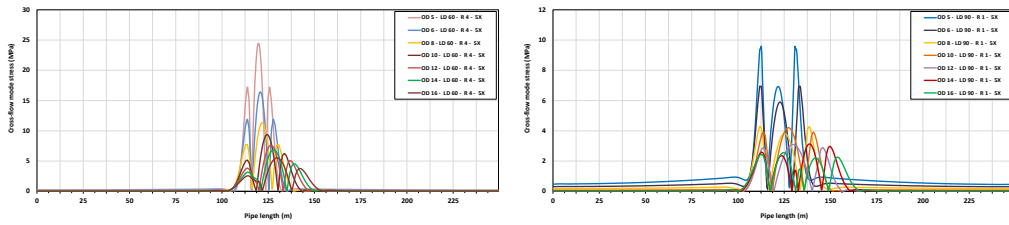
Figure A- 31: Multi-span cross-flow mode stress profile 26.
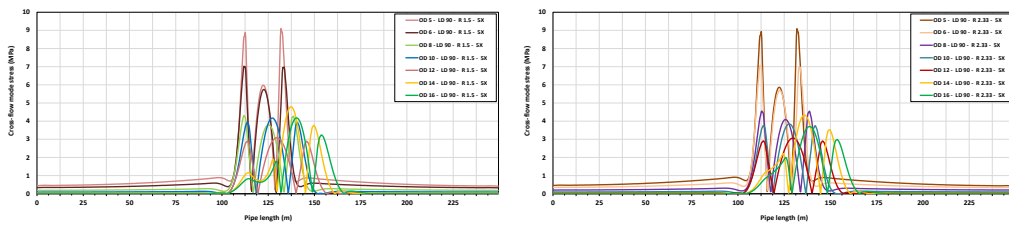
Figure A- 32: Multi-span cross-flow mode stress profile 27.
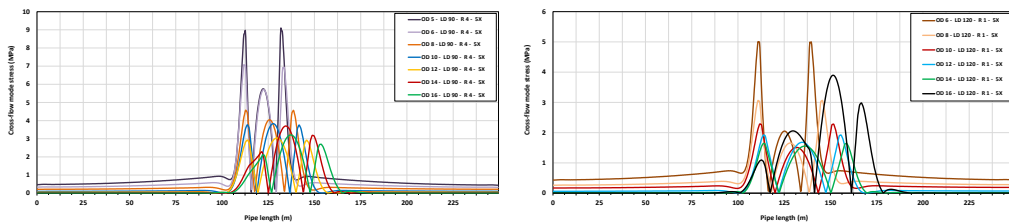
Figure A- 33: Multi-span cross-flow mode stress profile 28.
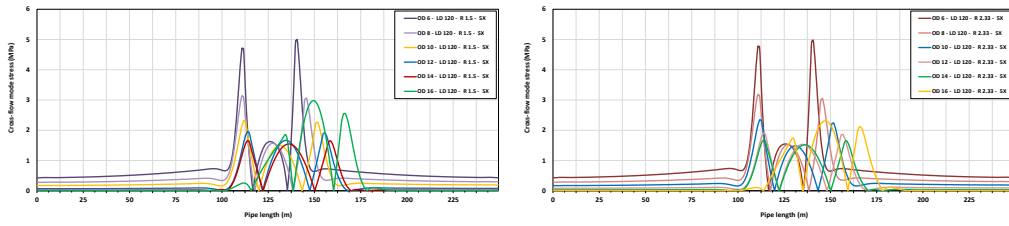
Figure A- 34: Multi-span cross-flow mode stress profile 29.
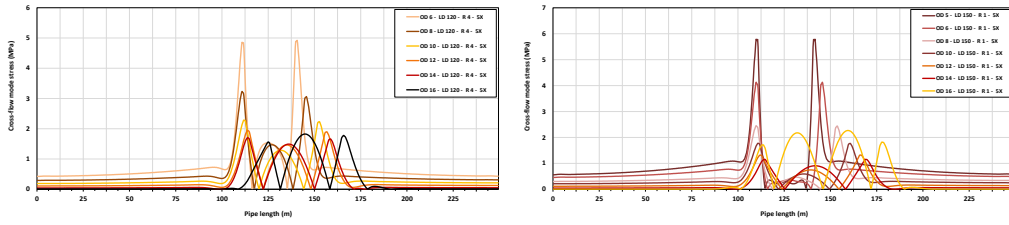
Figure A- 35: Multi-span cross-flow mode stress profile 30.
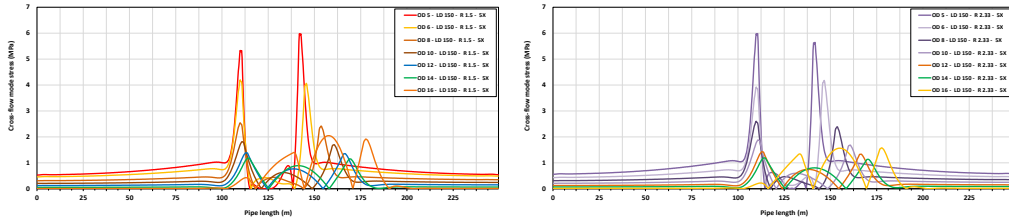
Figure A- 36: Multi-span cross-flow mode stress profile 31.
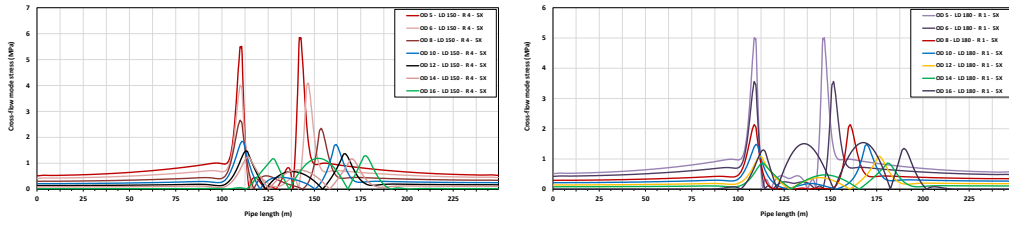
Figure A- 37: Multi-span cross-flow mode stress profile 32.
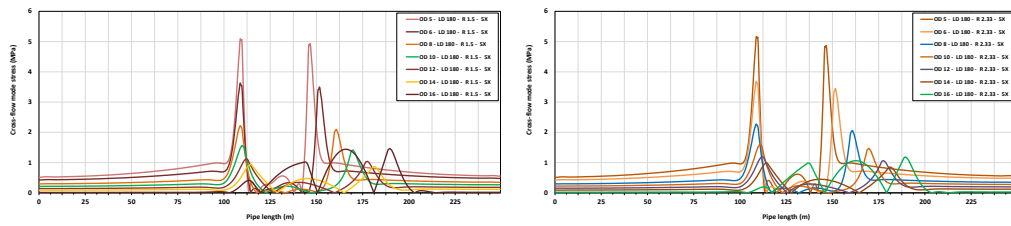
Figure A- 38: Multi-span cross-flow mode stress profile 33.
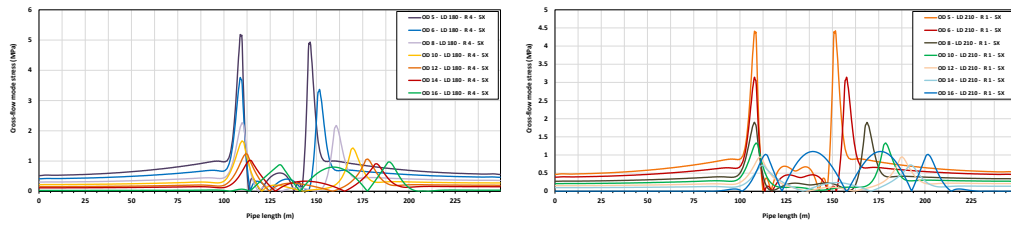
Figure A- 39: Multi-span cross-flow mode stress profile 34.
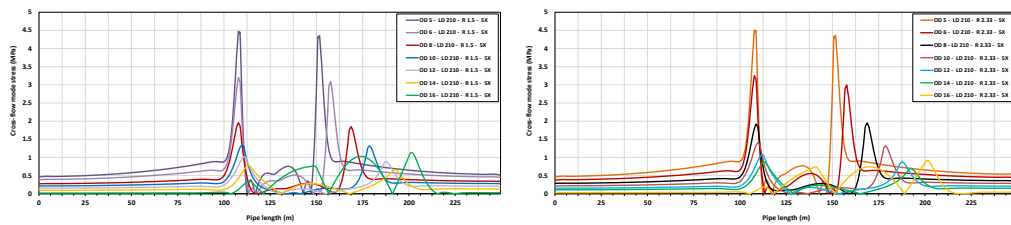

Figure A- 40: Multi-span cross-flow mode stress profile 35.
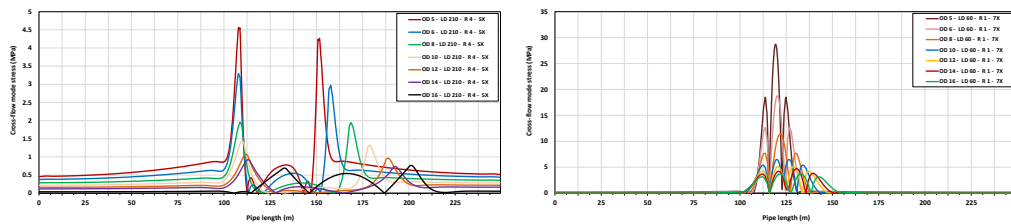
Figure A- 41: Multi-span cross-flow mode stress profile 36.
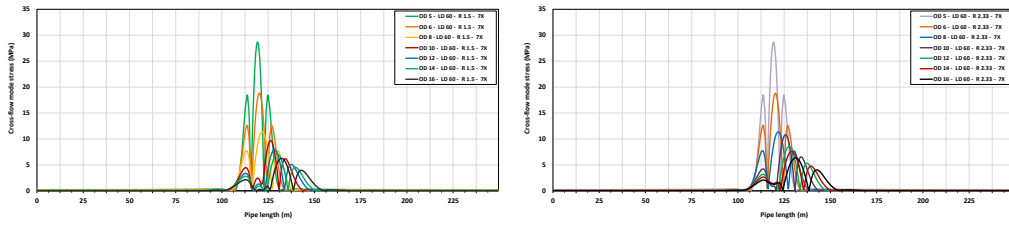
Figure A- 42: Multi-span cross-flow mode stress profile 37.
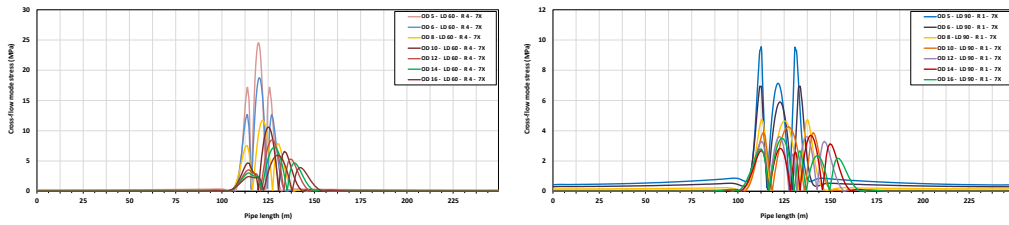
Figure A- 43: Multi-span cross-flow mode stress profile 38.
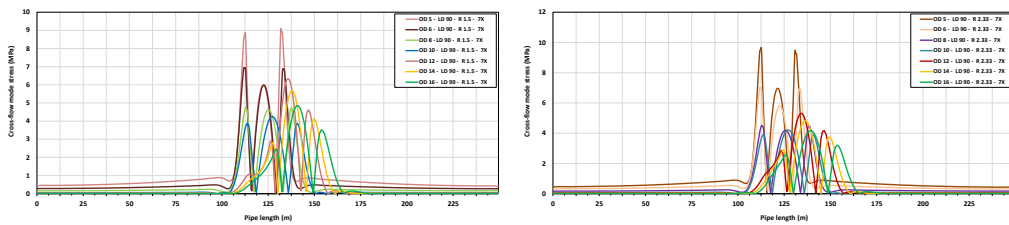
Figure A- 44: Multi-span cross-flow mode stress profile 39.
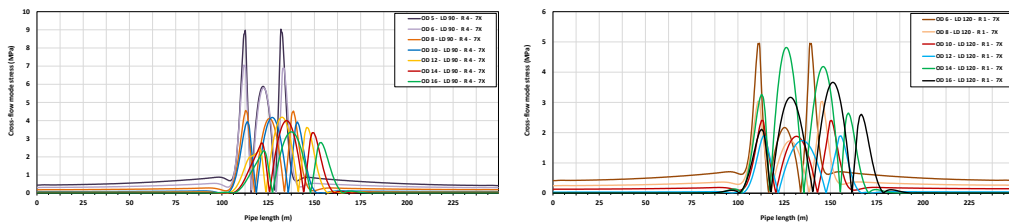
Figure A- 45: Multi-span cross-flow mode stress profile 40.
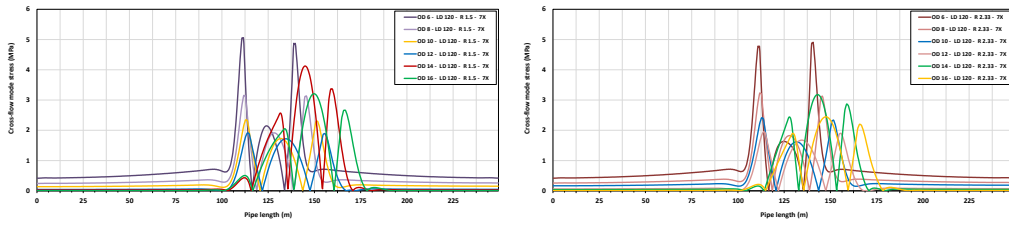
Figure A- 46: Multi-span cross-flow mode stress profile 41.
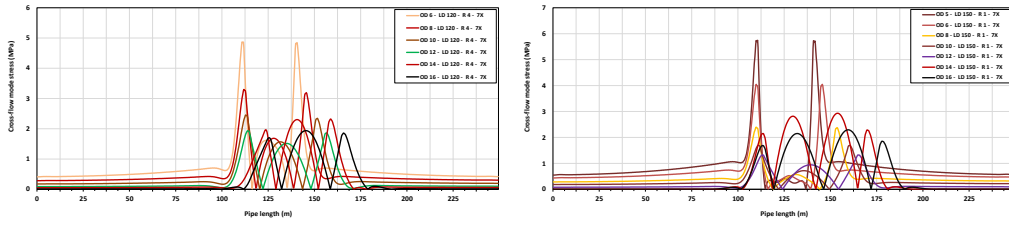
Figure A- 47: Multi-span cross-flow mode stress profile 42.
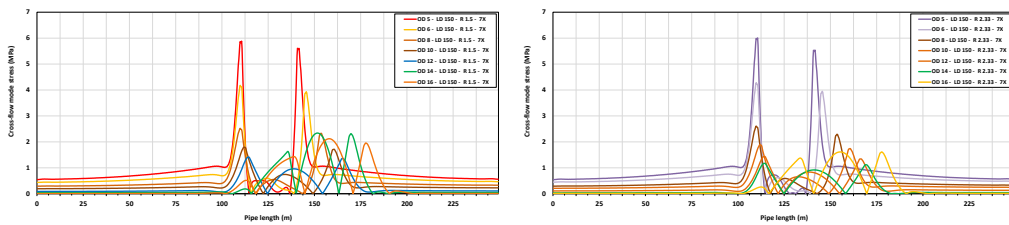
Figure A- 48: Multi-span cross-flow mode stress profile 43.
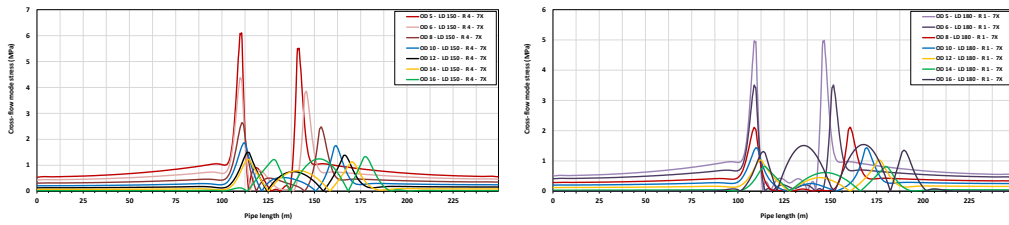
Figure A- 49: Multi-span cross-flow mode stress profile 44.
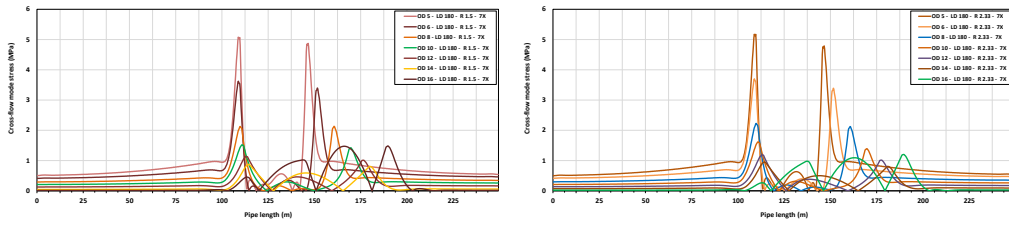
Figure A- 50: Multi-span cross-flow mode stress profile 45.
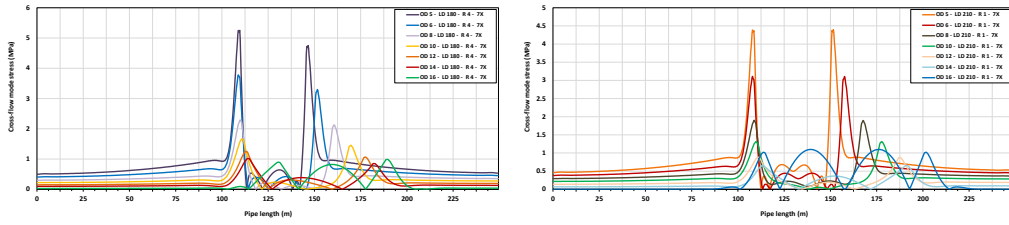
Figure A- 51: Multi-span cross-flow mode stress profile 46.
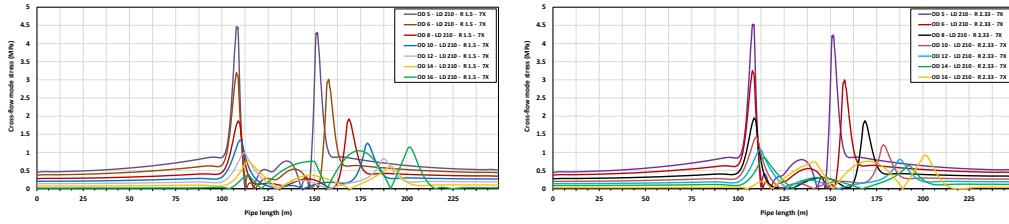
Figure A- 52: Multi-span cross-flow mode stress profile 47.
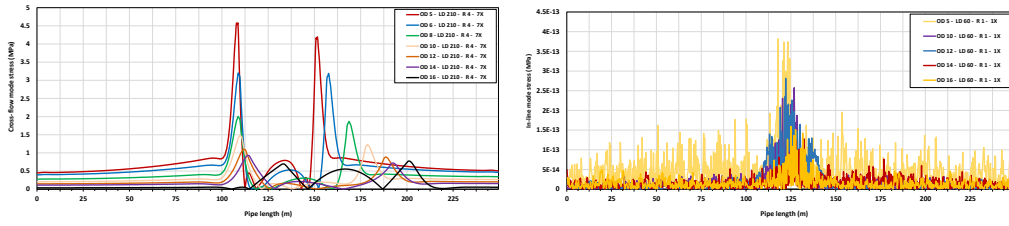
Figure A- 53: Multi-span cross-flow mode stress profile 48.

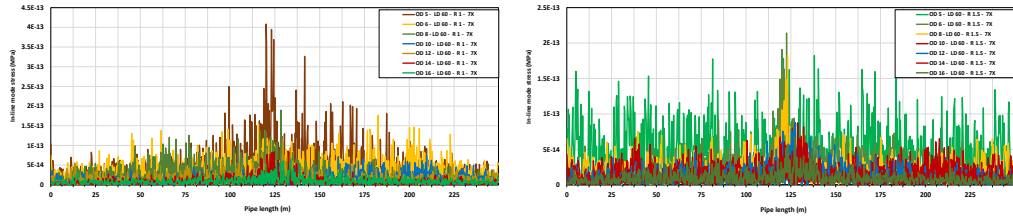# In-line mode stress profiles for multi-span configuration.
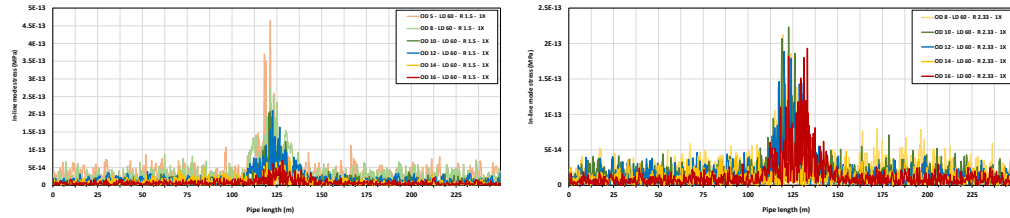
Figure A- 54: Multi-span in-line mode stress profile 1.
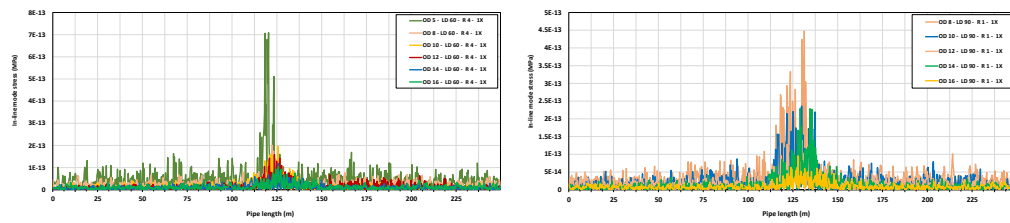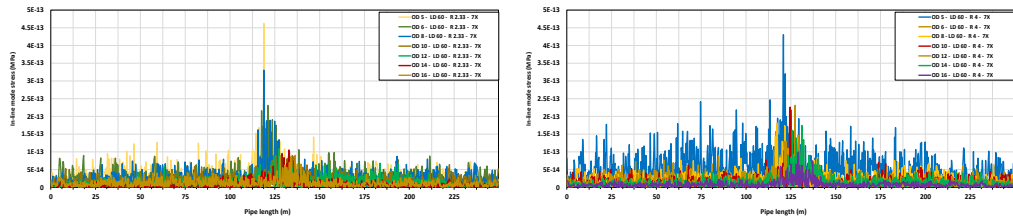

Figure A- 55: Multi-span in-line mode stress profile 2.
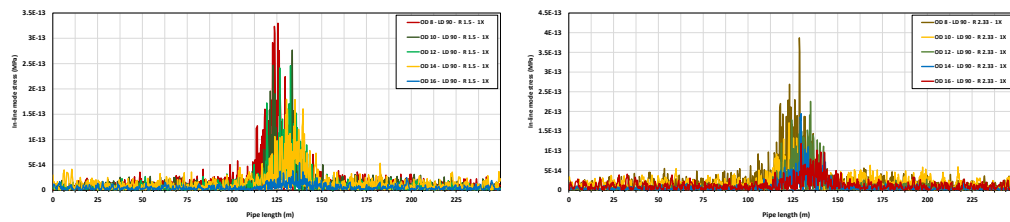
Figure A- 56: Multi-span in-line mode stress profile 3.
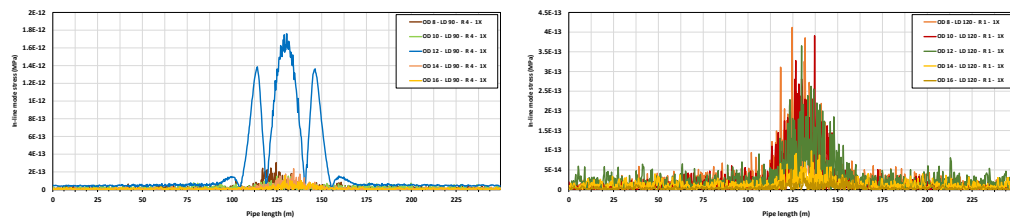
Figure A- 57: Multi-span in-line mode stress profile 4.
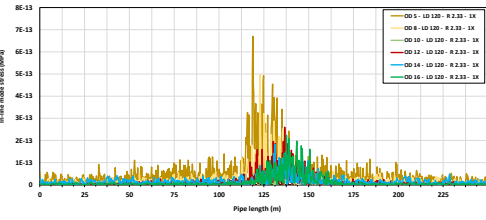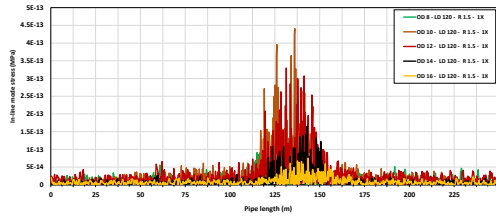
Figure A- 58: Multi-span in-line mode stress profile 5.
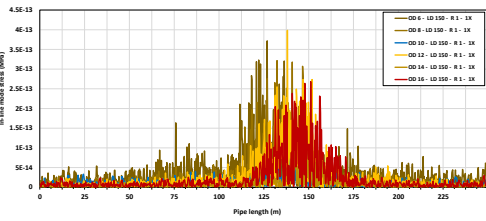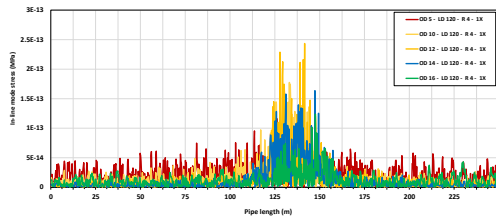
Figure A- 59: Multi-span in-line mode stress profile 6.
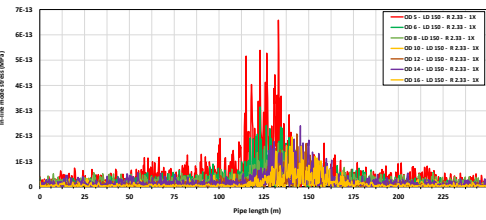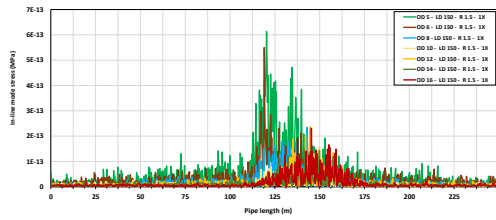
Figure A- 60: Multi-span in-line mode stress profile 7.
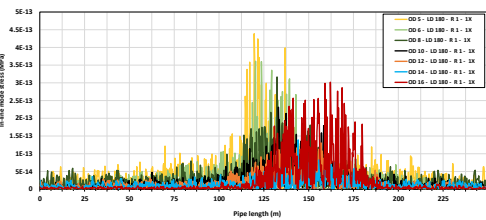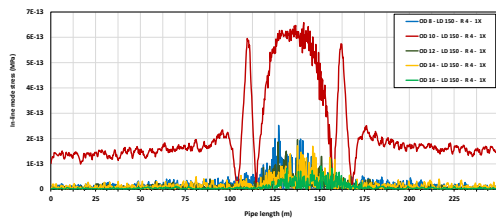
Figure A- 61: Multi-span in-line mode stress profile 8.
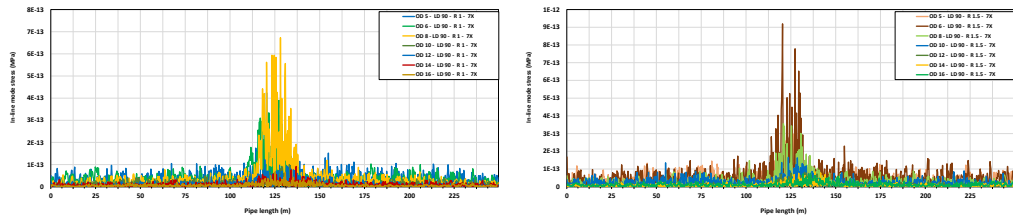
177
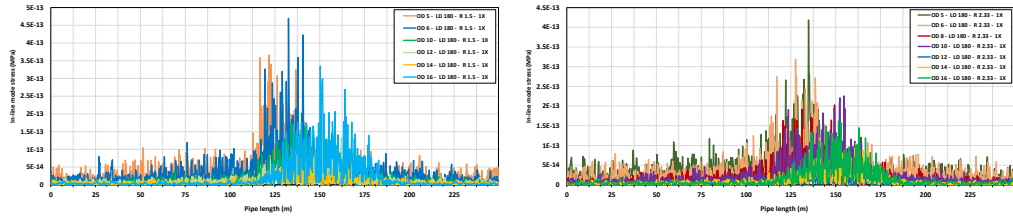
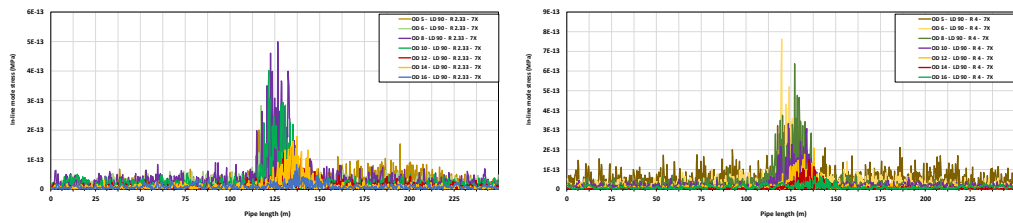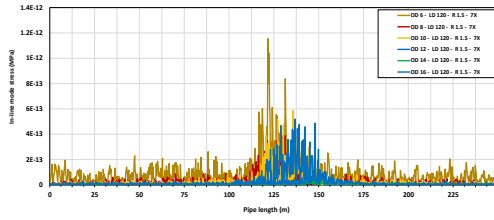Figure A- 62: Multi-span in-line mode stress profile 9.
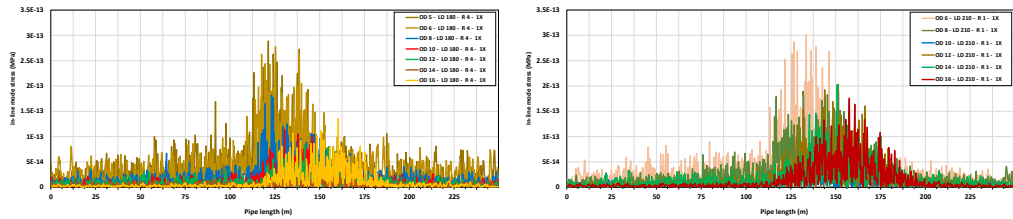
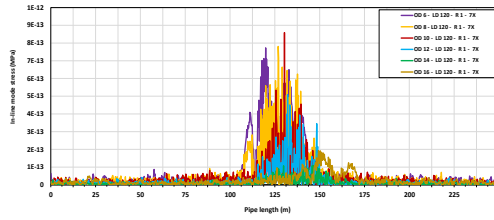Figure A- 63: Multi-span in-line mode stress profile 10.
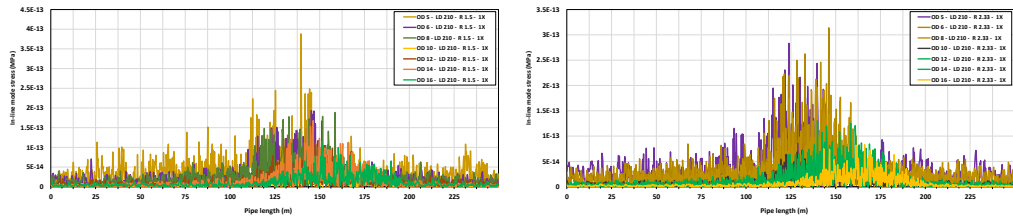
Figure A- 64: Multi-span in-line mode stress profile 11.
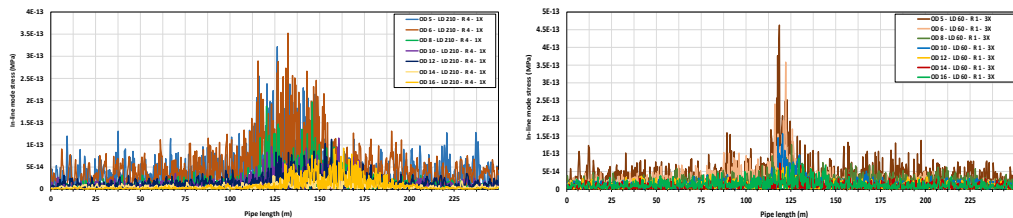
Figure A- 65: Multi-span in-line mode stress profile 12.

178
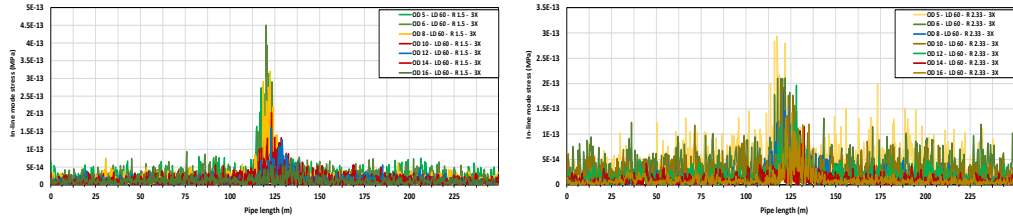
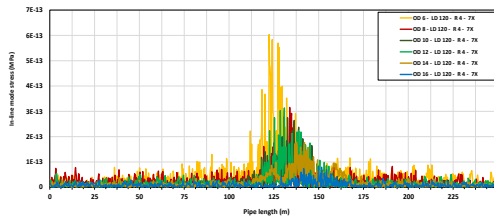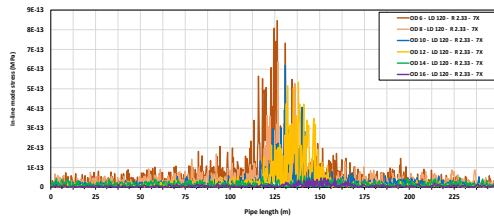Figure A- 66: Multi-span in-line mode stress profile 13.
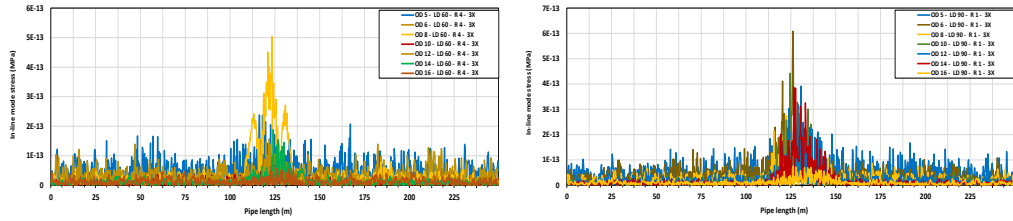
Figure A- 67: Multi-span in-line mode stress profile 14.
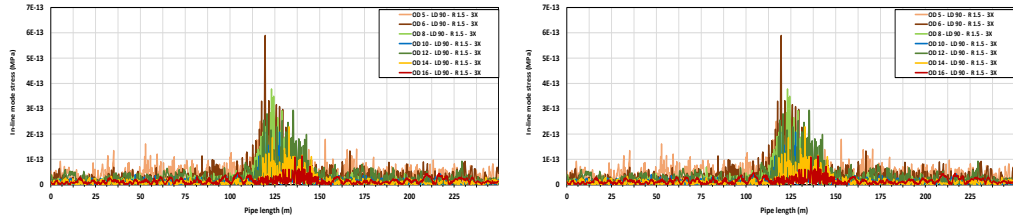
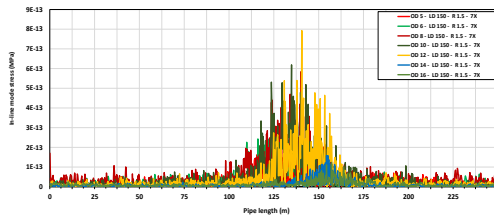Figure A- 68: Multi-span in-line mode stress profile 15.
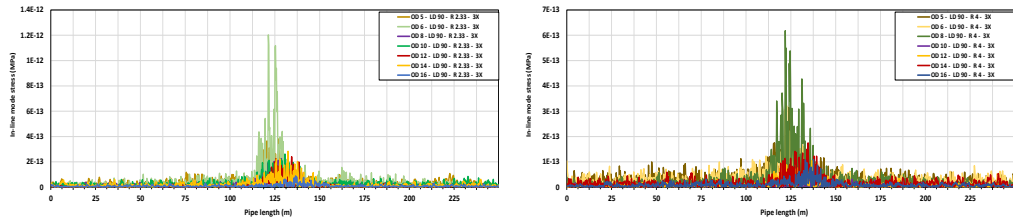
Figure A- 69: Multi-span in-line mode stress profile 16.
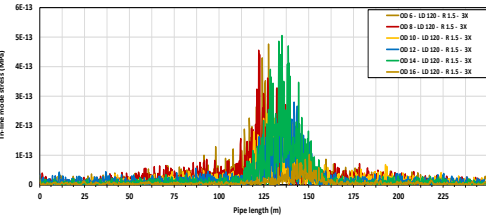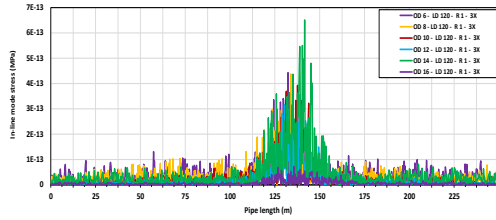
Figure A- 70: Multi-span in-line mode stress profile 17.
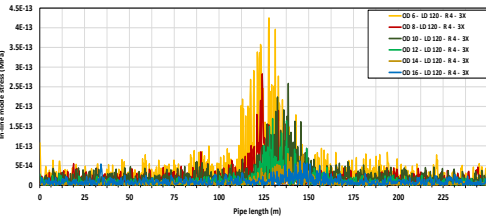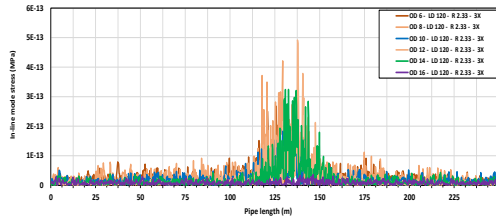
Figure A- 71: Multi-span in-line mode stress profile 18.
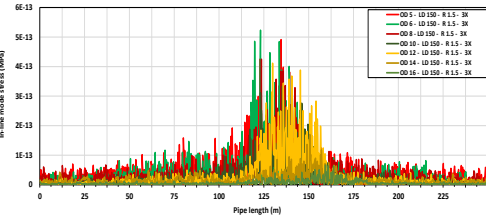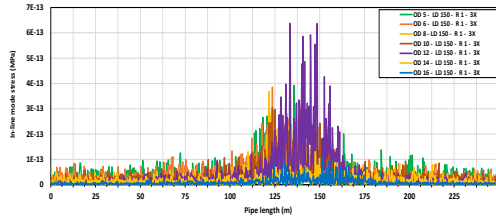
Figure A- 72: Multi-span in-line mode stress profile 19.
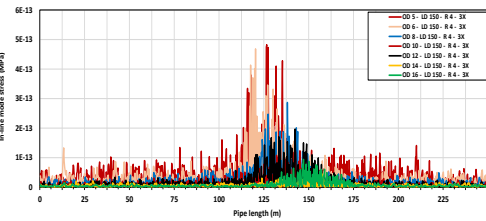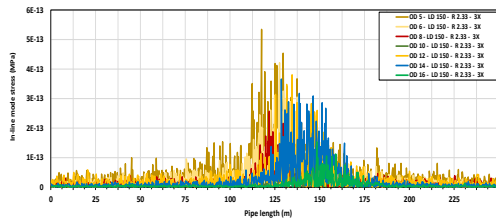
Figure A- 73: Multi-span in-line mode stress profile 20.
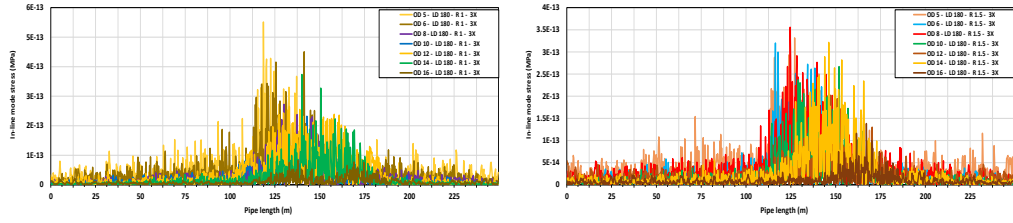
Figure A- 74: Multi-span in-line mode stress profile 21.
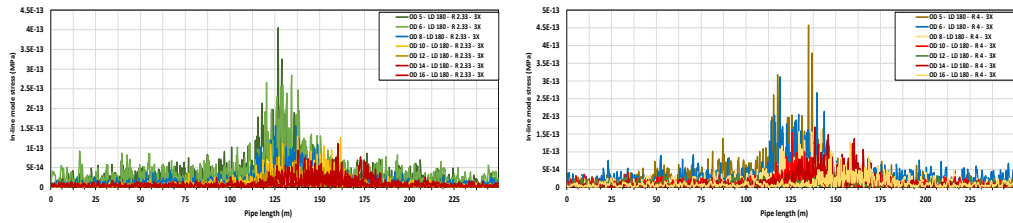
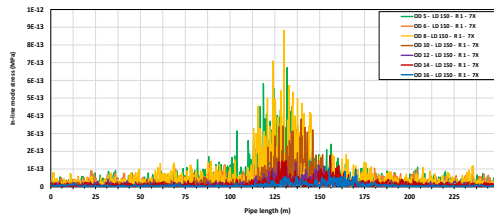Figure A- 75: Multi-span in-line mode stress profile 22.
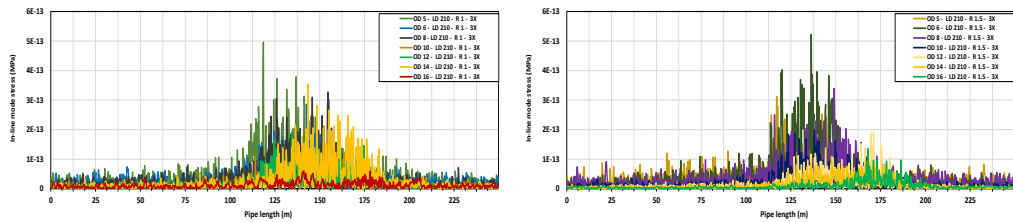
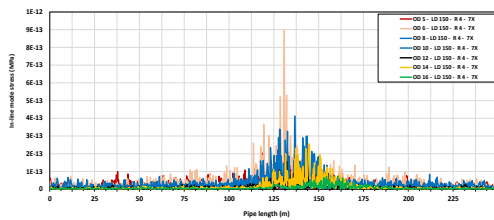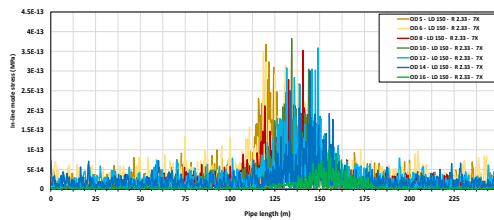Figure A- 76: Multi-span in-line mode stress profile 23.
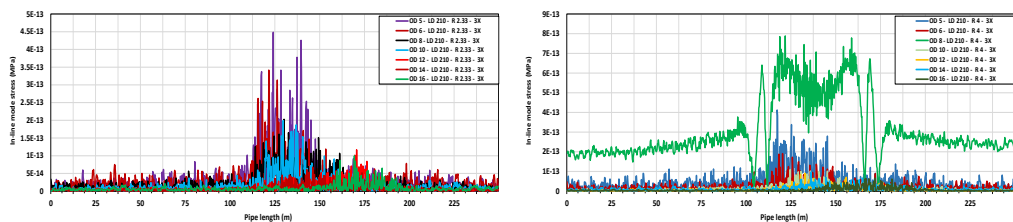
Figure A- 77: Multi-span in-line mode stress profile 24.
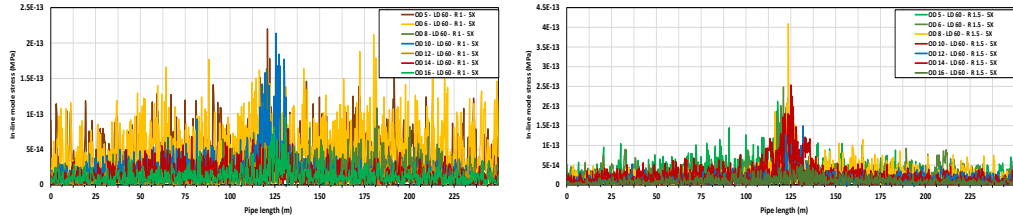
Figure A- 78: Multi-span in-line mode stress profile 25.
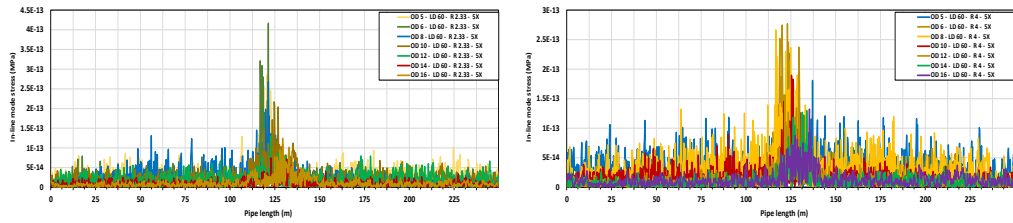
Figure A- 79: Multi-span in-line mode stress profile 26.
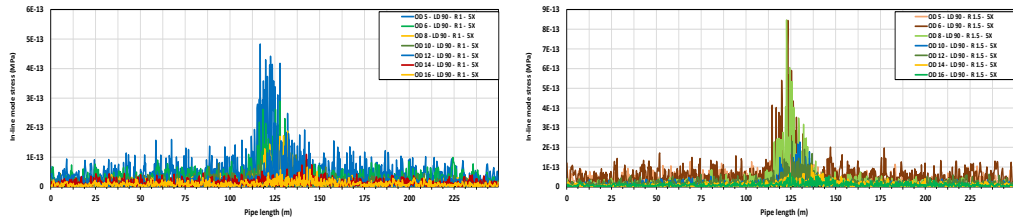
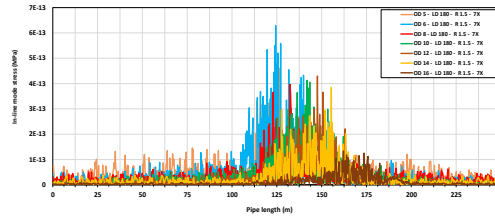Figure A- 80: Multi-span in-line mode stress profile 27.
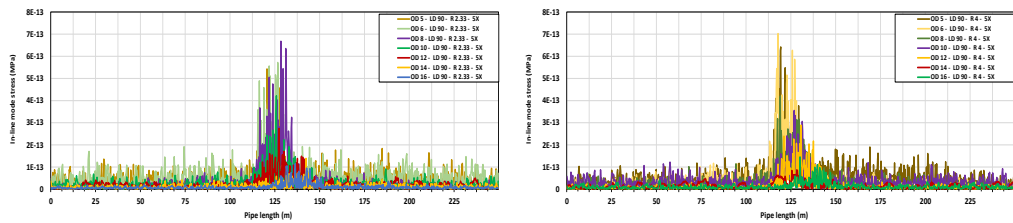
Figure A- 81: Multi-span in-line mode stress profile 28.
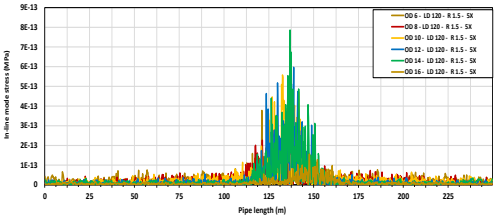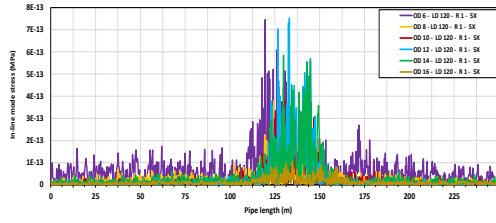
Figure A- 82: Multi-span in-line mode stress profile 29.
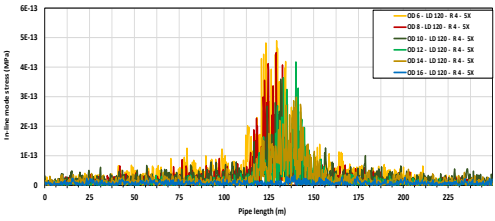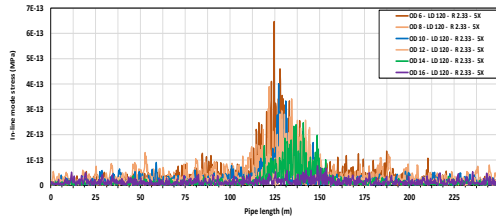
Figure A- 83: Multi-span in-line mode stress profile 30.
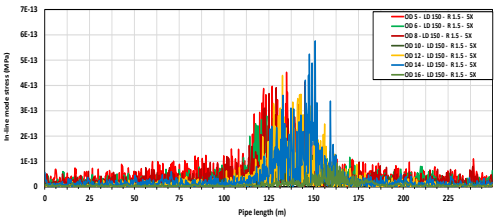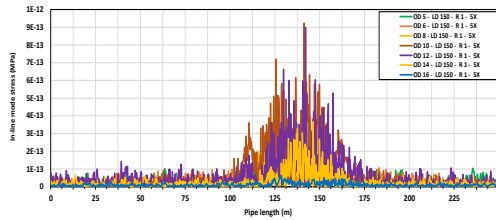
Figure A- 84: Multi-span in-line mode stress profile 31.
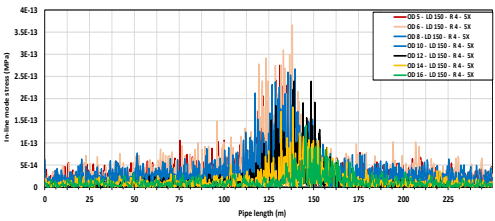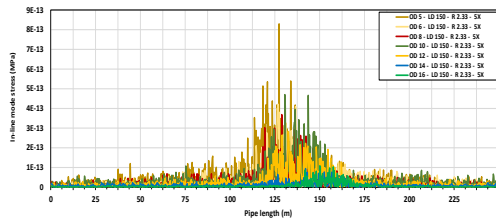
Figure A- 85: Multi-span in-line mode stress profile 32.
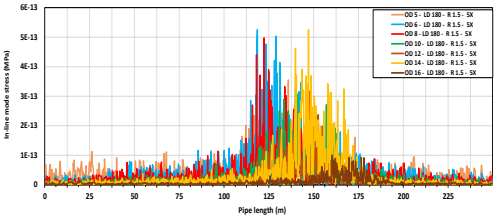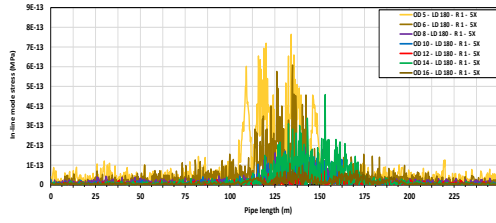
Figure A- 86: Multi-span in-line mode stress profile 33.
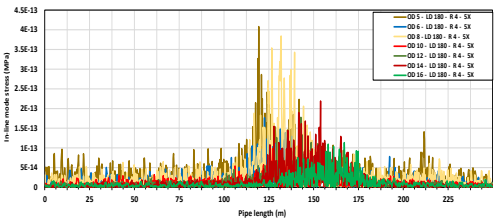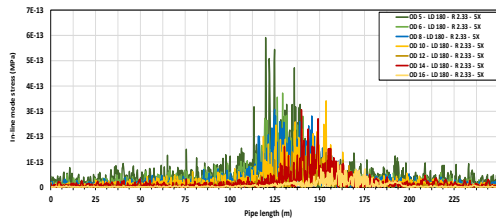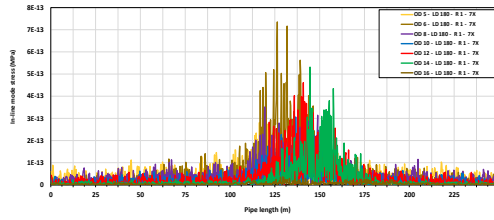

Figure A- 87: Multi-span in-line mode stress profile 34.
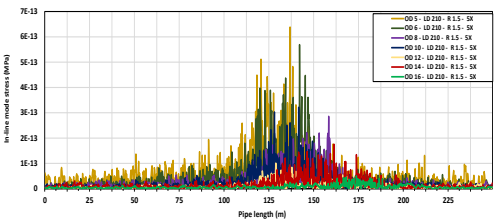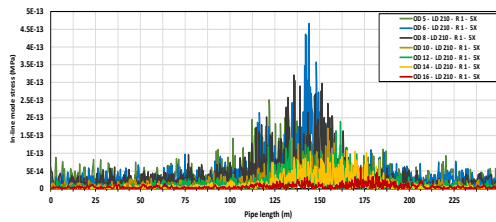
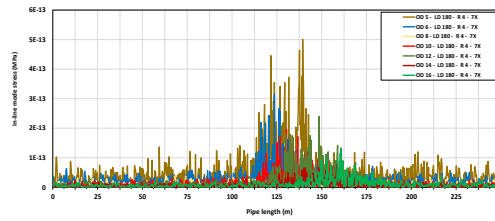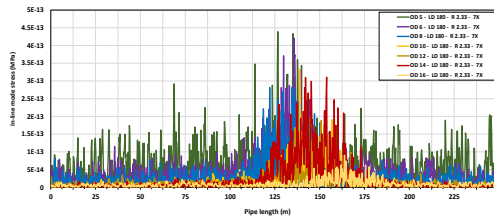Figure A- 88: Multi-span in-line mode stress profile 35.
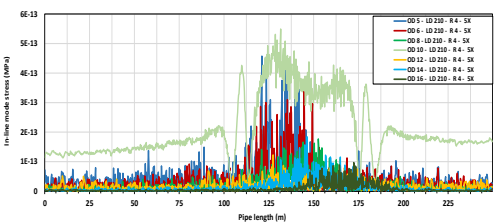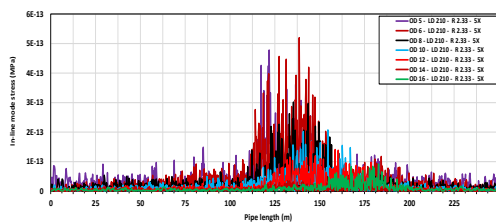
Figure A- 89: Multi-span in-line mode stress profile 36.

Figure A- 90: Multi-span in-line mode stress profile 37.

Figure A- 91: Multi-span in-line mode stress profile 38.

Figure A- 92: Multi-span in-line mode stress profile 39.

Figure A- 93: Multi-span in-line mode stress profile 40.

185

Figure A- 94: Multi-span in-line mode stress profile 41.

Figure A- 95: Multi-span in-line mode stress profile 42.

Figure A- 96: Multi-span in-line mode stress profile 43.

Figure A- 97: Multi-span in-line mode stress profile 44.

Figure A- 98: Multi-span in-line mode stress profile 45.

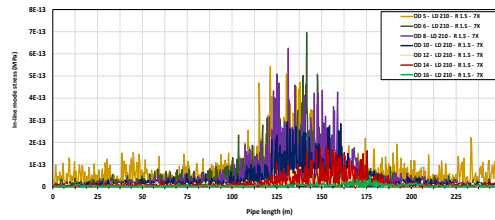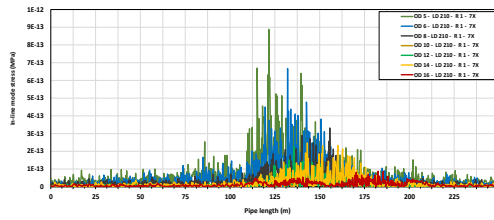Figure A- 99: Multi-span in-line mode stress profile 46.
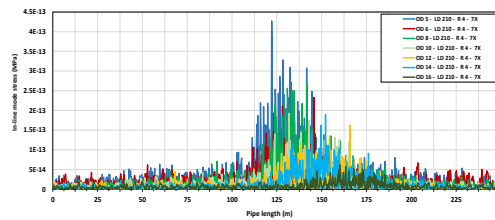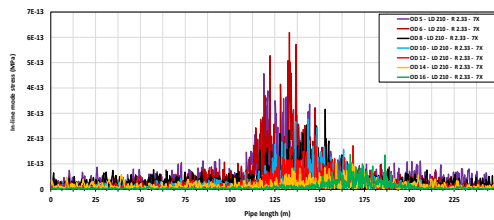

Figure A- 100: Multi-span in-line mode stress profile 47.

Figure A- 101: Multi-span in-line mode stress profile 48.